TESIS DE LA UNIVERSIDAD
DE ZARAGOZA

2022

121

Teodora Randelovic

The Role of Microenviroment in Glioblastoma Progression and Resistance Development

Director/es
Ochoa Garrido, Ignacio

EXTRACTO

ISSN 2254-7606

Prensas de la Universidad
Universidad Zaragoza

Servicio de Publicaciones

ISSN 2254-7606

Tesis Doctoral [Extracto]

THE ROLE OF MICROENVIROMENT IN GLIOBLASTOMA PROGRESSION AND RESISTANCE DEVELOPMENT

Autor

Teodora Randelovic

Director/es

Ochoa Garrido, Ignacio

UNIVERSIDAD DE ZARAGOZA
Escuela de Doctorado

Programa de Doctorado en Ingeniería Biomédica

2022

The Role of Microenvironment in Glioblastoma Progression and Chemoresistance Development

PhD Dissertation presented by
Teodora Ranđelović

Faculty supervisor
Ignacio Ochoa Garrido

PhD Programme: **Biomedical Engineering**

Tissue Microenvironment Lab
Instituto de Investigación en Ingeniería de Aragón (I3A)
Instituto de Investigación Sanitaria Aragón
University of Zaragoza

2022

Acknowledgments

After five years full of learning, enjoying and suffering, this stage of my life is finally coming to an end. But, it wouldn’t be possible without people around me. I hope you are all aware that I am much more grateful than written below, since words are not my forte.

I want to thank Ignacio Ochoa, Luis Fernandez, and Rosa Monge for the given opportunity and Instituto de Salud Carlos III for the i-PFIS grant that made this thesis possible. Being part of the TME lab and working with Beonchip have taught me how to work in the interdisciplinary team and appreciate its huge value, despite the difficulties still on the way.

Iñaki, thank you for believing in me and giving me the opportunity to learn and progress. Thank you for your enthusiasm and infinite ideas, even though they often gave me more (almost impossible ☺) work. Thank you for counting on me for the new projects; they were challenging but exciting.

I would like to express my gratitude to Roxana for everything done during these years, especially for helping me with the grant application and starting my life here in Zaragoza.

I would like to thank Milica, Tijana and Jelena from the Department of Neurobiology (IBISS, Serbia) for everything they taught me and their support over the years.

This thesis wouldn’t be possible without collaborations, so a huge thank you to all of you!

Team Beonchip – Rosa, Lara, Sara, Luis – thank you for the close collaboration and showing me the part of industry life. Lara, thank you for having me in the lab and teaching me the fabrication processes. Claudia, thank you for sharing the experience of new device fabrication with me. Sandra, for all the troubles we passed through together and all the achievements that brightened up the day.

I particularly acknowledge the patients for their participation in the investigation and the Biobank of the Aragon Health System and the Department of Neurosurgery of the University Hospital Lozano Blesa for the collaboration.

I owe a great debt of gratitude to the Pathology service of the University Hospital Miguel Servet. Isabel, thank you for the hours spent explaining the samples; I learned a lot. Violeta, thank you for following us in our ideas and doing everything we asked for. Without you, important parts of this thesis wouldn’t be possible.

Genomics Unit from CNIC, thank you for your help with sequencing and analysis. Quique, without you, the last part of my thesis wouldn’t exist, so infinite thanks!

I would like to thank the Department of Human Anatomy and Histology for giving me the opportunity to collaborate in teaching.

I am grateful to all the members (former and present) of TME lab, for all the projects we shared, for your constant support and friendship, and for all the trust you gave me.

Manolo, Sara O, Clara A, Jesus, Rebeca SP, Carmen, Ana Rosa, thank you for your support and help. Maria, Guillermo, Chema, thank you for all the help and advices.

Sandra, Alodia, and Jacobo, you have been there for me since we started this journey. We shared good and bad, and I am grateful I had you as my companions in both professional and personal areas. David, Hector, and Marina, for all the moments we lived together. Clara B, Sara A, Claudia, Vira, Laura, Lorena, and our visiting members, Isabel, José and Jorik, thank you for all the time in and out of the lab. It was a pleasure to share with you all successes and failures.

I would also like to thank Cris and Yago from the next-door group, for making long culture-room hours pass quickly.

Thank you for being with me to my friends back in Serbia (and Germany), and all the people who became my family here in Zaragoza.

Víctor, thank you for the support and understanding; I know it wasn’t always easy.

In the end, the biggest thanks to my family for the unlimited support. Without you, I wouldn’t be here.

Najveću zahvalnost dugujem svojoj porodici na neizmernoj podršci koju mi pružaju svih ovih godina. Bez vas ne bih bila gde sam.

Thank you!
¡Gracias!
HVALA!

Index

Abstract

1.1 Abstract

Glioblastoma (GBM) is a highly heterogeneous primary brain tumor, with a very low survival rate. It has been shown recently that the complex tumor microenvironment has an essential role in tumor progression and therapy response. Hence, it is crucial to identify all the components and their interactions, and incorporate them in in vitro models used for GBM studies and therapy development.

The development of new technologies in the last decades ensured progress in both mentioned fields. Different multiomics techniques allow detailed characterization of the patient samples. On the other hand, the evolution of cell culture techniques and fabrication processes enables the creation of more physiological in vitro systems than traditional Petri dish culture (organ on chip).

The main aim of this thesis was to study the role of the microenvironment in the response of GBM to temozolomide (TMZ) treatment. Microfluidic devices, previously developed within the group, were modified to study the impact of oxygen concentration on GBM progression. Hypoxia was shown to be essential for the necrotic core formation and it protected cells from the TMZ effect. Moreover, the microfluidic device design was improved to enable the creation of a more advanced and controllable system.

Furthermore, spheroid culture gave us a valuable model for chemoresistance development studies. After the application of two clinical TMZ treatment cycles, the presence of a population of resistant spheroids was observed. Morphologically, those spheroids were a combination of control and treated spheroids, and they had a specific gene expression pattern.

Last but not least, a new spatial transcriptomics technique was used to characterize better GBM patient samples correlating their gene expression with the histological location. It enabled the identification of differential transcriptomic clusters within apparently homogeneous tissues, confirming the high heterogeneity of this tumor, not only in a morphological aspect but also molecularly.

1.2 Resumen

El glioblastoma (GBM) es un tumor cerebral primario altamente heterogéneo, con una tasa de supervivencia muy baja. Recientemente se ha demostrado que su microentorno tumoral complejo tiene un papel esencial en la progresión del tumor y la respuesta a la terapia. Por lo tanto, es crucial identificar todos los componentes y sus interacciones, e incorporarlos en modelos in vitro utilizados para estudios sobre GBM y el desarrollo de nuevas terapias.

El desarrollo de nuevas tecnologías en las últimas décadas ha asegurado el progreso en ambos campos mencionados. Diferentes técnicas multiómicas permiten una caracterización detallada de las muestras de los pacientes. Por otro lado, la evolución de las técnicas de cultivo celular y los procesos de fabricación permiten la creación de sistemas in vitro más fisiológicos que el cultivo tradicional en placas de Petri (organ on chip).

El principal objetivo de esta tesis fue estudiar el papel del microentorno en la respuesta del GBM al tratamiento con temozolomida (TMZ). Se modificaron dispositivos microfluídicos, desarrollados previamente dentro del grupo, para estudiar el impacto de la concentración de oxígeno en la progresión de GBM. Se demostró que la hipoxia es esencial para la formación del núcleo necrótico y protege a las células del efecto de TMZ. Además, se mejoró el diseño del dispositivo microfluídico para permitir la creación de un sistema más avanzado y controlable.

Igualmente, el cultivo de esferoides nos proporcionó un modelo valioso para los estudios de desarrollo de quimio-resistencia. Tras la aplicación de dos ciclos de tratamiento clínico con TMZ, se observó la aparición de una población de esferoides resistentes. Morfológicamente, esos esferoides eran una combinación de esferoides control y esferoides tratados, que tenían un patrón de expresión génica específico.

Por último, se utilizó una nueva técnica de transcriptómica espacial para caracterizar mejor las muestras de pacientes con GBM, correlacionando su expresión génica con la ubicación histológica. Esto permitió la identificación de clusters transcriptómicos diferenciales dentro de tejidos aparentemente homogéneos, confirmando la alta heterogeneidad de este tumor, no solo en el aspecto morfológico sino también molecular.

List of abbreviations

2D	Two-dimensional
3D	Three-dimensional
ABC	ATP-binding cassette
ABCB1	ATP-Binding Cassette Subfamily B Member 1
ABCC1	ATP-Binding Cassette Subfamily C Member 1
ABCC2	ATP-Binding Cassette Subfamily C Member 2
ABCC3	ATP-Binding Cassette Subfamily C Member 3
ABCC4	ATP-Binding Cassette Subfamily C Member 4
ABCC5	ATP-Binding Cassette Subfamily C Member 5
ABCG2	ATP-Binding Cassette Subfamily G Member 2
ACTB	Actin Beta
AHR	Aryl Hydrocarbon Receptor
AR	Androgen Receptor
ARNT	Aryl Hydrocarbon Receptor Nuclear Translocator
ASCL1	Achaete-Scute Family BHLH Transcription Factor 1
ATCC	American Type Culture Collection
ATG5	Autophagy Related 5
ATM	Ataxia Telangiectasia Mutated
ATP	Adenosine Triphosphate
AV	Annexin V
B2M	Beta-2-Microglobulin
BBB	Blood-Brain Barrier
BCL2	B-cell lymphoma 2
BCNU	1,3-bis (2-chloroethyl)-1-nitrosourea
BCRP	Breast Cancer Resistance Protein
bFGF	Basal Fibroblast Growth Factor
BG	Be-Gradient
BMI	B cell-specific Moloney murine leukemia virus integration site 1
BNIP3	BCL2 Interacting Protein 3
BRCA2	Breast Cancer Type 2 susceptibility protein
BSA	Bovine Serum Albumin
CAM	Calcein Acetoxymethyl Ester
CCK8	Cell counting kit-8
CCL2	C-C Motif Chemokine Ligand 2

CCNA1	Cyclin A1
CCNB1	Cyclin B1
CCND1	Cyclin D1
CCNE1	Cyclin E1
CCNU	Comustine
CCR2	C-C Motif Chemokine Receptor 2
CD	Cluster of Differentiation
CDKN1A	Cyclin Dependent Kinase Inhibitor 1A
CDRA	Cancer Drug Resistance Accelerator
CHD1	Chromodomain Helicase DNA Binding Protein 1
CHI3L1	Chitinase 3 Like 1
CHI3L2	Chitinase 3 Like 2
Chk	Checkpoint Kinase
CLM	Clomipramine
COC	Cyclic Olefin Copolymer
COP	Cyclic Olefin Polymer
CSC	Cancer Stem Cells
CSPG4	Chondroitin Sulfate Proteoglycan 4
CXCL12	C-X-C Motif Chemokine Ligand 12
CXCR4	C-X-C Motif Chemokine Receptor 4
CYP1A1	Cytochrome P450 Family 1 Subfamily A Member 1
CYP2B6	Cytochrome P450 Family 2 Subfamily B Member 6
CYP2C19	Cytochrome P450 Family 2 Subfamily C Member 19
CYP3A4	Cytochrome P450 Family 3 Subfamily A Member 4
CYP450	Cytochrome P450
DCK	Deoxycytidine Kinase
DDP	Cisplatin
DHC2	Dynein, cytoplasmic 2, heavy chain 1
DLL3	Delta Like Canonical Notch Ligand 3
DMEM	Dulbecco’s modified Eagle’s medium
DMSO	Dimethyl sulfoxide
DOX	Doxorubicin
ECFC	Endothelial Colony Forming Cells
ECM	Extracellular Matrix

EDC	N-Ethyl-N’-(3-dimethylaminopropyl) carbodiimide hydrochloride
EDTA	Ethylenediaminetetraacetic acid
EGF	Epidermal Growth Factor
EGFR	Epidermal Growth Factor Receptor
EMT	Epithelial–Mesenchymal Transition
ERBB2	Erb-B2 Receptor Tyrosine Kinase 2
ERBB4	Erb-B2 Receptor Tyrosine Kinase 4
ERK	Extracellular signal-regulated kinase
ESPS	electrospun polystyrene
ESR2	Estrogen Receptor 2
FBS	Fetal Bovine Serum
FDA	Food and Drug Administration
FF	Fresh Frozen
FFPE	Formalin-Fixed Paraffin-Embedded
FLNA	Filamin A
GA	Glutaraldehyde
GABRA1	Gamma-aminobutyric acid receptor subunit alpha-1
GAPDH	Glyceraldehyde-3-Phosphate Dehydrogenase
GAS1	Growth Arrest Specific 1
GBM	Glioblastoma
GCNT	Graphene–carbon nanotube
GFAP	Glial Fibrillary Acidic Protein
GFP	Green Fluorescent Protein
GMHA	Glycidyl Methacrylate-Hyaluronic Acid
GPX	Glutathione Peroxidase
GR	Glutathione Reductase
GSC	Glioblastoma-derived cancer stem cells
H&E	Hematoxylin-eosin
HA	Hyaluronic Acid
HAMA	Methacrylated Hyaluronic Acid
HES	Hairy and Enhancer of Split-1
HIF	Hypoxia Inducible Factor
HLA	Human leukocyte antigen

HPRT1	Hypoxanthine Phosphoribosyltransferase 1
HRE	Hypoxia-Response Element
HUVEC	Human Umbilical Vein Endothelial Cells
ID1	Inhibitor Of DNA Binding 1
IDH	isocitrate dehydrogenase
IF	Interstitial Flow
IGF1R	Insulin Like Growth Factor 1 Receptor
JAG1	Jagged Canonical Notch Ligand 1
KDR	Kinase Insert Domain Receptor
LC3	Microtubule-associated protein 1A/1B-light chain 3
LIN28	Lin-28 Homolog
MALDI	Matrix-Assisted Laser Desorption/Ionization
MAPK	Mitogen-Activated Protein Kinases
MCTS	Multicellular Tumor Spheroids
MDR	Multidrug resistance
MEK	Mitogen-activated protein kinase kinase
MERTK	MER Proto-Oncogene, Tyrosine Kinase
MES	2-(N-Morpholino)ethanesulfonic acid hydrate
MET	MET Proto-Oncogene, Receptor Tyrosine Kinase
MGMT	O-6-Methylguanine-DNA Methyltransferase
MKI67	Marker Of Proliferation Ki-67
MMP	Matrix metalloproteinase
MRP	Multidrug resistance-associated protein
MSC	Mesenchymal stem cells
MT2A	Metallothionein 2A
MVP	Major Vault Protein
NAT2	N-Acetyltransferase 2
ND	Not determined
NEFL	Neurofilament Light Chain)
NES	Nestin

NFKB	Nuclear Factor Kappa B Subunit 1
NHLF	Normal human lung fibroblasts
NHS	N-Hydroxysulfosuccinimide sodium salt solutions
NKX2-2	NK2 Homeobox 2
OCT	Optimal cutting temperature compound
OLIG2	Oligodendrocyte Transcription Factor 2
OXPHOS	Oxydative phosphorylation
PAA	Poly(acrylic acid)
PARP	Poly (ADP-ribose) Polymerases
PBS	Phosphate-Buffered Saline
PCA	Principal Component Analysis
PCL	Polycaprolacton
PDGFRA	Platelet Derived Growth Factor Receptor Alpha
PDMS	Polydimethylsiloxane
PECAM1	Platelet And Endothelial Cell Adhesion Molecule 1
PEG	Poly(ethylene-glycol)
PEGDA	Polyethylene glycol diacrylate
PEI	poly(ethyleneimine)
PFA	Paraformaldehyde
PI	Propidium Iodide
PIK3R1	Phosphoinositide-3-Kinase Regulatory Subunit 1
PMMA	Poly(methyl methacrylate)
POU3F2	POU Class 3 Homeobox 2
PPAR	Perosyxomel proliferator activated receptors
PS	Polystyrene
RALBP1	RalA Binding Protein 1
RARG	Retinoic Acid Receptor Gamma
RGD	Arginine-glycine-aspartate
RIN	RNA Integrity Number
ROS	Reactive Oxygene Species
RXRB	Retinoid X Receptor Beta
SALL2	Spalt Like Transcription Factor 2

SH	4-54-STAT3 inhibitor
SHH	Sonic Hedgehog Signaling Molecule
SLC12A5	Solute Carrier Family 12 member 5
SMO	Smoothened, Frizzled Class Receptor
SOD	superoxide dismutase
SOX2	SRY-Box Transcription Factor 2
SULT1E1	Sulfotransferase Family 1E Member 1
SYT1	Synaptotagmin 1
TCA	Tricarboxylic acid
TCF4	Transcription Factor 4
TGFB1	Transforming Growth Factor Beta 1
TIC	Tumor Initiating cells
TME	Tumor Microenvironment
TMZ	Temozolomide
TNFRSF1A	TNF Receptor Superfamily Member 1A
TNFα	Tumor Necrosis Factor Alpha
TOP2	DNA Topoisomerase II
TRADD	TNFRSF1A Associated Via Death Domain
t-SNE	t-distributed stochastic neighbour embedding
TUBB3	Tubulin β3
UMAP	Uniform Manifold Approximation and Projection
UMI	Unique Molecular Identifier
VCR	Vincristine
VEGF	Vascular Endothelial Growth Factor
VEGFR2	Vascular endothelial growth factor receptor 2
VPS34	Phosphatidylinositol 3-kinase
WHO	World Health Organization
XPC	Xeroderma Pigmentosum C

List of figures

List of tables

1 Introduction[1]

---

[1] This chapter was adapted from: Stanković T*, Ranđelović T*, Dragoj M, Stojković Burić S, Fernández L, Ochoa I, Pérez-García VM, Pešić M. In vitro biomimetic models for glioblastoma – a promising tool for drug response studies. Drug Resist. Updat. 2021 Mar; 55:100753. doi: 10.1016/j.drup.2021.100753. Epub 2021 Feb 20. PMID: 33667959. *authors contributed equally

Glioma is the most common and aggressive type of malignant brain tumors. High-grade gliomas, including WHO grade III (anaplastic astrocytoma and oligodendroglioma) and WHO grade IV (glioblastoma) gliomas, are hardest to treat and have the worst survival prognosis of all brain tumors[1–4]. Among high-grade gliomas, glioblastoma (GBM) is the most frequently diagnosed type that commonly occurs between the fifth and the seventh decade of life[2,3,5]. GBM is also the most aggressive brain tumor type with only a 5-year survival rate of 6.8% which renders it one of the cancers with the worst prognosis[3]. The aggressiveness of this tumor is even more distressing given that it does not metastasize to other organs, like other solid tumors, but remains a rather brain-localized primary tumor which kills the patient.

The standard clinical protocol for GBM treatment includes surgical resection and radiation with concomitant and adjuvant chemotherapy (Stupp protocol). The only approved chemotherapeutic drug currently used in Stupp protocol is temozolomide (TMZ) that improves patient survival by only 2.5 months compared to radiotherapy alone[6]. Multiple new targeted therapies have been tested but also failed to prolong patients' survival[5,7]. The latest FDA approved electrical device that generates tumor treating fields (Optune/NOVOTTF-100A System) improved patients' quality of life, but could not extend their survival beyond 3 months[8].

The evident stagnation in GBM treatment and the implementation of new therapeutic strategies is due to a number of factors including: (i) specific, hardly reachable, tumor location in the brain, (ii) highly invasive potential, (iii) presence of the blood-brain barrier (BBB), and (iv) considerable cellular heterogeneity and plasticity. All these factors contribute to prominent intrinsic, as well as acquired, resistance to both radiotherapy and chemotherapy. GBMs are generally large tumors, mainly located deep within the white matter of the supratentorial part of the brain. It commonly spreads into cortex, deep nuclei or even to the contralateral hemisphere which is seen in images as a characteristic "butterfly" shape[9]. Apart from the delicate position within the brain, GBMs are also extremely diffuse and highly infiltrative tumors which make them even more difficult to remove, in spite of improvements in neurosurgery procedures. GBM invasiveness is reflected by the infiltration of tumor cells into the surrounding brain parenchyma. Unlike other tumors that disseminate through the bloodstream and lymphatic system, GBM cells spread along white matter tracts and basal lamina of blood vessels[10–12]. Moreover, glioma cells' ability to undergo intravasation into the blood or lymphatic vessels has been rarely evidenced[13] and therefore distant GBM metastases are very rare[14]. Although GBM remains localized within the brain, tumor cells invade different brain sections, affecting normal functions of the central nervous system. Hence, this life-threatening brain tumor is extremely difficult to resect completely. In addition, GBM cells show a dichotomous “go or grow” behavior. Depending on the interaction with stromal cells, communication with the extracellular matrix (ECM) and surrounding extracellular factors, such as oxygen level and nutrients availability, GBM cells can switch between a migratory and proliferative state[15–17]. This dichotomous phenotype has important implications for the efficiency of chemotherapy and acquisition of chemoresistance[18,19].

Although many GBM characteristics contribute to the resistance to current therapeutic regimens, limited and varied drug delivery across the BBB can be considered a considerable reason for the slow progress in the development of more effective therapies[20–22]. The structure of the BBB comprises physical, transport and biochemical barriers. Brain capillary endothelial cells prevent paracellular diffusion due to their tight junctions. Therefore, molecules from the bloodstream can pass the BBB only through luminal and abluminal plasma membranes of endothelial cells[23]. Many anticancer drugs that do not readily cross lipid bilayers cannot pass this physical barrier. On the other hand, lipophilic drug diffusion is prevented by transmembrane efflux transporters that constitute a drug extrusion barrier on the endothelial cells. These transporters including P-glycoprotein (P-gp; ABCB1), multidrug resistance associated protein 1 (MRP1/ABCC1) and breast cancer resistance protein (BCRP/ABCG2) actively expel drugs into the capillaries[24–26]. Among them, P-gp is the most abundant[27,28]. Thus, the BBB limits the penetration into the brain of more than 98% of small-molecule drugs, including for example paclitaxel, doxorubicin, methotrexate and vincristine[29].

Due to cellular heterogeneity and plasticity, drug resistance is mainly attributed to a small subpopulation of cells with stem cell-like properties commonly designated as “glioma stem cells” (GSC)[30]. These cells possess self-renewal capacity in vitro and in vivo and the ability to form tumors upon intracranial implantation in immunodeficient mice (Singh et al., 2004). These cells express a number of stem cell specific markers including for example Nestin, SOX2, ID1, CD15, and CD44 that maintain stem-like properties and have the ability to differentiate into multiple linages of neuronal and non-neural cells[31]. For example, as observed by live-imaging, glioblastoma stem cells may differentiate into endothelial cells and contribute to angiogenesis in GBM[32]. On the other hand, differentiated glioblastoma cells can switch to a stem-like phenotype by reprogramming the expression of major neuro-developmental transcription factors, such as POU3F2 (BRN2), SOX2, SALL2 and OLIG2[33].

Both acquisition and loss of stemness contribute to considerable plasticity of glioblastomas[34,35]. This diversity of cells gives rise to complex and pronounced intratumoral heterogeneity involved in chemoresistance, making glioblastoma a very difficult to treat malignancy.

Resistance to chemotherapy is mediated by multiple signaling pathways that are activated through different factors, either intracellular or originating from the tumor microenvironment (TME)[25,36,45,46,37–44]. Increasing evidence emphasizes the role of the TME in glioblastoma pathogenesis and response to therapy[34,47–49]. However, still a lot remains to be studied and understood.

Some of the main histological characteristics of GBM are necrotic core, pseudopalisade and vascular proliferation. It was shown that all of these zones have different molecular profiles and that cellular heterogeneity creates additional variability (microglia, astrocytes, immune cells)[50]. On the other hand, molecular features separate GBM in four groups depending on molecular alterations (classical, neural, proneural, mesenchymal), and different therapeutic approaches should be applied to each one[51,52]. Comparison of different parts of the same tumor showed that, within the same tumor, depending on the histological context, distinct molecular subtypes could be present[53–56].

Patient samples should be examined as much as possible the way they are, to get the most information about the tumor components and their correlations. New omics techniques are being developed, which allow detailed study of the tumor, preserving tissue structure. Hence, they enable the correlation between the histology and the expression of genes, proteins, metabolites, creating the complete image of the tumor[57,58]. They could allow discovering new targets and developing more biomimetic in vitro models for further studies and faster and cheaper treatment development.

Classical 2D, monolayer cultures on plastic or glass surface do not mimic complex structure of brain tissue and glioblastoma cell behavior[59–61]. On the other hand, animal studies with human xenografts and orthotropic models do not adequately reproduce the disease status present in GBM patients[59,62]. Therefore, recent studies are focused on developing tridimensional (3D) in vitro cultures to study glioblastoma pathogenesis and response to therapy more realistically considering all the effects of cell surrounding.

1.1 Intracellular factors contributing to glioblastoma chemoresistance

The majority of common chemotherapeutics, as well as radiotherapy, inflict severe DNA damage, predominantly DNA double strand brakes (DSB)[63–66]. It was shown that glioblastoma cells, particularly their CD133+ stem-like subpopulation, have enhanced activation of DNA damage checkpoint proteins (ATM, Rad17, Chk1 and Chk2) and subsequent DNA repair upon treatment, therefore causing therapy failure[67–69]. However, resistance to TMZ, as an alkylating agent, is mediated by another set of DNA repair proteins, involving increased expression of MGMT[70], and deficiency in components of base excision and mismatch repair systems[71–73].

Apart from causing direct DNA damage, chemotherapy also generates reactive oxygen species (ROS) that cause additional DNA breaks and damage of important cellular proteins and lipids[74,75]. Unfortunately, glioblastoma cells have developed the ability to resist such therapeutic assault by lowering ROS production and increasing expression of components of their scavenging system including superoxide dismutase (SOD), catalase, glutathione peroxidase (GPX), glutathione reductase (GR), Solute Carrier Family 7 Member 11 (SLC7A11)[76–78].

Normally, cells damaged upon chemotherapy would undergo autophagy (to self-repair) and/or apoptosis (to self-destruct)[79–82]. However, glioblastoma cells have developed additional defense mechanisms against therapy based on these two processes. They have enhanced pro-survival autophagy pathways (increased expression of VPS34, Beclin1, ATG5, LC3, BNIP3) and developed the ability to evade apoptosis[83–85], contributing to further tumor mass growth despite significant cellular impairments. High grade glioma stem cells were shown to have increased expression of anti-apoptotic proteins[86,87], while pro-apoptotic molecules were downregulated[88,89]. Such alterations in apoptotic machinery eventually contribute to glioma resistance to therapy[90–92].

In the very essence of the abovementioned mechanisms of chemoresistance is the deregulation of numerous signaling pathways. The most commonly altered signaling molecules in chemoresistance are involved in maintaining stem-like phenotype (Notch and Wnt/β-catenin pathways) and have pro-survival and anti-apoptotic effect (PI3K/Akt/mTOR and RAS/MAPK pathways)[92–94]. In addition, ATP-binding cassette (ABC) transporter superfamily is another class of molecules particularly important for the anti-glioma chemotherapy resistance. Glioma cells have predominantly overexpressed multidrug resistance-associated proteins (MRPs) conferring intrinsic chemoresistance[95]. High MRP1 and BCRP expression is characteristic of glioma stem-like cell population and high grade gliomas[87,95–97]. P-gp, as the best characterized ABC transporter, is also reported to be expressed to some extent in gliomas but its role in chemoresistance is still controversial. Its presence, together with that of BCRP, in the BBB appears to be the most responsible for reduced drug efficacy in glioblastoma[98,99].

1.2 Microenvironment factors contributing to glioblastoma chemoresistance

Sensitivity to anti-glioma therapy also considerably depends on different microenvironment factors, primarily hypoxia. Severe hypoxia is a major characteristic of high grade gliomas. It causes formation of pseudopalisade structures with necrotic areas, thrombotic vessels and a characteristic rim of highly migratory cells that are moving away from hypoxic regions[100]. In response to low oxygen levels, glioma cells undergo phenotypic and genetic changes that allow them to survive and even proliferate in a hypoxic environment. Hypoxic conditions predominantly promote stem-like properties of both stem and non-stem glioma cells by stimulating their self-renewal and neurosphere formation[101–103]. This hypoxia-induced response is driven by changes in the expression of hypoxia-induced factors (HIF1α and HIF2α), various downstream pro-survival signaling molecules (PI3K-Akt or ERK1/2 pathways) and numerous stemness markers (CD133, CXCR4, CD44, A2B5, OCT4, NANOG and c-MYC)[102–104]. Such stemness-like phenotype, promoted by hypoxia, additionally contributes to therapy resistance[105,106]. Moreover, hypoxia can have direct negative effect on anti-glioma therapy efficacy, by eliminating free radicals or slowing down tumor cell proliferation, as well as indirect effect mainly through HIF-1α activation. Specifically, increased HIF activity up-regulates the expression of MDR efflux transporters of the ABC superfamily which mediate chemoresistance[107,108]. Moreover, HIF-1α affects glioma sensitivity to therapy by regulating autophagy/apoptosis, metabolism, proliferation, and the tumor vasculature[109,110]. Sanzey and colleagues showed that severe hypoxia strongly upregulated the expression of glycolysis-related genes in patient-derived GBM cells that resulted in increased glycolytic activity and promoted tumor invasiveness[111].

Apart from modulating glioma cell phenotype and treatment response, hypoxia affects other microenvironment factors which additionally contribute to therapy resistance[37]. Due to the hypoxic conditions, tumor cells switch to anaerobic metabolism causing acidification of the TME. This acidic stress promotes and maintains glioma stem-like phenotype[112]. Specifically, increased expression of HIF-1α, in response to hypoxia, enhances survival of nearby endothelial cells and induces the expression of vascular endothelial growth factor

(VEGF) that further stimulates formation of new blood vessels (angiogenesis)[69,113–115]. Reciprocally, endothelial cells induce glioma stem cell state and stimulate sphere formation via Notch signaling[116,117]. They also release different factors, such as bFGF or nitric oxide, which additionally favor glioma plasticity and induction of stem-like phenotype[118,119].

In addition to interaction with surrounding cells and different factors they secrete, the ECM is another important component of the perivascular niche that determines glioblastoma cell behavior and response to therapy. The composition of brain ECM is quite unique and distinct from other tissues. Its abundant components are glycosaminoglycans, predominantly hyaluronic acid, and proteoglycans, such as heparan sulfate, while the presence of fibrous glycoproteins collagen, laminin and fibronectin is scarce and mainly restricted to blood vessels basement membrane[120]. In glioblastoma, most of these components are overexpressed and contribute to GBM invasion[121], as well as acquisition of stem-like phenotype and chemoresistance[85,122]. Moreover, changes in the ECM composition modulate its physicomechanical properties, in the first place stiffness and rigidity, which additionally contribute to increased invasiveness and chemoresistance[123–125].

1.3 In vitro 3D models of glioblastoma

Different glioblastoma 3D cell culture models were developed with the intention to recreate a TME and mimic interactions between tumor cells, different cellular components and ECM (Figure 1.1). The aim is to create biomimetic systems that are user-friendly, cost-effective and compatible with downstream analysis, to finally obtain a reliable GBM model which could be used for therapy response studies in personal medicine.

1.3.1 Types of 3D GBM cell cultures

One of the highly biomimetic GBM models, used for drug testing, is growing a tumor tissue explant in a collagen-coated Petri dish. It conserves a real structure of the tumor with all components of its microenvironment[126]. A similar model, which includes growing GBM cells on an organotypic brain slice, enables investigation of tumor invasion in healthy brain tissue[127]. Disadvantages of these models are low reproducibility and difficulties with the preservation of the tissue.

Therefore, more reproducible models of 3D cell culture were introduced and widely used in GBM research. Depending on the cell culture environment, we can distinguish between scaffold-free and scaffold-based cultures[128].

1.3.1.1 Scaffold-free models

Scaffold-free cultures are spherical multicellular aggregates that well represent different biochemical gradients, as the diffusion within them is limited. Larger aggregates develop gradients of oxygen, nutrients, growth factors, signaling molecules and molecular waste and can simulate drug penetration within a solid tumor. Scaffold-free models include spheroids and organoids.

1.3.1.1.1 Spheroids

Spheroids are the most frequently used 3D models. They successfully mimic cell-to-cell interactions. Limited diffusion within spheroids causes formation of different cellular zones: proliferating zone on the surface (sufficient level of oxygen, nutrients and signals), necrotic zone in the central part of the spheroid (lack of oxygen and nutrients, higher concentration of the waste) and quiescent zone between these two zones[129,130].

Depending on the cell line type, spheroid complexity and the method for its formation, one can distinguish between different types of glioblastoma spheroid cultures: multicellular tumor spheroids (MCTS), neurospheres, tissue-derived tumor spheres and organotypic multicellular spheroids[131]. Growing tumor cell lines under non-adherent conditions leads to cell aggregation and formation of spherical multicellular structures. There are different ways for the MCTS formation: non-adherent surface method, hanging drop method, suspension culture and magnetic levitation[132]. It is also possible to create spheroids within scaffolds and microfluidic devices, which will be discussed later.

Neurospheres (also called tumor spheres and gliomaspheres) are a special type of spheroid cultures generated from patient-derived primary GBM cells. Primary cells from GBM patients, obtained by dissociation of tumor tissue, are normally grown under suspension culture conditions, in serum-free medium, supplemented with B27, bFGF and EGF[59,133,134]. This enables spontaneous formation of neurospheres. Glioblastoma stem-like cells are a predominant component of the neurosphere, while the rest of cell subtypes are being lost[133,135].

Fragments of fresh tumor tissue from patients can be grown in vitro in agar coated flasks, without prior dissociation. Differing from tumor tissue explant mentioned above, anti-adherence agar coating allows the tissue to round up and form organotypic multicellular spheroids. This model properly represents the tumor. It conserves the TME with all cell types and ECM and better preserves the in vivo phenotype. On the other hand, its reproducibility is low and different results can be obtained, as they depend on the fraction of tumor cells that is successfully grown[136–139].

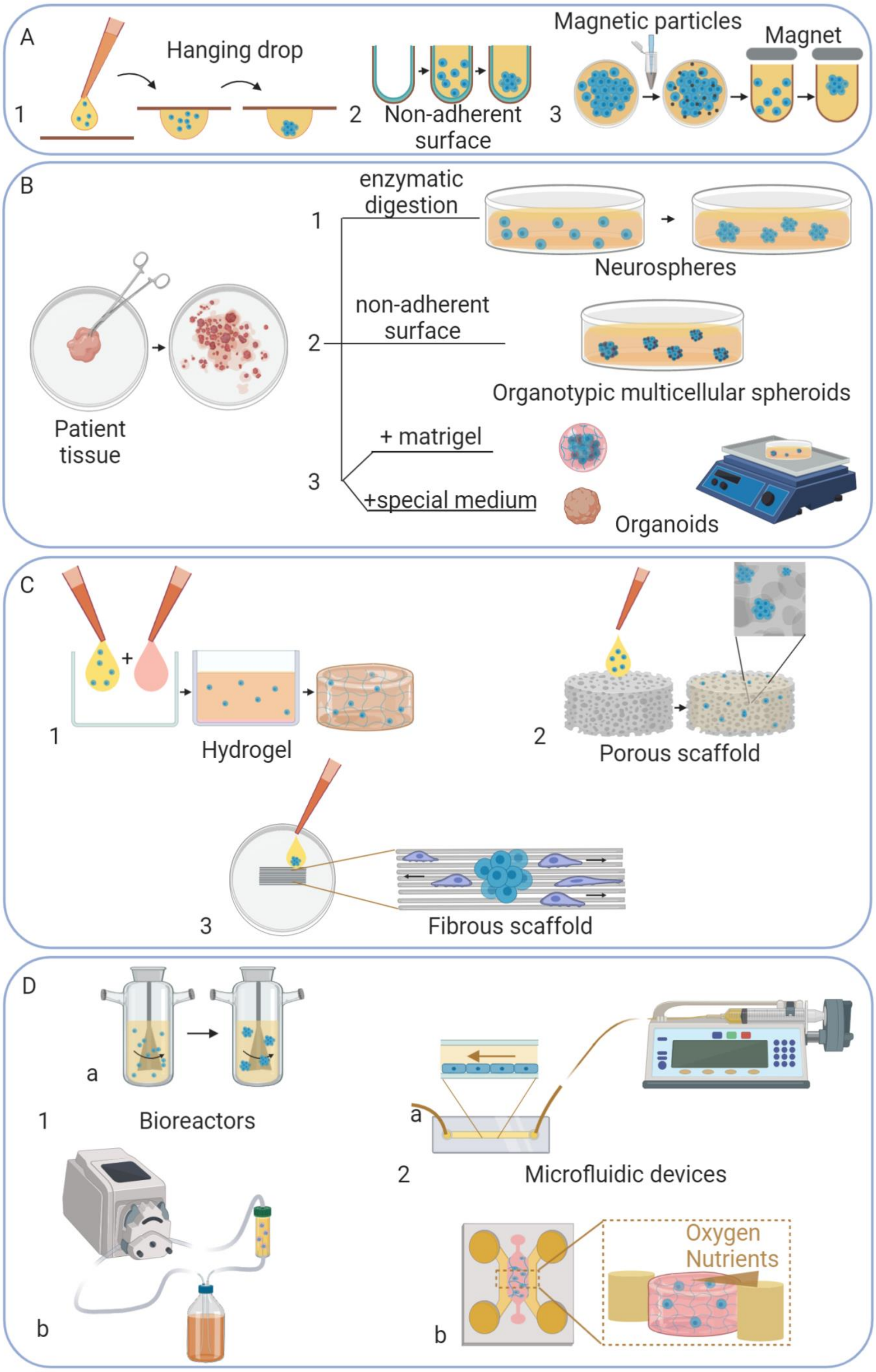

Figure 1.1 3D GBM cell culture models:
(A) Multicellular tumor spheroid (MCTS) formation: (1) Hanging drop method – Growing cells in a small volume of medium on a lid of a Petri dish permits the cells to fall to the tip of a drop, aggregate and form MCTS; (2) Non-adherent surface method – Seeding cells on a surface that is not suitable for cell attachment, leads to cell accumulation on the bottom

of the well and formation of MCTS; (3) Magnetic levitation – Incorporation of magnetic nanoparticles within the cells allows magnetic-induced cell floating and formation of MCTS on the liquid-air interface; (B) Cultures made from patient samples: (1) Neurospheres – Primary cells obtained by enzymatic dissociation of tumor tissue are grown in medium without serum and supplemented with growth factors, which promote sphere formation; (2) Organotypic multicellular spheroids – Fragments of fresh tissue, grown under non-adherent conditions, round up and form spheroids; (3) Organoids – Primary cells or tumor tissue fragments can form complex 3D structures, when embedded in matrigel or grown in special medium on orbital shaker; (C) Scaffold-based models: (1) Hydrogels – Cell suspension can be mixed with liquid polymer precursor which after cross-linking converts to solid scaffold with encapsulated cells; (2) Porous scaffolds – Cells seeded on the top of the solid scaffold enter within the scaffold and form 3D structures; (3) Fibrous scaffolds – Organized scaffold that mimics GBM invasion pathways; (D) Cultures with medium flow: (1) Bioreactors: (a) Stirring bioreactor – Constant agitation of cells prevents cell attachment to the surface and promotes spheroid formation; (b) Perfusion bioreactor – Scaffold based culture connected to peristaltic pump permits the simulation of physiological mass transport; (2) Microfluidic devices: (a) Simple microfluidic device connected to syringe pump for investigation of sheer stress effects; (b) Gradient microdevice – Hydrogel with embedded cells is filled within the central chamber, while lateral channels are perfused with medium, that way permitting formation of different gradients. Created with BioRender.com.

1.3.1.1.2 Organoid culture

Organoids are complex 3D structures that better represent the heterogeneous structure of the tissue[59,140–142]. They are usually obtained by growing primary stem cells or pluripotent stem cells, which are able to differentiate in various cell subtypes and to self-organize, creating specific tissue structures. A growth medium containing specific factors or ECM components are needed to promote cell differentiation and organization[143]. The first glioblastoma organoids were formed by embedding tumor cells in matrigel and growing them in a stem cell medium on orbital shaker[144]. The disadvantages of these organoid cultures are the long formation time, lack of vascularization and the absence of complete maturation of the reproduced organ[128,143]. Recently, Jacob et al., developed a new method for organoid formation[145]. Patient derived tumor tissue is cut into small pieces and grown on an orbital shaker in serum-free medium without exogenous addition of growth factors and ECM, hence preventing cell selection and allowing conservation of molecular signatures of parental tumor and different cellular components of TME for prolonged time. Limitations of this model are decreased rate of organoid formation from IDH-1 mutant and recurrent tumors as well as decrease of vasculature and immune cells after long culture[145].

1.3.1.2 Scaffold-based models

Scaffold-based models comprise different components of GBM microenvironment in an in vitro system. They are based on diverse biocompatible materials that give support to cells and mimic biochemical and mechanical properties of ECM. Within scaffolds we can study cell growth, invasion, cellular interactions with its microenvironment and the effects of potential therapy.

Scaffolds can be made from natural and synthetic materials[128,132,146]. Natural material-based scaffolds consist of ECM-derived biomolecules, such as hyaluronic acid (HA)[147], collagen[148–150], fibrinogen[151], basement membrane extracts[152,153] and even decellularized patient tissue[154]. Cells grown in these scaffolds are able to receive transduction signals and to respond to changes in the microenvironment. The disadvantage of these materials is that, as they originate from mammalian organisms, they can contain pathogens, variations in soluble factors and protein concentrations, so the results obtained in such scaffolds can vary. In order to overcome these problems, non-mammalian polymers are used (alginate and chitosan)[155–157], as they are also biocompatible with GBM cells, but are non-immunogenic. Also, different synthetic polymers are being developed. These polymers are inert, their properties can be highly controlled and they give reproducible results. As they do not have cellular adhesion sites, bioactive proteins can be attached, such as RGD functionalized proteins (with the adhesive peptide of tri-amino acid sequence, arginine-glycine-aspartate), in order to enable cellular adhesion or biodegradation[158,159]. Some of the synthetic polymers used are polystyrene[160], polydimethylsiloxane (PDMS)[161], polylactic acid[162], poly(ethylene-glycol) (PEG)[163–165], polycaprolacton (PCL)[166].

Depending on the 3D structure of the scaffold they can be divided into hydrogels, fibrous scaffolds and porous scaffolds[128,167]. Hydrogels are microporous polymer networks that have high water absorption capacity. Physical or chemical cross-linking of liquid precursors leads to the creation of solid scaffolds. This permits the encapsulation of the cells within the scaffold at the beginning of the fabrication process. As hydrogels are rich in water, the transport of oxygen, nutrients and growth factors is possible. Depending on their composition, hydrogels can have similar biophysical and biochemical characteristics to ECM, hence presenting a more realistic in vitro model and the most frequently used one[135,168].

Fibrous scaffolds mimic fibrous structures of white matter tract or blood vessels, which serve as invasion routes for GBM cells[167]. They are made by electrospinning of synthetic polymer solutions, such as PCL[169,170], polystyrene[171], polyacrylonitrile[172] or PDMS[161]. Cells are seeded on the top of the scaffold, they attach on the surface of the material and their migration along scaffold can be followed.

Porous scaffolds are solid scaffolds, composed of interconnected pore network. They provide a physical support to cells and permit formation of 3D structures. Cells are seeded on the top of the scaffold and they enter it passively or by migration, attach to the walls, proliferate, cluster and form spheroids. Different techniques can be used for scaffold fabrication. Some of them are freeze drying, micro molding, gas foaming, solvent casting/particulate leaching and bioprinting, as the most advanced method[128,146].

3D bioprinting is a manufacturing process that enables creation of tissues and organs using different hydrogel-based biomaterials (bioinks) and cells. The fabrication process requires digital design of the desired structure and segmentation of the image, in order to enable printing of successive layers of material and cells and formation of 3D systems[173]. This process is highly controlled and facilitates precise distribution of different cell types and ECM, thereby mimicking TME with its cellular, biochemical and biophysical components. Using 3D bioprinting, one is able to obtain complex, highly reproducible 3D cell cultures. However, depending on the parameters of the printing processes, it can provoke cell death or changes of phenotype; thus, it is important to optimize the conditions[132,174]. Recently, more bioprinted models of GBM are being developed, as the technique has great potential for GBM studies[175–184]. Furthermore, additional components of TME were added to GBM bioprinted models, oxygen gradients were created[184] and different cell types were included, such as macrophages[176,177,181], astorocytes[180,181] and vascular endothelial cells[184].

1.3.1.3 3D GBM cell cultures with media flow

In order to reconstitute real tumor conditions more faithfully, researchers have developed complex 3D cell cultures that introduce media flow through the system. Depending on the design of these perfusion 3D cultures, the presence of media flow, mimics blood flow through the vessels and/or interstitial fluid flow. Bioreactors and microfluidic devices are examples of these complex 3D cell cultures, developed also for GBM studies.

Bioreactors are closed systems in which biological and biochemical processes are under strictly controlled environmental and operating conditions (e.g., temperature, pH, pressure, shear stress, nutrient supply, oxygen and CO2 concentration, metabolites and regulatory molecules)[185–188]. Since bioreactors provide us with a high degree of control, reproducibility and automation, they have found applications in various fields. Bioreactors are also designed and used for growing cancer cells and scaffold-based tumor tissues as a new 3D model of malignant neoplasms.

Bioreactors for tumor tissue engineering have to be made from bioinert and biocompatible materials. The whole system should operate under sterile culture conditions and allow specific mass transport and nutrient supply. Also, it should be transparent to allow visualization and use of fluorescence and optical imaging of tumor tissue[189,190].

Depending on the physicochemical parameters to be controlled and the desired outcome of the experiment, many different types of bioreactors have been developed and used for tumor tissue engineering. They can be grouped into the following types: bioreactors with static cultivation systems, stirring bioreactors, rotary bioreactors, hollow-fiber bioreactors and perfusion bioreactors. Detailed description of these bioreactors and their application in tumor tissue engineering have been previously reviewed[190].

Bioreactors have been mainly used to cultivate a large amount of human GBM-derived cancer stem cells (GSCs), hence circumventing the limitations of massive cell propagation in conventional in vitro 2D cell cultures[191]. The type of bioreactor most commonly used for expansion of CSCs of various tumors, including GBM, is the stirring bioreactor. This type of bioreactor provides dynamic mixing of the growth medium and significantly improves mass transfer between cells and the culture medium. However, these conditions place the cells under the constant influence of fluid-induced shear stress[189,190]. Recently, perfusion bioreactors have been used as a new strategy for improving the 3D in vitro models of the GBM. This type of bioreactors achieves the most accurate simulation of mass transfer in a living organism[192]. Combining scaffold-based 3D cell culture and perfusion bioreactor has found application in producing large amounts of glioblastoma tumor-initiating cells (TICs) required for drug screening, as well as for basic cancer research[163,193].

Microfluidic platforms or chips are microfabricated bioreactors that enable growing cells in micrometric chambers within well controlled physiological-like conditions. They consist of one or more fluidic channels where small volumes of liquid and low number of cells can be handled[194]. Depending on the characteristics of the device, we can mimic interactions between cells, between cells and ECM, as well as to mimic biophysical and biochemical characteristics of the TME, such as gradients of nutrients, oxygen and signaling molecules[195]. As the laminar flow is present within the channels of the microdevice, there is no fluid mixing and molecules travel through the device by diffusion[196].

The simplest microfluidic devices consist of a simple channel that permits the 2D growth of cells. They are used to investigate flow-induced shear stress effects, migration, nutrient gradients and drug effects[197–201]. As mentioned above, microfluidic platforms can be used for spheroid formation. These devices are made from anti-adherent materials and their geometry promotes capturing of the cells within microwells, their aggregation and spheroid formation[202]. Within some devices, cells are embedded in hydrogels and thus, by providing physical and biochemical components of ECM, a more adequate biomimetic model is created[195,203–206].

Microfluidic devices permit a real time monitoring of cell culture. They can be used for different purposes, to investigate cell proliferation, metabolism, migration and invasion, angiogenesis, immune system function and most importantly therapy response[195,203,206–208].

1.3.2 3D glioblastoma models specifically used for anti-glioblastoma drug screening

Most of the studies that examined anti-glioblastoma effects of different chemotherapeutic drugs, as well as novel compounds in a 3D setting used spheroids grown in medium as a model system. Some examples of drugs/compounds tested for their anticancer effect in gliomaspheres are listed in Table 1.1.

Recently, Quereda and collaborators developed a high-throughput spheroid-based proliferation assay for testing cytotoxicity of up to 3,300 compounds simultaneously on GSC cells[209].

Although simple spheroid systems in growth media are widely used for drug screening in 3D GBM cultures they have significant limitations, primarily the simplified architecture that lacks complex TME conditions. Therefore, in several publications drug effects on glioblastoma cells were tested in different 3D scaffolds mimicking natural ECM (Table 1.1). In most of these studies the authors examined the invasion of 3D culture in response to various compounds, such as inflammatory cytokines IL-1β and TNFα[210], FasL neutralizing antibody[211] or drug combination of imatinib and docetaxel[212]. However, two research groups, An et al.[213] and Iwasaki et al.[214], performed more comprehensive studies and investigated then effects of vorinostat (histone deacetylase inhibitor) and TNFα, respectively, on 3D cell culture growth and viability, morphological and adhesive characteristics and gene expression in addition to invasive properties.

Table 1.1 3D GBM cell cultures used to study anti-glioblastoma drug activity

3D cell cultures	GBM cell types	Drugs	Reference
Scaffold-free cultures			
Spheroids grown in media	U251, primary cell lines	Acetazolamide with TMZ	[215]
	U87, primary cell lines	RO4929097 with TMZ and radiotherapy	[216]
	U87	Curcumin and DOX in micellar carrier	[217]
	U251	Pyrrolidine-2 and curcumin	[218]
	T-98G	Curcumin and TMZ in magnetic nanoparticles	[219]
	U251	Metformin and Ara-a	[220]
	LN229, U87, T-98G	Sodium Selenite with TMZ	[221]
	U87	^{225}Ac in polymersomes	[222]

	Primary cell lines	Niclosamide with TMZ	223
Spheroid-based high-throughput platform	U87, primary cell lines	Simultaneous cytotoxicity testing up to 3300 compounds	209
Organoids grown in media	Patient tissue	TMZ with radiotherapy, gefitinib, trametinib, everolimus	145
Scaffold-based cultures			
Single cells in Type I collagen 3D matrix	U178	IL-1β and TNF-α	210
Spheroids in Matrigel	U87, U251	APG101	211
Spheroids in collagen gel	SNB-19, primary cell lines	Imatinib and Docetaxel	212
Spheroids in collagen type I 3D gel	LN18, F98, C6, F98EGFR-vIII, U87	Vorinostat	213
Single cells in Matrigel	Primary cell lines	TNF-α	214
Organoids in hyaluronic acid-collagen hydrogel	Patient derived cells	Dacomitinib	179
Single cells in collagen gel	U251, U87	Simvastatin with TMZ	224
3D platforms			
High-throughput alginate micropillar and microwell chip platform	Patient derived cells and normal human astrocyte cell line	70 compounds simultaneously tested	225
Spheroids forming microfluidic device with PEGDA hydrogel	U87	Pitavastatin and Irinotecan	226
Spheroids forming microfluidic device with PEGDA hydrogel	Patient derived cells	TMZ and bevacizumab	227
Single cell separation microfluidic device	U251	Vincristine	228

Lee et al., constructed a type of 3D platform with alginate matrix for high-throughput drug cytotoxicity and efficacy testing on both GBM cells and normal astrocytes[225]. This 3D chip with micropillars (for growing cells in alginate matrix) and microwells (containing drugs) is suitable for simultaneous screening of 72 compounds in 7 replicates[225]. Recently, technological advances enabled us to perform more accurate and reliable drug testing in complex 3D cultures, such as in microfluidic devices, which more faithfully recapitulate glioblastoma TME and its conditions observed in patients. Examples of microfluidic devices specifically developed for anti-glioblastoma drug screening are summarized in Table 1.1.

Fan and colleagues developed microfuidic-based brain cancer chip for high-throughput testing of multiple-simultaneous drug response on GBM spheroids in PEGDA hydrogel[226]. They validated generation of drug concentration in chips by testing single and combined effects of pitavastatin and irinotecan on U87 spheroid cell viability. Recently, the same group of authors engineered an improved version of the brain cancer chip that prevents the diffusion of any drug molecule across channels[227]. As a proof-of-concept experiment, they tested viability effects of concentration gradient generated by simultaneous application of temozolomide and bevacizumab on three GBM patient-derived cell spheroids. To consider the effect of cellular heterogeneity on drug treatment response, Pang and collaborators designed a microfluidic platform for single-cell separation based on cell biomechanical properties. In this system, the authors were able to determine the level of vincristine sensitivity according to the cell size and degree of deformability[228].

1.4 Effects of 3D culture on GBM gene expression and phenotype

Cell culture dimensionality significantly affects glioblastoma cell phenotype, such as morphology, migration, proliferation, differentiation and stemness (Table 1.2). Numerous studies have shown that glioma cells have an altered morphology in 3D systems compared to 2D cell cultures. In 3D matrices, cells are present in a spindle or round form compared to flattened epithelioid shape when grown in monolayers[156,160,182,229–234]. Unlike cells in 2D cultures that lack polarity, spindle cells of 3D cultures contain one or two oriented spindly protrusions[229]. This is particularly evident for highly invading cells that present a neural progenitor-like phenotype with a round small cell body and a long leading process, as shown in experiments with tumor spheres grafted into a 3D collagen matrix[235]. Moreover, in 3D scaffolds, glioblastoma cells tend to form multi-cellular clusters and to aggregate into tumor cell spheroids[236,237], while cells cultured on 2D surfaces have an epithelium-like morphology and grow into sheets[234]. This colony formation ability in 3D culture depends on the GBM cell type and characteristics of 3D scaffold, such as pore size[230]. As observed in the study of Wang et al., cells form tighter spheroids in 3D scaffolds with closer connections and have more abundant secretory granules on the cell surface[238]. Those cells were also richer in mitochondria and rough endoplasmic reticulum and had a higher number of longer microvilli.

Apart from influencing cell morphology, the 3D culture environment also enhances the migration ability of the glioma cells, compared with the 2D plated cultures[230]. The movement pattern in 3D cultures significantly depends on the presence of the tumor core; without a tumor core, cells migrate randomly, while existence of tumor sphere induces oriented cell migration[235]. It was shown that migration of U87 glioblastoma cells in a 3D environment is driven by mesenchymal-amoeboid transition upon Rac1 GTPase inhibitor treatment[229].

Glioblastoma cell proliferation is generally slower in 3D compared to 2D cultures[156,160,175,230–233,236,237,239], and it is accompanied by decreased expression of the proliferative marker Ki67[230]. According to the Gomez-Roman study, this behavior can be changed in response to VEGF supplementation which increases 3D cell proliferation but has no effect on 2D growth conditions[160]. It was observed that in a 3D environment, GBM cells accumulate in G0/G1 cell cycle phase but without significant difference in apoptosis rate compared to 2D culture, suggesting their decreased proliferation and increased quiescence in 3D scaffolds[237]. Although 2D culture initially had higher proliferative capacity, it was shown that upon prolonged 2D cultures (longer than 10 days), cellular proliferation decreases after some point of time and then proliferation rate of 3D cultures becomes higher[175,182,234].

Fernandez-Fuente and colleagues first showed that there is no difference in GBM cell differentiation level (GFAP level) between 2D and 3D cultures[240]. However, a later study of Lv et al., reported decreased GFAP level as a marker of increased dedifferentiation of glioblastoma cells in 3D compared to 2D culture[237]. Several observations are consistent with the later finding and show that cultures in different 3D scaffolds have a greater proportion of stem cell-like cells, with CD133 positive phenotype, compared to monolayer cultures[182,232,234,238].

Along with increased stem-like phenotype, angiogenic potential of GBM cells is also altered in 3D compared to 2D cultures. For example, accelerated vasculature formation, with enhanced recruitment of CD31 positive cells, was observed in U87 tumors from cells pre-cultured in 3D chitosan alginate scaffolds[156]. Moreover, complexity of 3D culture can affect angiogenic potential as well. Wang et al., reported that 3D bioprinted GSC culture had increased VEGFA secretion and formed more tube-like structures than conventional GSC suspension culture[238].

Corresponding to increased stemness, three-dimensionally grown glioblastoma cells also have increased in vivo tumorigenic potential. They form larger tumors that are developing much faster, compared to tumors derived from monolayer cell cultures[182,232,234]. However, Kievit et al., reported that this initial rapid tumor growth is not sustainable and after some time tumors developed from 3D pre-cultured cells began to grow at a similar rate as the 2D pre-cultured tumors[156].

As cell appearance and behavior is determined by gene expression, it was reasonable to assume that the dimensionality of cell culture would also significantly affect regulation of gene expression. Indeed, when grown in 3D cultures, glioblastoma cells showed different levels of expression of various genes compared to culturing in monolayers[239,241]. Numerous studies have observed altered expression of several classes of markers (mRNA and/or protein) in 3D cultures, including:

- Stemness related markers - most frequently general stemness markers such as CD133[166,230,232,234,237,238,242], CD44[166,232,234], Nestin[166,175,230,232,234,236,242], Nanog[230,237], SOX2[230,237]; Oct4[230,242]; Snail[232,234], as well as less frequently observed Frizzled 4, GLI, HES[232], LIN28A, LIN28B, CXCR4 and CSPG4[243], RHAMM[166], Musashi-1[236]; interestingly, the degree of overexpression of some stem-related genes, such as MSI1, MSI2 and BMI-1 and c-Myc, was shown to be cell type dependent in 3D environment[230];
- Markers of glial differentiation and neural development - β-tubulin III[175] and GFAP[175,236]; however, there is inconsistency in the literature regarding GFAP because some authors reported no difference in its level between 2D and 3D cultures[232];
- DNA damage repair genes – MGMT[237];
- ABC transporters - ABCG2[236] and ABCB1[243], although Lv et al., reported no significant alterations in ABC transporter gene expression in 3D compared to 2D environment[237]
- Markers related to invasion and EMT - MMP1[230], MMP-2[156,230,236,244], MMP3, MMP7[230], MMP-9[236,244], N-cadherin[230,232], TWIST1[236], Twist2, Snai1 and Snai2[232], vimentin[230]; it is worth mentioning that E-cadherin levels are suppressed upon 3D cultures[232]
- Markers of angiogenesis and response to hypoxia - HIF-1α[234,236,238,242,244], VEGF[156,175,244], laminin[156], fibronectin[156,244], VEGFR2, and CD31[238]
- Cell-cycle related genes - p21, p27, CCNA1, CCNB1, CCND1 and CCNE1[230].

Excluding specific genes/proteins, whole signaling pathways are also differentially regulated in 3D compared to 2D GBM cellular systems. Specifically, it was reported that components of pro-apoptotic signaling cascade (caspases, poly (ADP-ribose) polymerase (PARP) and p53) were downregulated, while anti-apoptotic signaling factors (PDL-1 and Livin) were upregulated in 3D collagen scaffold[230]. In addition, key proteins of Wnt, SHH and Notch signaling pathways (Notch1, 2 and 3, Wnt3a, Wnt5a and SHH) were also highly expressed in this 3D system[230].

1.5 Effects of the TME on GBM cell phenotype in 3D models

Besides dimensionality, other characteristics of 3D culture also significantly shape glioblastoma phenotype (Table 1.2).

1.5.1 Composition of 3D scaffolds

In the first place, the type of 3D scaffold material, its composition and formulation, considerably determines glioblastoma behavior and gene expression. For example, patient-derived primary GSC exhibited opposite migratory profile in Matrigel and collagen scaffolds, moving in spherical multicellular aggregates in Matrigel versus single elongated cells within collagen matrix[245]. The type of collagen used for scaffold fabrication also affects GBM cell morphology. Cells gain a round morphology in collagen-IV, while in collagen-I/III, with the strong fibrillary structure, they acquire spindle shape and prominent migratory phenotype[150].

Addition of ECM components to 3D scaffolds considerably influences GBM cell characteristics. Incorporation of HA in 3D collagen-hydrogels causes cells to get a more rounded morphology and to decrease migration[150,245]. Pedron at al., showed that addition of methacrylated hyaluronic acid (HAMA) to adhesive (GelMA) and non-adhesive (PEG) 3D hydrogels induced cell clustering and increased expression of invasion-related genes (VEGF, HIF-1, MMP-9, and Fn)[159]. Several groups also reported that the presence of HA in 3D scaffolds increased expression of stem cell markers, particularly CD133, and EMT-related genes in GBM cell lines[166,234,246], also leading to increased tumorigenicity in nude mice[234]. Accordingly, Li et al., developed 3D HA scaffold-based bioreactor (AlgTubes) for scalable culturing of high quality and high quantity glioblastoma TICs[193]. They made coaxial alginate tubes filled with HA and dispersed primary glioblastoma cells. Such a bioreactor system with a high HA content ensured efficient mass transport, protection from the hydrodynamic pressure, efficient expansion of glioblastoma TICs and maintenance of stem phenotype[193].

Similar to HA, addition of agarose to collagen matrices also promoted a round morphology and amoeboid motility and slowed down migration of GBM cells due to increased elasticity, reduced porosity and presence of steric barriers within such composite 3D scaffold[149]. Excluding HA, the presence of other ECM components, such as laminin, contribute to altered GBM behavior in 3D cultures. Coating of electrospun polystyrene (ESPS) scaffolds with different laminin isoforms was shown to increase expression of integrin alpha 6 and beta 4, as well as several stem markers and ABC transporters in U251 cells[243]. Additionally, inclusion of laminin in polyacrylonitrile scaffolds leads to higher migration and lower proliferation[172].

1.5.2 Biomechanical properties of 3D scaffolds

The addition of ECM components and ligands to 3D scaffolds, as well as crosslinking 3D scaffold material, alters biomechanical properties, stiffness and porosity, of the scaffold causing changes in GBM cell behavior. For example, Kaphle et al., showed that 8S-StarPEG, used to crosslink collagen, could increase hydrogel viscosity and decrease collagen degradation and cell migration[247]. Generally, increasing hydrogel stiffness causes cells to be more rounded and proliferate less and it also inhibits their motility and invasion[150,158,248–251]. It is interesting to note that, in spite of the general behavior pattern, different glioblastoma cells may act differentially in the same 3D matrix[147], which is particularly evident for primary glioblastoma cells[252].

Altering scaffold stiffness and crosslinking also affects gene expression. Increased expression of HIF-1, VEGF, and MMP-9, as well as reduced CD44 expression, was observed in response to greater stiffness and/or crosslinking density[158,244]. Apart from stiffness, varying scaffold porosity may influence GBM cell gene expression. In the Jia et al., study, pore size of the 3D collagen scaffold significantly and differentially affected expression of malignancy, stemness, cell cycle and EMT-related markers in three glioblastoma cell lines. This effect was mainly observed at the protein level rather than at the mRNA level, but without clear influence on their biological functions (proliferation, colony formation, migration and invasion)[230].

In more complex 3D systems, media perfusion is introduced to mimic interstitial flow (IF) in tumors. Presence of IF generates fluid shear stress (SS) which can alter glioblastoma cell behavior and gene expression, even though it is of lesser magnitude in tumor tissue than in vasculature system. Panchalingam et al., developed stirred-suspension bioreactor protocols for growing human-GSCs in suspension culture under low- and high-shear stress forces[253]. High SS conditions resulted in a higher cell expansion and lower mean diameter of neurospheres. Also, the size of the neurospheres formed under high-shear stress conditions was more uniform, suggesting that high-shear GSC tissue may lead to homogeneous cell culture morphology. It was previously shown, using a 3D modified

Boyden chamber with media perfusion, that SS either induced cell death or decreased cell motility which was accompanied by downregulation of MMP-1 and MMP-2 activity[205]. However, later studies have shown that IF stimulates glioblastoma cell invasion, mediated by CXCR4-CXCL12 chemotactic signaling and/or HA receptor (CD44)-dependent mechanosensing[254,255].

1.5.3 Induction of hypoxia

Hypoxia, as one of the major hallmarks of glioblastoma as well as solid tumors, is an important microenvironment factor that should be mimicked in 3D cultures in order to study GBM behavior and response to therapy in the most comprehensive way[106,256]. Therefore, several studies have investigated its effects on 3D GBM cell culture phenotype. Xu and colleagues studied the effects of 1% and 0.2% oxygen levels on GBM cells in PDMS microfluidic chip with collagen hydrogel[116]. They observed increased induction of EMT and migration under hypoxic conditions, as well as upregulated expression of HIF-responsive and EMT-associated genes. However, the effects on cell proliferation depended on the degree of oxygen levels. At an environment of 1% O_2, cell proliferation was increased whereas under highly hypoxic conditions (0.2% O_2) it was decreased. Similar results, namely increased invasion, mesenchymal transition and spheroid growth and expansion, were observed by mimicking *in vivo* hypoxia conditions using a genetic approach, by transfecting HIF1α or HIF2α into GBM cells[257]. However, during long incubation (in 7 days) of hypoxic 3D culture of patient-derived glioblastoma cells, the size of spheroids did not change over time albeit they were dramatically smaller than under normoxia at the end of cultivation period[258]. In these 7-day spheroid cultures, cellular proliferation marker was mainly decreased, and hypoxia-induced markers (HIF-1α, carbonic anhydrase IX, VEGF) were upregulated under hypoxic conditions compared to normoxic conditions, while expression of stem cell markers varied across spheroid cultures in response to hypoxia. Furthermore, Ayuso et al., developed a microfludic device that enabled generation of both oxygen and nutrient gradients within 3D cultures with the possibility to monitor cell death, viability, proliferation and ROS production[195]. Using this platform they were able to mimic blood-vessel obstruction and consequently oxygen and nutrient deprivation, therefore inducing cell migration and formation of the characteristic pseudopalisade structure within 3D cell culture[203]. Moreover, detailed proteomic analysis of 3D GBM cell cultures revealed that proteins and phosphoproteins are differentially expressed in response to hypoxic conditions[241]. Namely, both pro-survival and pro-apoptotic proteins were activated, as well as migration-associated proteins, while the amount of proteins promoting cell cycle was reduced.

1.5.4 Nutrient deprivation

Effects of nutrient supply on GBM cell phenotype were also examined in the study of Panchalingam et al.[253]. In their stirred-suspension bioreactor-based culture of human GSCs, the authors introduced different feeding strategies and examined the effect that the 2-day and 6-day fed-batch (40% medium replacement every 2 or 6 days) had on the expansion and phenotype of human GSC expanded cells. The results showed that the 2-day fed-batch mode resulted in the highest expansion after 32 days of culture (90 -fold cell expansion), larger neurosphere diameter, enrichment of CD133+ cells and maintenance of their genomic and phenotypic characteristics[253].

1.5.5 Introduction of stromal cells

The complexity of the GBM TME is particularly reflected in the presence of various stromal cells and their intense interaction with tumor cells. Therefore, numerous models were developed to study GBM co-cultures with various stromal constituents in a 3D setting. So far, most extensively were investigated the 3D GBM co-cultures with endothelial cells. Co-culturing glioblastoma and HUVEC cells in 3D hydrogels was shown to stimulate overall co-culture growth throughout the time, especially when the proportion of GBM cells in co-culture was increased[259]. The presence of glioblastoma cells in 3D hydrogels enhanced proliferation, sprouting and migration of HUVEC cells[260–262]. Such stimulation of angiogenesis is mediated through VEGF secretion by glioblastoma cells or exogenously added VEGF at low concentrations[260]. This effect was even more pronounced under hypoxic conditions[260]. On the other hand, HUVEC cells slowed down the growth rate of GBM cells, caused them to form spheres around or on the top of endothelial cells[246] and promoted their invasive phenotype[263]. In the novel 3D model of Wang et al., adult patient-derived GBM tumor xenograft cells were shown to have significantly increased cell proliferation in the presence of mouse brain microvascular endothelial cells encapsulated in alginate microfibers mimicking microvessels in hydrogel[264]. Co-culturing GBM and endothelial cells in 3D models induced the acquisition of GBM stem-like phenotype with increasing expression of corresponding markers CD133, CD44 and Id1[246]. Recently, McCoy and colleagues showed that enrichment in GBM stem cell population and their increased invasiveness were mediated by interleukin-8 signaling in 3D models of patient-derived GBM spheroids co-cultured with brain endothelial cells[265], while Truong et al., proved in 3D organotypic microfluidic platform that these effects of microvasculature environment on patient-derived glioblastoma cells involved activity of CXCL12-CXCR4 signaling[266]. Similarly, Wang et al., reported that endothelial cells increased the expression of CXCR4 in GBM cells in their 3D co-culture system[264]. Co-culturing also affected the expression of several other groups of genes and proteins: induced expression of angiogenesis related genes, such as PECAM1/CD31, KDR/VEGFR2, and PIK3R1[259], induced the expression of differentiated cell marker tubulin β3 (TUBB3), upregulated expression of cell–ECM adhesion-associated proteins (integrin α2, integrin β3, type II collagen α1 and vitronectin) and downregulated the expression of genes associated with cell–cell adhesion such as cadherin 1 and catenin α2[263]. Ngo and Harley established a tri-culture comprising of U87 cells, HUVECs and normal human lung fibroblasts (NHLFs) and explored their interaction in 3D hydrogel depending on the ECM composition[267]. This study revealed that U87 cells arranged in close proximity to endothelial cells and their morphology changed from rounded in the absence of HA to elongated in its presence. On the other hand, U87 cells induced the regression of the microvasculature network in a cell density- and time-dependent manner, irrespectively of HA presence.

Other stromal cells also significantly influenced GBM cells behavior in 3D co-culture models and *vice versa*. According to Kievit and collaborators, astrocytes affect GBM cells similarly to HUVEC cells. They slowed down GBM cell growth rate when cultured in a higher cell ratio (astrocytes:GBM 5:1), stimulated them to form spheres and promoted their stem-like phenotype[246]. On the other hand, when grown in a ratio 1:1 in HA-gelatin hydrogel, astrocytes promoted tumor cell proliferation[268]. 3D GBM co-cultures with normal astrocytes showed that ECM molecules secreted by GBM cells increased glial fibrillary acidic protein (GFAP) expression in astrocytes, while astrocytes secreted soluble factors that increased GBM cell migration[269]. Moreover, it was demonstrated in the study of Gritsenko et al., that 3D astrocyte scaffold stimulated GBM cell invasion, both along astrocyte layers and through the scaffold[270]. In more complex 3D systems developed by Herrera-Perez et al., human endothelial colony forming cells were introduced to co-culture of various patient-derived cell lines and astrocytes to investigate their mutual effect on GBM cell invasion[271]. Astrocytes significantly induced invasion of all three examined GBM cell lines. However, addition of endothelial precursor cells had diverse effects on invasion depended on the cell type and their genetic background.

Mesenchymal stem cells (MSC) also modulated the GBM phenotype in corresponding 3D co-culture models. MSC promoted GBM cell proliferation in transwell chamber system either through a TGFB1-mediated paracrine signaling or by direct interaction, independently of TGFB1 cytokine secretion[272]. Breznik et al., observed that glioblastoma cell lines increased MSC motility when co-cultured in collagen I or matrigel. On the other hand, MSC had a differential effect on GBM cell invasion depending on the cell type, suppressed the invasion of U87 cells but increased the invasion of U373 cells[273].

Immune cells as important constituents of the tumor stroma also influence GBM cell invasion. For example, Coniglio et al., showed that tumor associated macrophages (THP-1 cells) significantly induced invasion of human glioblastoma cell line U87 and similarly rat microglia stimulated invasion of murine glioblastoma cell line GL261 in 3D matrices[274]. Besides, human microglial cells were shown to promote GBM cell proliferation[275]. Cui and colleagues went a step further and developed 3D tri-culture microfluidic angiogenesis platform to investigate the interaction between GBM, endothelial cells and immune cells[276]. They observed that GBM cells switched uncommitted macrophages into macrophages with immunosuppressive phenotype. These tumor-associated macrophages further stimulated sprouting and angiogenesis of co-cultured endothelial cells[276]. Tang et al., developed a tetra-culture model with GSC, astrocytes, neural precursor cells and macrophages. This system supports the upregulation of different glioblastoma signatures, such as invasion, angiogenesis, hypoxia and stemness. On the other hand, macrophages in a co-culture system are polarized to M2 phenotype, showing the mutual effect of cellular components of TME[181].

Table 1.2 Effects of 3D cell culture and microenvironment on GBM cell phenotype.

Cell characteristics	**Properties of 3D cell culture**									
	Third dimension	**Inclusion of ECM components in 3D scaffold**	**Stiffer scaffold**	**Interstitial flow**	**Hypoxia**	**Nutrient supply**	**Endothelial cells**	**Astrocytes**	**Mesenchymal cells**	**Immune cells**
Morphology	Spindle/ round[1]	Spindle/ round[2]	More round	More homogeneous	ND	ND	Round/ elongate[2]	Round	ND	ND
Proliferation	-	ND	-	ND	+/-[3]	+	-	+/-[2.4]	+	+
Migration	+	+/-[2]	-	ND	+	ND	ND	+	ND	ND
Invasion	ND	+	-	+	+	ND	+	+	+/-[5]	+
Stemness	+	+	ND	ND	ND	+	+	+	ND	+
Angiogenic potential	+	ND	+	ND	ND	ND	+	ND	ND	+
Tumorigenic potential	+	+	ND	ND	ND	ND	ND	ND	ND	ND
Therapy resistance markers expression	+	+	ND	ND	ND	ND	ND	ND	ND	ND
Apoptotic factors expression	Pro – Anti +	ND	ND	ND	Pro +	ND	ND	ND	ND	ND

+ increased; - decreased; ND – not determined; 1 depending on 3D cell culture model; 2 depending on scaffold composition; 3 depending on O2 concentration; 4 depending on seeding ratio; 5 depending on cell type

1.6 Effects of drug treatment on GBM cells in 3D models

Regardless of the type of 3D GBM culture used in drug screening, they are generally more resistant to drug treatments than monolayer cultures and therefore more closely resemble chemotherapy response in GBM patients. A number of studies has investigated the difference in response to drugs between 2D and 3D cultures and some examples are listed in Table 1.3. Regarding drug resistance development, Han et al., constructed a specific microfluidic device for the detection and study of drug resistance acquisition in GBM[197]. This Cancer Drug Resistance Accelerator (CDRA) chip consists of 488 hexagonal microchambers with two microchannels for antiparallel supply with drug and media. It was designed to generate a drug concentration gradient and observe the emergence of drug resistant cell populations throughout the time. Different mechanisms were reported to underlie the development of drug resistance in 3D cell cultures. Ayuso et al., observed that TMZ had a mild effect on U251 cell viability in their microfluidic system. They explained this resistance as a consequence of reduced GBM cell proliferation in 3D hydrogel that affects TMZ activity, which is dependent on DNA replication[195]. Pang and collaborators observed that biomechanical properties of GBM cells significantly affected sensitivity to vincristine in their microfluidic platform for single-cell separation based on cell[228]. They revealed that smaller and/or more deformable tumor cells were more resistant to the drug.

Table 1.3 Studies showing drug resistance in 3D compared to 2D cell cultures

3D cell cultures	GBM cell types	Drugs	Relative resistance (3D vs 2D)	Reference
3D culture with chitosan-hyaluronic acid scaffolds	U-118	DOX, TMZ	no difference for DOX, 2-fold for TMZ	236
3D bioprinted cell culture with gelatin/alginate/ fibrinogen hydrogel	U87, SU3 patient-derived cell line	TMZ	1.5-fold for SU3 cells, 2.2-fold for U87	175
3D culture with collagen scaffolds	U87, primary GBM cells	TMZ, CCNU, Cisplatin	U87 cells: 3-fold for DDP, 42-fold for CCNU, 6-fold for TMZ primary cells: 3-fold for DDP, 18-fold for CCNU, 6-fold for TMZ	237
3D culture with chitosan-hyaluronic acid scaffolds	Primary GBM cells	TMZ, BCNU, CCNU, Everolimus	3-fold for TMZ, 9-fold for BCNU, 16-fold for CCNU, no difference for Everolimus	165

3D bioprinted culture with gelatin/alginate/ fibrinogen hydrogel	U118	TMZ	2.5-fold	264
3D aggregates on agarose hydrogels	BMG-1	Cisplatin, Bleomycin	1.3-fold for cisplatin, no difference for bleomycin	277
Spheroids and 3D culture with gelatin foam	Patient-derived cells	Irinotecan, 5-Fluorouracil	about 10-fold for both drugs	242
3D bioprinted culture with alginate/HA/collagen I	U87, primary cell line	TMZ, cisplatin	2-fold for TMZ, 8-fold for cisplatin for U87, 24-fold for cisplatin for primary cells	177

TMZ-temozolomide; DOX-doxorubicin; CCNU-comustine; BCNU-carmustine.

According to data of Wang et al., several groups of genes demonstrated increased expression in 3D cell cultures, contributing to a higher degree of drug resistance[233]. These included genes associated with drug detoxification, drug efflux (ABCC5, ABCC3, and MVP), resistance to apoptosis (ESR1, RARG, ERBB4, MET), antiapoptotic genes (BCL2, B2M), resistance against oxidative stress (NFKB family members, PPAR, SOD1, HIF1A), DNA repair (MGMT, XPC, TOP2B and BRCA2) and DNA replication arrest (CDKN13 and CCND1). Interestingly, the authors did not observe a significant difference between 3D scaffold and 2D cultures in the expression of genes mainly involved in multidrug resistance (e.g., ABCB1) and detoxification (e.g., CYP3A4). In line with these findings are results published by Lv and colleagues that observed upregulated expression of MGMT, as a possible mechanism of resistance to alkylating agents in 3D environment, but no changes in the expression of major ABC transporters (ABCB1, ABCC1, ABCC2, ABCC4, and ABCG2)[237]. However, some authors have reported increased expression of ABCG2 in GBM cell lines resistant to drug treatment in 3D cultures[212,236]. Florczyk et al., also observed that cell line with the highest degree of resistance to alkylating agents in 3D systems, besides upregulating ABCG2 expression, also increased the expression of ABCB1[236]. Moreover, results from previously described 3D system, Cancer Drug Resistance Accelerator chip, showed that increased drug efflux activity was the main cause of emerging DOX resistance in U87 cells[197]. The authors of this study isolated resistant U87 cells from the chip and performed exome and transcriptome sequencing and identified several mutated genes (*CHD1* and *FLNA*) related to DOX resistance, as well as significant number of differentially expressed genes associated with immune response, DOX metabolism and NFκB signaling. Increased resistance to apoptosis is another mechanism that contributes to resistance to alkylating agents[206,233], as well as DOX and resveratrol[278], in 3D cell cultures. Regarding the latter study, authors observed increased production of anti-apoptotic factors, survivin and Bcl2, in 3D cultures in response to DOX and resveratrol as known apoptosis inducers.

Drug resistance in 3D models may be at least partially reversed by combined drug application. Fernandez-Fuente and collaborators showed that sunitinib resistance in three-dimensional GSC culture may be reversed through the inhibition of the Akt and ERK signaling pathways, using PD98059 and LY294002, respectively[240]. Shojaei et al., described that simvastatin, a mevalonate biosynthesis inhibitor, can increase TMZ-induced apoptosis by inhibiting autophagy flux[224]. Similarly, in our recent study we were able to sensitize TMZ- resistant RC6 cells by combining TMZ with coenzyme Q10 in 3D microfludic device within collagen hydrogel[279].

1.7 Effects of 3D culture microenvironment on GBM cell response to drug treatment

The effects of drug treatments on 3D glioblastoma culture are determined not only by culture dimensionality but also by the presence of various microenvironment factors, as summarized in Table 1.4.

Two publications reported that the efficacy of EGFR-targeted therapies in 3D GBM culture depends not only on EGFR status but also on the chemical composition and physicomechanical properties of the ECM. Pedron et al., showed that EGFR mutated, patient-derived GBM cells, that are sensitive to erlotinib, had decreased response to this TKI inhibitor in the HA-containing GelMA hydrogel, due to crosstalk between CD44 and EGFR signaling pathways[280]. Xiao and colleagues made a similar observation in their 3D brain-biomimetic platform. They confirmed that patient-derived GBM cells are less responsive to erlotinib and lapatinib in the presence of HA-bound hydrogels and this effect was also dependent on the stiffness of the hydrogel[281]. Recently, the same group showed that HA and RGD-functionalized proteins in 3D hydrogel concomitantly contributed to GBM cell resistance to the alkylating agents TMZ and carmustin[282]. This effect was mediated by Src signaling upon joint activation of CD44 and integrin. Another ECM component, fibronectin, was also shown to influence GBM cell response to targeted therapy. Efficiency of MEK inhibitor, PD0325901, on GBM cell growth, motility and dispersal from spheroid is dependent on high fibronectin concentration in the ECM[283]. Recently, two additional research groups demonstrated that growing cells in stiffer scaffolds leads to higher TMZ resistance[249,250].

As previously mentioned, hypoxic conditions promote an invasive phenotype of GBM upon 3D cultures, however the lack of oxygen also influences their response to therapy. Namely, Musah-Eroje and Watson showed that growing GBM cells in 3D culture increased resistance to TMZ which became even more pronounced under hypoxic conditions[153].

The presence of stromal cells in composite 3D GBM cultures further contributes to tumor cells' drug resistance. Namely, astrocytes and endothelial precursor cells are able to diminish the cytotoxic effect of the STAT3 inhibitor (SH-4-54) in 3D culture of stem-like GBM cell line[271]. Earlier work of Yang and colleagues also showed that addition of the astrocytic cell line to different GBM cell spheroid cultures protected them from cytotoxic insult of TMZ and DOX[284]. Additionally, Civita et al., reported that lower response to TMZ, vincristine and clomipramine can be a result of mitochondrial exchange between reactive astrocytes and GBM cells through tunneling nanotubes formed between them[268]. Xiao et al., established U87 cells co-culture with rat neurons and glial cells within 3D graphene–carbon nanotube matrix and evaluated the effect of myosin II inhibitor, blebbistatin, on tumor cell migration. They observed that the presence of cortical cells reduced blebbistatin activity reflected in decreased U87 cell motility[285].

Table 1.4 Effects of various microenvironment conditions on drug response in 3D glioblastoma cell cultures

3D cell cultures	GBM cell types	Drugs	Microenvironment conditions	Major findings	Reference
3D culture with HA decorated GelMA hydrogels	Patient-derived xenograft cells	Erlotinib	0, 0.3, 0.5, 0.7, 1 and 2 wt% hyaluronic acid methacrylate	EGFR mutated cells were 2 fold resistant in the presence of HA in hydrogel	280
Gliomaspheres and 3D culture with HA and RGD containing hydrogels	Primary cell lines	Erlotinib, Lapatinib	0.5% or 0.1% (w/v) HA, with or without RGD peptide, 1 or 2 kPa compressive modulus	Cells cultured in 3D hydrogels with a high HA content (0.5% w/v), RGD tripeptide and low compressive modulus (1 kPa) were the most resistant to erlotinib	281
Gliomaspheres and 3D culture with HA and RGD containing hydrogels	Primary cell lines	TMZ, carmustine	0.5% and 0.1% (w/v) HA, with or without RGD peptide	High content HA scaffolds, particularly those with RGD peptide, were more resistant to TMZ and carmustin than low-HA hydrogel culture and gliomaspheres	282
Spheroids	Primary cell lines	PD0325901	30 and 300 µg/ml serum fibronectin	PD0325901 increased spheroid stiffness and viscosity under high fibronectin serum concentration	283
Neurospheres	U251, U87 SNB19	TMZ	Normoxia (20% oxygen), hypoxia (1% oxygen)	U87 and U251 neurospheres were more resistant to TMZ than monolayer culture, particularly under hypoxic conditions	153
3D culture in collagen type I-hyaluronan matrix	Primary cell lines	SH-4-54	Tri-culture with normal primary astrocytes and ECFCs	Stem marker positive cells were 1.25 fold more resistant to STST3 inhibitor in 3D matrix with stromal cells than in 3D matrix only	271
Spheroids	A172, U251, LN18, C6, primary cell lines	TMZ, DOX	Co-culture with TNC-1 astrocytes	Most cell lines were resistant to TMZ and DOX in the presence of astrocytes	284

3D culture in GCNT matrix	U87	blebbistatin	Co-culture with rat neurons and glial cells	Cortical cells reduced U87 migration velocity by 34% in GCNT matrix	285
3D culture in HA-gelatin hydrogel	Primary cell line	TMZ, CLM, VCR	Co-culture with microglia	Cells were more resistant to all drugs in co-culture with microglia	275
3D culture in HA-gelatin hydrogel	Primary cell lines	TMZ, CLM, VCR	Co-culture with astrocytes	Cells were more resistant to all drugs in presence of astrocytes	268
3D bioprinted culture with GelMA and GMHA	Xenografted tumor cells	TMZ, Erotinib, Gefitinib	Tetra-culture with astrocytes, neural precursor cells and macrophages	The resistance was enhanced in tri-culture and it was potentiated with addition of macrophages	181

HA-hyaluronic acid; GelMA-methacrylamide-functionalized gelatin; RGD-arginine-glycine-aspartate; TMZ-temozolomide; ECFCs-endothelial colony forming cells; PD0325901-MEK inhibitor; SH-4-54-STAT3 inhibitor; blebbistatin-myosin II inhibitor; GCNT-graphene–carbon nanotube, GMHA-glycidyl methacrylate-HA.

1.8 Conclusions

In the past decade researchers have made a great effort to develop a variety of 3D glioblastoma cell models. These models are valuable tools for in vitro studies of glioblastoma pathogenesis and also represent good platforms for drug screenings. 3D glioblastoma models are physiologically more relevant and reliable than conventional 2D cell cultures and they are increasingly replacing monolayer cultures in laboratory practice. They should ultimately substitute animal models in preclinical drug characterization, reduce the costs of drug discovery and development, avoiding at the same time ethical concerns regarding in vivo experiments. However, there are still important issues to be considered and properties to be improved in order to fully adopt 3D glioblastoma cell culture models as standard platforms for preclinical drug screening and development. The greatest challenge in developing 3D glioblastoma models is to mimic the full temporal and spatial complexity of the tumor: organization of its structures, heterogeneity of cell types, specificity of ECM composition, dynamics of TME conditions, and simulation of different cancer-related processes, such as metastasis.

As reviewed above, spheroids represent the first step in making more complex cell cultures. They have cell-cell and cell-ECM interactions and established biochemical gradient, but are still lacking the 3D architecture of the tumor. On the other hand, organoids, as miniature organs, appear to most closely resemble native tumor structure in vitro but lack reproducibility and have limitations in continuously providing tumor-related physicochemical conditions and preserving long-term culture. Introducing 3D bioprinting technology also gives an opportunity to achieve structural complexity of tumor tissue in a controlled manner. However, bioprinted cultures, as with organoids, lack an important physicomechanical component namely fluid flow. Therefore, in the future, organoids and bioprinted cultures should be combined with other approaches and platforms that provide a dynamic microenvironment, for example perfusion bioreactors and microfluidic devices, for establishing a complete mimic of 3D glioblastoma cell culture. In this regard, microfluidic devices are so far the most comprehensive of all 3D cell culture models. Yet, there are several challenges to be addressed in the future development and use of microfluidic-based 3D glioblastoma cell cultures. In the first place, the choice of biomaterials remains a great challenge and requires further development by biomaterial and tissue engineering. Focus should be put on improving biomaterial characteristics for 3D GBM cell culture scaffolds, on increasing their long-term stability, mimicking the specific composition of GBM ECM (e.g. enriched in HA), maintaining consistency of their composition and physicomechanical properties, particularly in response to the presence of GBM cells and their dynamic interaction with scaffold. Particular attention should be paid to the choice of biomaterials- regarding the type of drugs applied in studies to avoid false positive or false negative results on chemosensitivity due to variable drug permeability and absorption. Other challenges, which also affect drug efficiency in GBM, remain to be addressed in the future design of microfluidic-based 3D GBM platforms. Those include establishing heterogeneity of GBM cells, mimicking interactions between GBM cells and other brain cell types, as well as modeling GBM motility.

2 Objectives

As stipulated in the literature review above, the microenvironment is a fundamental factor modulating the tumor progression and its response to treatment. This is why we contemplated the development of 3D in vitro models that could mimic closer the important characteristics of TME and provide more reliable models for therapy testing. However, interactions between different components of TME are still incompletely known and the heterogeneity of GBM is extensive, so more precise and detailed studies of patient tissues are needed, which is why we considered studying the microenvironment with spatial transcriptomics technique.

This thesis was financed by an i-PFIS grant for doctorates between Institutes for Health Research and companies, in this case IIS Aragon and Beonchip S.L., which permitted the development of a part of the thesis in an industrial environment.

Objectives of this thesis were:

- To collaborate on the improvement of a microfluidic device that will simulate better GBM characteristics
- To examine the role of oxygen in GBM progression and response to treatment within a microfluidic device
- To establish the model of TMZ chemoresistance development and test alternative treatment schemes
- To study the spatial expression of genes related to treatment resistance by using spatial transcriptomics.

3 Materials and methods

3.1 Patient samples

After written informed consent, tissue samples from patients with astrocytoma were collected from the University Clinical Hospital “Lozano Blesa” by the Biobank of the Aragon Health System. The histological grade was established by histopathological analysis of the surgical specimens. The use of the samples was approved by Research Ethics Committee of the Autonomous Community of Aragon (Comité de Ética de la Investigación de la Comunidad Autónoma de Aragón, CEICA), request form SA20-35. Within the scope of this thesis, fresh and fresh frozen samples and OCT blocks were used.

3.2 Primary cell lines

Tissue samples were collected during surgery, placed in ice-cold PBS, and processed within two hours after the surgery. First, the tissue was minced with a surgical blade in a glass Petri dish in sterile conditions. Accumax solution (1-2 mL) was then added to the tissue and incubated for 15 min at room temperature for chemical dissociation. Dissociated tissue was then centrifuged and resuspended in DMEM/F12 medium (Biowest, L0091), supplemented with 10% FBS (Sigma Aldrich, F7524), 2 mM L-glutamine (Lonza, 17-605C), penicillin/streptomycin (Lonza, 17-602E), and 25 µg/mL amphotericin B solution (Gibco, 15290-026). The medium was additionally supplemented with growth factors: 20 µL/mL B-27 (Thermo Fisher Scientific, 12587010), 40 ng/mL epidermal growth factor (Biotechne, 236-EG-200), and 20 ng/mL basic fibroblast growth factor (Miltenyi, 130-093-838). Dissociated tissue was monitored for 48h to confirm cell attachment before changing the medium. Cell culture was maintained at 37ºC in humidified 5% CO2 atmosphere. A low passage number was used to ensure the similarity with the patient tissue, without genetic and epigenetic changes.[286]

3.3 Commercial cell lines

Glioblastoma cell lines, U-251 MG (U251) and U-87 MG (U87), were purchased from Sigma Aldrich (09063001 and 89081402, respectively).

Human colon carcinoma cell line (HCT-116) was purchased from the American Type Culture Collection (ATCC).

All cell lines were cultured in high glucose Dulbecco’s modified Eagle’s medium (DMEM; Lonza BE12-614F), supplemented with 10% fetal bovine serum (FBS; Sigma Aldrich F7524), 2 mM L-glutamine (Lonza, 17-605C), and penicillin/streptomycin (Lonza

17-602E). Cell cultures were maintained at 37ºC within a humidified TEB-1000 incubator (EBERS Medical Technology) with 5% CO_2. Cells were subcultured when they reached 80-90% confluence using Trypsin/EDTA solution (Lonza, BE17-161E).

3.4 Fluorescent cell labeling

U251 cell line was stably transduced with a green fluorescent protein (GFP)-expressing lentiviral vector, kindly provided by Dr. Prats, University Paul Sabatier, Toulouse, France[287]. Briefly, 5 x 10^4 cells/well were seeded in 24-well plates and incubated for 24 hours at 37°C in a humidified atmosphere containing 5% CO2. The growth medium was then removed, and cells were washed twice with PBS (Lonza, BE17-516F). Opti-MEM medium (Thermo, 31985062) was supplemented with 5 µg/ml protamine sulfate (Sigma, P4505) and was mixed with the lentivirus suspension in a 1:1 ratio. This mixture was added to the cells and incubated for 24 hours. Afterward, the transduction medium was replaced with a growth medium and the cells were routinely cultured for two weeks to remove the viral particles. Transfection efficiency was checked by fluorescence microscopy with more than 90% of the cells found to be GFP-positive (U251-GFP).

Following the same protocol, U87 cell line was transduced with cherry protein (U87-cherry).

U251 cell line was transfected with a hypoxia-responsive 5HRE/GFP plasmid, which was a gift from Martin Brown & Thomas Foster (Addgene plasmid #46926; http://n2t.net/addgene:46926; RRID: Addgene_46926)[288]. Transfection was performed using Xfect Transfection Reagent (Takara, 631317). In short, U251 cells were seeded in a 6-well plate and incubated for 24 hours at 37°C in a humidified incubator containing 5% CO2. Plasmid DNA (5 µg) was diluted in Xfect Reaction buffer and mixed with Xfect Polymer. After 10 min incubation which allowed the formation of nanoparticle complexes, the solution was added to the cell culture and incubated for 4h. After 48h, the selection of transfected clones was started with 200 µg/mL G-418 (VWR, 345812-10).

U87 cells were green fluorescently labeled by adding 5 µl of lipophilic cell membrane dye Vybrant™ DiO (Invitrogen, V22886) per 10^6 cells/ml suspension. Cells were incubated for 15 min, centrifuged, and washed three times with growth media.

3.6 Spheroid formation

Spheroids were made by hanging drop and non-adherent surface methods.

For the hanging drop method, cells were trypsinized and resuspended in a growth medium supplemented with 20% methylcellulose solution to reach the concentration of 40 000 cells/mL. To form 1000-cell spheroids, 25 µL drops were placed on the lid of a Petri dish. The bottom part of the dish was filled with distilled water to prevent evaporation. Plates were placed within the incubator and left for 48h to assure spheroid formation. Afterward, spheroids were transferred to a growth medium in suspension 96 well plates (Sarstedt 83.3925.500) treated with anti-adherence solution (Stemcell 07010).

The non-adherent surface method consisted in trypsinizing the cells, preparing the concentration of 10^4 cells/mL in the growth medium, and seeding 100µL (1000 cells) per well in anti-adherence treated well plates. Further centrifugation at 1000 rpm for 5 min helped cell aggregation. Plates were then placed within the incubator and left for 48h for spheroid formation.

For spheroid maintenance, the growth medium was changed every third day.

3.7 Microfluidic device

3.7.1 Chip fabrication

Microfluidic devices consist of a central chamber and two lateral microchannels, interconnected with parallelogram-shaped pillars. The part of the device that marks the structure was fabricated by injection molding of COP. It was attached to a thin COP layer with pressure-based adhesive. To study the effect of oxygen concentration on the culture, a PDMS layer was used instead of a COP layer. PDMS was mixed with a curing agent (10:1, w/w), and 1.5 mg were placed on the 100-mm Petri dish to create the 0.2-0.3-mm layers. After 2h of curing at 60°C, PDMS layers were ready for use. To assure medium refresh below the device and constant oxygen supply, the devices were attached to a Petri dish using 3mm-high PDMS.

3.7.2 Surface treatments

Microfluidic devices were treated with oxygen plasma on Diener electronic Plasma-Surface-Technology (Atto) at 100W for 1 min, using a pressure of 0.4 mbar and 50% O_2, to increase the hydrophilicity of the material.

Where additional surface treatment was needed to strengthen the unions between the device and ECM proteins, as in PDMS devices or when using contractile cell lines, poly(ethyleneimine) (PEI) or poly(acrylic acid) (PAA) were used.

PEI treatment was performed after plasma surface activation by 10-minute incubation of the devices with 2% PEI aqueous solution, followed by 30-minute incubation with 0.4% glutaraldehyde (GA). After the solution aspiration, the devices were washed three times with distilled water and sterilized by UV exposure for 30 minutes[289].

3.7.3 Collagen hydrogel preparation and 3D cell culture within the device

Hydrogel mixture for 3D culture was composed of 50% (v/v) of the desired cell density in growth media and 50% (v/v) collagen matrix. For collagen matrix, either 3.36 mg/ml (Corning 354236) or 10.57 mg/ml (Corning 354249) type I rat tail collagen, NaOH 1N (Sigma 655104) at proportion of 1:40 (v/v of collagen volume) and DMEM 5X (Sigma D5523) at 1:5 (v/v of collagen matrix volume) were mixed to get a desired final collagen concentration (1.2 mg/mL, 2 mg/mL or 4mg/mL). Sterile water was added to reach the final collagen matrix volume. The collagen gel matrix was homogenized and kept on ice. The cell suspension at the desired cell density was homogenized with the collagen matrix and injected into the central chamber of the device. To assure 3D cellular distribution, the devices were placed up and down for a few minutes and then put within the incubator with 5% CO_2 at 37°C for 15 minutes to promote collagen polymerization. Afterward, the pre-warmed growth medium was added to the lateral channels and refreshed every day.

3.7.4 Cell recovery from collagen hydrogel

Collagenase P (Roche, 11213857001, 2.3 IU/mg) was dissolved in PBS to a final concentration of 8 mg/ml (18 IU). Collagenase solution was subsequently sterile-filtered, and 50 μl of the collagenase solution were pipetted through each lateral channel of the microdevice. Collagenase incubation was performed at room temperature for 10 min. Afterward, the recovered cell suspension was transferred to a fresh Eppendorf tube and washed with PBS before subsequent steps.

3.7.5 Hypoxia studies

To study oxygen concentration and functional effects of hypoxia within the device, two approaches were used.

ImageIT Red Hypoxia reagent (Thermo Fisher, H10498) was added to a hydrogel mixture and a growth medium at a concentration of 10 uM. This compound is fluorescent starting from 5% oxygen and the lower the concentration of oxygen, the higher the fluorescence intensity.

For studying the functional effects of hypoxia, U251 cells transfected with a 5-HRE/GFP plasmid, as explained above, were used. Hypoxia response elements (HRE) are activated by hypoxia-inducible factor (HIF), the main transcription factor in hypoxia.

The cells were embedded in collagen hydrogel and seeded within COP and PDMS device at the concentration of 40 x 10^6 cells/mL.

3.8 TMZ treatment

TMZ (Sigma, T2577) was reconstituted in DMSO to 50 mM concentration. The final concentration used in our experiments was 100 µM, as that is the maximum concentration measured in the patient's plasma[291]. For most of the experiments, a clinical treatment scheme was used. It contains a 5-day TMZ treatment, followed by a 23-day rest[6]. Alternative approaches studied included treatment once in 28 days, once a week, or every four days. DMSO was used as a control.

3.10 CCK-8 viability assay

Cell Counting Kit – 8 (CCK-8, Dojindo, CK04) was used for the initial validation of TMZ effectivity in different in vitro models. Different cell concentrations were seeded in each culture to enable long term experiments (1 000 cell/mL for 2D culture, 25 000 cells/mL for 3D gel culture, and 10 000 cells/mL for 3D spheroid culture). 10% CCK-8 solution was added to the medium on days 0, 5, and 21 and incubated for three hours. The absorbtion rate was measured at 450 nm using Biotek® SynergyTM HT multi-reader (BioTek Instruments, Inc. VT, USA).

3.11 Viability staining

The viability of cell culture was determined by calcein-AM/propidium iodide (CAM/PI) staining. Stock solutions of 1mg/ml CAM (Life Technologies, C1430) and 2mg/ml PI (Sigma, P4170) were dissolved in DMSO and distilled water. To test cell viability, CAM and PI stock solutions were diluted to 2 and 6 μg/ml, respectively, in phosphate-buffered saline (PBS) (Lonza BE17-516F). CAM/PI solution was added to a 96 well plate with spheroids or perfused through the lateral channels of microfluidic devices and incubated for 15 min. CAM becomes fluorescent once it reaches the cytoplasm of viable cells and PI stains dead cells, with compromised cell membrane.

For cell death tracking, two drops of NucGreen Dead 488 ReadyProbes Reagent (ThermoFisher, R37109) were added to a 1 mL growth medium and perfused through lateral channels.

3.12 Histological and immunohistochemical analysis

Spheroids were fixed with 4% paraformaldehyde (PFA) for 15-30 min at room temperature. To facilitate handling, they were stained with blue tissue-marking dye (Labolan, 240101K) before paraffin embedding. Sections (3 µm thick) were used for hematoxylin-eosin (H&E) staining and for immunohistochemical detection of Ki67 (FLEX Monoclonal Mouse Anti-Human Ki-67 Antigen, Clon MIB-1, Ready-to-Use (Dako Omnis, GA626)), which were automatically done using Dako Omnis instrument (GI10230) at the Pathology service of the University Hospital “Miguel Servet”.

3.14 Immunofluorescence staining

Hydrogels in microfluidic devices were fixed with 4% PFA for 15-30 min at room temperature. COP/PDMS layer was detached, and hydrogels were transferred to a microscope slide. They were washed three times with 0.05% Tween20/PBS for 15 min each and then permeabilized with 0.1% TritonX-100/PBS for 15min. After blocking with 5% BSA/PBS with 3% goat serum for 4h at room temperature, primary anti-caspase 3 antibody produced in rabbit (Sigma Aldrich, C8487) was diluted in 2.5% BSA/ 0.05% Tx100 (1:1000) and incubated overnight at 4°C. After washing three times, a secondary goat anti-rabbit IgG-Rhodamine antibody in 2.5% BSA/ 0.05% Tx100 (1:200) was added and left overnight at 4°C. Finally, nuclei were stained with Hoechst 33342 for 3h, washed, and mounted with Mowiol medium.

3.15 Amnis imaging cytometry

The determination of cell mortality and its classification between early, late apoptosis, necrosis, and necroptosis was carried out in the Service of Cytomics of the University of Zaragoza with Image Cytometer "ImageStream X" (AMNIS, Seattle, WA) as previously described in the literature for the determination of cell viability along with cell death studies[292,293]. Cells grown in the microdevices for 24 and 72 h were extracted from the devices with the collagenase technique described above. After one PBS wash and centrifugation, cells were resuspended in PBS and stained with “FITC Annexin V apoptosis detection Kit with Propidium Iodide” (Biolegend, 640914) according to the manufacturer’s instructions. The staining kit was validated with HCT-116 cultured in 2D for 24 and 72h as an internal control.

For cell analysis, the 488 nm laser was used. The capture of the fluorescence of 480-560 nm was used for the determination of Annexin V (AV) and the capture of 660-745 nm for the determination of propidium iodide (PI). The representation of both contents determines in the four quadrants of the bi-parametric histogram: the number of living cells without staining (PI- AV-), early apoptosis (PI- AV+), dead due to necrosis or necrotic (PI+ AV-). The population with double staining (PI+ and AV+) underwent an additional determination of nucleus morphology. For nucleus morphology, we used both the area occupied by the nucleus and bright detail intensity to discriminate necroptotic cells (intact nucleus with homogeneous staining) from late apoptotic cells (fragmented and inhomogeneous nucleus).

3.16 Imaging and analysis

Bright field, fluorescence, and confocal images were acquired using a Nikon Eclipse Ti-E C1 confocal microscope, while color images were acquired on a Leica DMi-8 microscope.

Images were analyzed using Fiji software (http://fiji.sc/Fiji).

Fluorescence intensity across the central microchamber of the microdevice was quantified by selecting a rectangular region across the chamber and using the plot profile function under the software instructions.

To estimate cell concentration within microfluidic devices with U251-GFP cells, the cell concentration was assumed proportional to the fluorescence intensity. The constant of proportionality was calculated assuming that the integral of the initial cell concentration along the chamber equals the total amount of cells.

Spheroid growth was analyzed with a Fiji plugin SpheroidJ, which allowed automated analysis of the spheroid area and was developed in collaboration with the University of La Rioja, using the images generated during this thesis[294].

3.17 RNA extraction

3.17.1 2D and cells embedded in collagen gels

2D HCT control samples were extracted from 12-well plates at 150 000 cells/well. Embedded cells were extracted from collagen hydrogels confined in 2 microdevices, as described in previous sections. RNA was extracted using Total RNA Purification Plus Kit (Norgen Biotek Corp, Canada).

3.17.2 Spheroids

Spheroids were collected on days 0, 28, and 56, washed in PBS, frozen in liquid nitrogen, and stored at -80°C. Before adding a lysis buffer RLT Plus, the spheroids were minced in liquid nitrogen in a cell crusher. AllPrep DNA/RNA Micro Kit (Qiagen, 80284) was used to simultaneously extract DNA, RNA and proteins, according to the manufacturer’s protocol.

3.17.3 Fresh frozen (FF) patient samples

Freshly extirpated patient samples were washed in PBS and frozen in liquid nitrogen alone or with optimal cutting temperature (OCT) compound and stored at -80°C. Ten 10 µm-sections were cut for RNA extraction and RNeasy lipid tissue mini kit (Qiagen, 74804) was used following the manufacturer’s instructions.

3.18 RNA quantification and quality control

The concentration of RNA extracted from collagen hydrogels and its purity were assessed employing absorbance measurements using a Biotek® SynergyTM HT multi-reader (BioTek Instruments, Inc. VT, USA).

RNA extracted from spheroids and patient samples was quantified using Qubit fluorometer and Qubit RNA High Sensitivity (HS) Kit (ThermoFisher, Q32852). RNA quality was assessed by calculating RNA integrity number (RIN) using Tape Station 2200 and High Sensitivity RNA ScreenTape.

3.19 Real-time PCR

cDNA was synthesized by using PrimeScript™ RT-PCR Kit (TaKaRa) according to the manufacturer's instructions. Briefly, 1 μg of RNA was taken from each sample and diluted to a final volume of 16 µl in an Eppendorf tube. 4 µl of 5x Master mix was added to a final volume of 20 µl. The mixture was incubated in a CFX96 Real-Time System (Bio-Rad, Spain) for 15 minutes at 37°C, for 5 seconds at 85°C and finally, the mix was cooled down to 4°C.

PrimeTime® qPCR assay probes were purchased from IDT® (Integrated DNA Technologies, Spain) for *RALBP1*, *MKI67*, and *SLC2A1*, as screened genes, and for *GAPDH* and *ACTB*, as housekeeping genes.

PrimeScript qPCR Kit was used to perform the qPCR reactions in a CFX96 Real-Time System according to the manufacturer's instructions to a final qPCR volume of 10 µl. The conditions for the q-PCR were the following: 95°C for 15s, [95°C for 15 seconds, 60°C for 30 seconds] (40 cycles), followed by a 4°C cooling hold step. Two endogenous genes (*GAPDH* and *ACTB*) were used for the normalization of the data. All reactions were performed in triplicate. Target gene expression was normalized using the geometric mean of the mentioned reference genes. Relative gene expression fold changes were determined between the time points of 24 and 72 h using the 2−ΔΔCt method.

3.20 RT2 profiler PCR array

The expression of 84 genes related to cancer drug resistance was studied by RT2 profiler PCR array (Qiagen, PAHS-004ZA) following the supplier instructions. RNA was extracted from FF, primary and recurrent GBM patient samples, and spheroids treated with TMZ as explained earlier. RNA (20 ng) was reverse transcribed using the RT2 PreAMP cDNA Synthesis Kit (Qiagen, 330451) with an incorporated genomic DNA (gDNA) removal step. cDNA was mixed with the RT2 SYBR Green qPCR Mastermix (Qiagen, 330500) and added to RT2 Profiler PCR Array, which also included housekeeping genes, gDNA control, reverse transcription, and positive PCR controls. qPCR was performed in a Bio-Rad CFX96 real-time cycler. *HPRT1* was used as a housekeeping gene, and data was analyzed by the Qiagen online software.

3.21 Spatial transcriptomics (Visium)

The spatial transcriptomics experiments were performed using the Visium Spatial Transcriptomics Kit (10x Genomics) according to the manufacturer's instructions. Briefly, 10-μm sections of fresh frozen tissues were placed on the Visium Spatial Gene Expression Slide, with one section per capture area. Sections were then fixed with methanol and stained with hematoxylin and eosin. Imaging was done with a Leica DMi8 microscope, obtaining a classical histological image. Afterward, 30-min permeabilization was performed to release the mRNA from the tissue and capture it onto primers on the slide. Reverse transcription was done using template switch oligos and second strand DNA was produced. After denaturation, cDNA was transferred from the slide to the Eppendorf tube for amplification and library construction. Sequencing was done on a lane of HiSeq 4000 (Illumina) flowcell. Raw FASTQ files and histology images were aligned against Human Reference Genome (GRCh38-2020-A) with the Space Ranger software, and downstream analysis was done in Seurat R package, at the Genomics Unit of Centro Nacional de Investigaciones Cardiovasculares (CNIC).

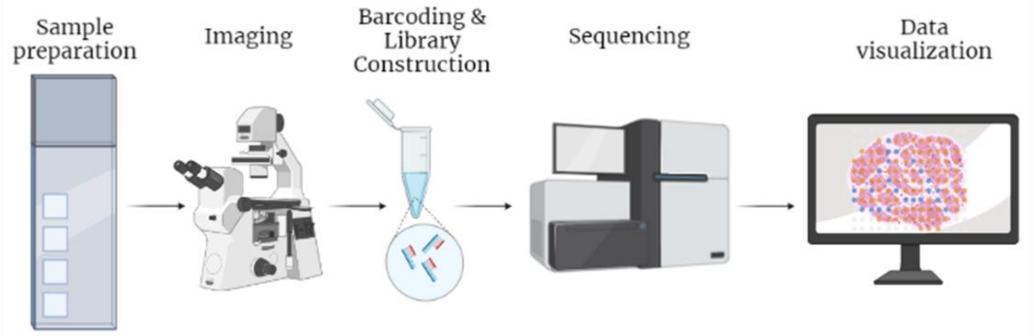

Figure 3.1 Visium Spatial Transcriptomics workflow.
Created with Biorender.

3.23 Statistical analysis

All the experiments were repeated at least three times as independent biological repeats. All results were presented as the mean ± standard deviation of the mean. Data were analyzed using GraphPad Prism, and statistical significance was set at $p < 0.05$. Normality was tested by D’Agostino-Pearson test. If the Gaussian distribution was confirmed, one-to-one comparisons were performed with a Student t-test with Welch's correction (if SD were not the same). If the normality test was not passed, a non-parametric test was performed (Mann-Whitney test). Multiple comparisons by ANOVA were corrected using the Tukey test.

4 Evolution of Be-Gradient device[2]

---

[2] This chapter contains confidential information.

5 Deciphering the role of oxygen in glioblastoma progression inside organ-on-chip models

As explained above, the configuration of our device and the material used for its fabrication allowed the spontaneous formation of oxygen and nutrient gradients and recreation of necrotic core and pseudopalisade formation in vitro[195,203]. Also, as described in 1.2, hypoxia can induce phenotypic changes that support tumor progression. It can promote stem-like properties, activate pro-survival signaling pathways, modulate cellular metabolism, regulate apoptosis and autophagy and induce migration[101,110]. However, not only oxygen gradients are present within the tumor, but also nutrient or metabolites, growth factors and waste gradients. Their interaction in the ischemic event was not well studied. Therefore, we wanted to decouple the effects of oxygen from other gradients to check if the lack of oxygen was the main trigger for GBM progression.

We fabricated a device using oxygen-permeable PDMS as a base layer for our device instead of the COP layer for this study. This device configuration allowed homogeneous oxygen distribution within the central chamber but maintained gradients of nutrients and factors present in the growth medium, as shown in Figure 5.1. To repeat the conditions used previously for the formation of the necrotic core, a high concentration (4 x 10^7 cells/mL) of U251 cells was embedded in collagen hydrogel and seeded within the central chamber of the device and the culture was followed for 5 days.

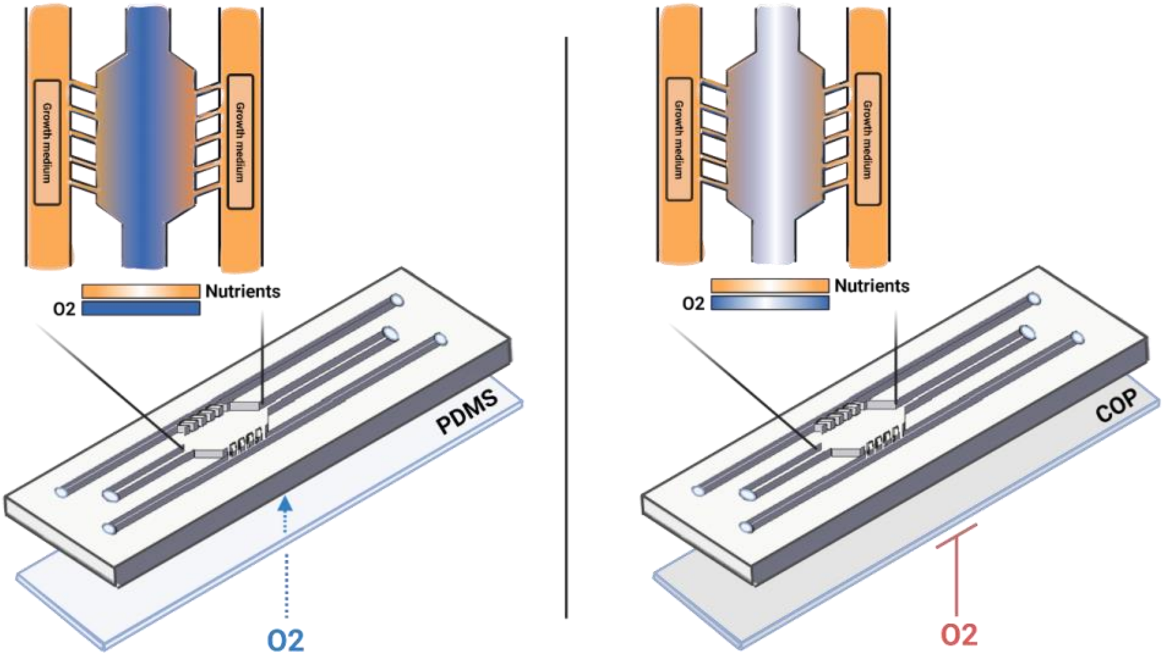

Figure 5.1 Configuration of microfluidic devices with different gas permeability.
Depending on the material used for the fabrication different gradients could be generated within the device. A. PDMS is gas-permeable material, so oxygen distribution within the camber was homogeneous, and cells were exposed to gradients of nutrients and factors. B. COP is gas-impermeable material, so cells could get oxygen through lateral channels only, and apart from nutrient gradients, oxygen gradients were also generated.

5.1 Results and discussion

5.1.1 Verification of hypoxic conditions

To corroborate the differences in oxygen levels within the devices, two methods were employed. Firstly, Hypoxia ImageIT Reagent was used to directly visualize the level of hypoxia within the device. This compound is fluorescent when the oxygen concentration is lower than 5%, and its fluorescence intensity increases with the decrease in the oxygen level. As shown by Ayuso, we confirmed that hypoxia was self-induced within the COP device, with the highest level in the center of the chamber. As expected, fluorescent intensity was significantly lower in the PDMS device, confirming that the PDMS layer was permeable to gases and did not allow the generation of hypoxia within the central chamber. The difference in the fluorescence intensity between the devices on the second day of culture is shown in Figure 5.2, with corresponding confocal images.

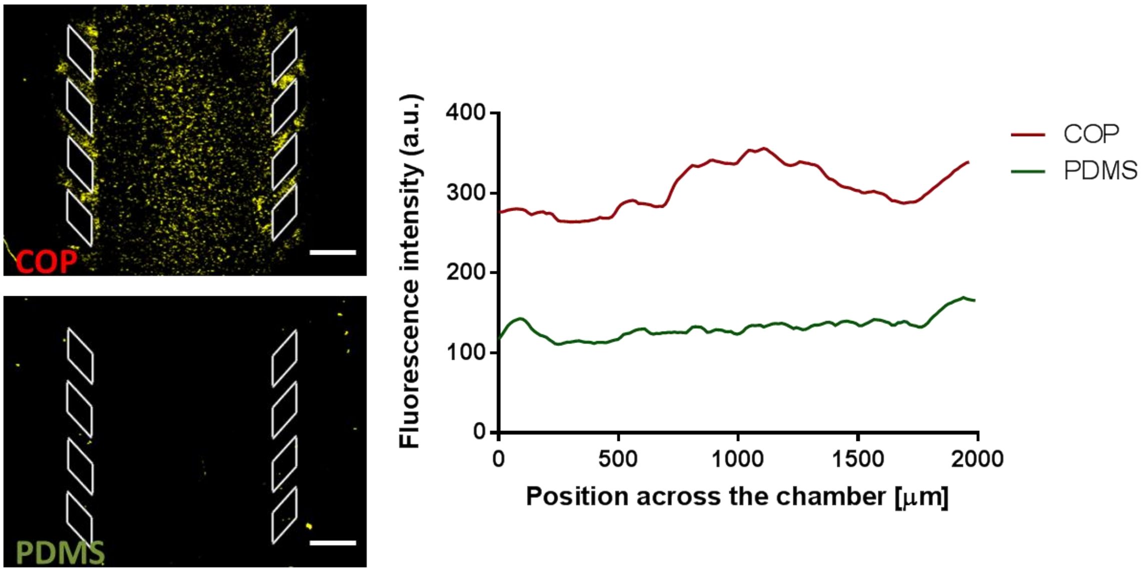

Figure 5.2 Differences in oxygen concentration within the device.
Hypoxia ImageIT reagent was added to 4 x 10^7 U251 cells/mL embedded in collagen hydrogel. This reagent is fluorescent when oxygen concentration is lower than 5%, so the fluorescence level confirmed hypoxic conditions in the COP device. Scale bar is 500 μm.

Moreover, changes in fluorescent intensity, hence level of hypoxia, monitored for a 5-day experiment, can be seen in Figure 5.3. In COP devices, we observed that fluorescence intensity increased during the first 2 days, and then it was lower on days 4 and 5. That could be the result of cell death, as fewer cells were demanding oxygen in the central chamber, so oxygen levels did not decrease as much as the first days of the experiment when most of the cells were alive. A significant change was also observed in oxygen concentration in the PDMS device ($p<0.0001$). This could be the result of the device configuration since the biggest part of the device was still gas-impermeable, and the oxygen exchange was done just from the bottom part. In any case, the fluorescence level was significantly lower than in the COP device ($p<0.0001$). Moreover, the oxygen concentration was also higher (lower fluorescence) at the end of the experiment in the PDMS device compared to the previous days, which could also be explained by the decrease of viable cells in the central chamber.

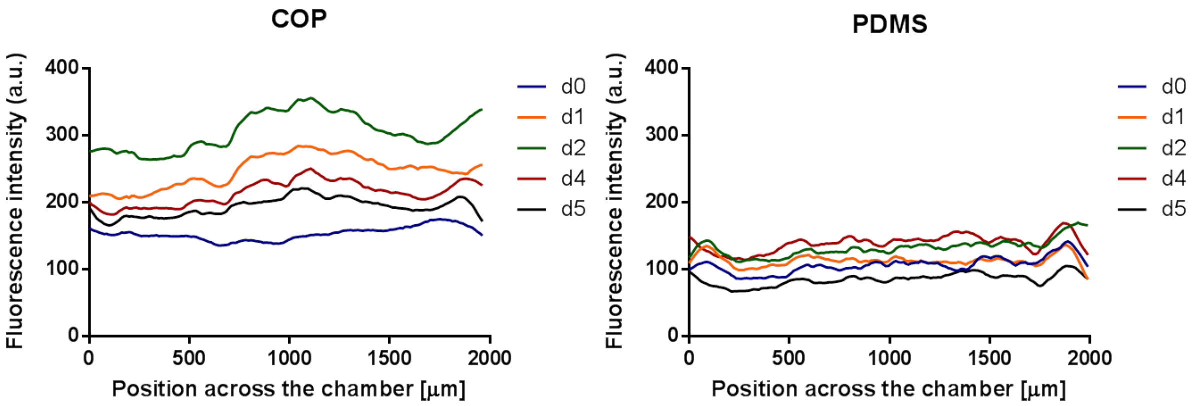

Figure 5.3 Five-day monitoring of oxygen concentration.
A. Increase in fluorescence intensity could be seen in the COP device, especially in the central part of the chamber, signifying lower oxygen concentration. B. The distribution of oxygen was homogeneous in the PDMS device, even though there was a slight increase of fluorescence intensity.

To validate if the low oxygen level had functional effects, cells were transfected with the 5HRE/GFP plasmid, so they should become fluorescent when promoters of genes that respond to hypoxia were activated. Our results, shown in Figure 5.4, demonstrated that there was almost no fluorescence within PDMS devices, while there was higher fluorescence in COP devices, again confirming different oxygen levels in the devices.

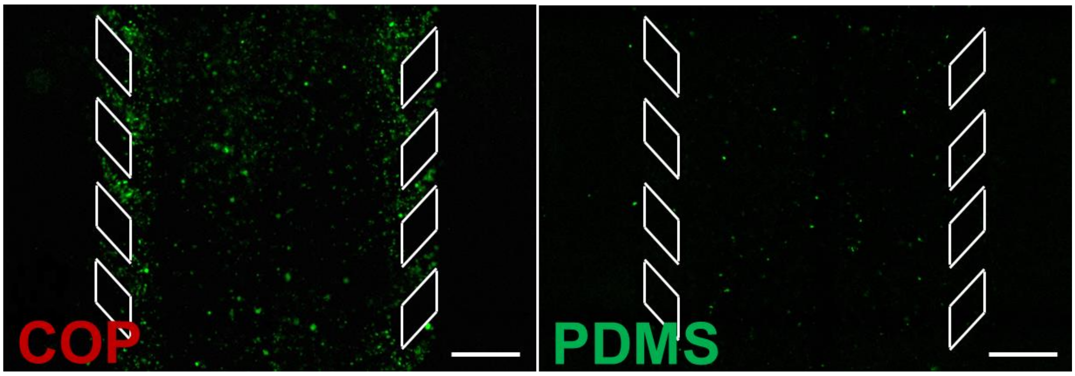

Figure 5.4 Visualization of the activation of hypoxia responsive elements (HRE).
U251-HRE cells were embedded in collagen hydrogel and seeded within the devices. When hypoxic conditions were established, fluorescent signal was liberated from the activation of genes that responded to hypoxia. Fluorescence intensity was significantly higher in COP devices compared to PDMS devices. Scale bar is 500 µm.

5.1.2 Necrotic core formation under different oxygen conditions

To validate the effect of oxygen concentration on cell death and necrotic core formation, a CAM/PI viability staining was done. It was observed that, after 5-day culture, within the COP chip a necrotic core was formed, as Ayuso showed[195], while in the PDMS chip there was a homogeneous death within the chamber, without enhanced cell death in the center of the chamber (Figure 5.5). This suggested that hypoxia was necessary for the necrotic core formation process. Moreover, apart from central death in COP device, we observed a higher level of dead cells next to the pillars. This could be the result of oxidative stress induced by ischemia-reperfusion cycles[324–326].

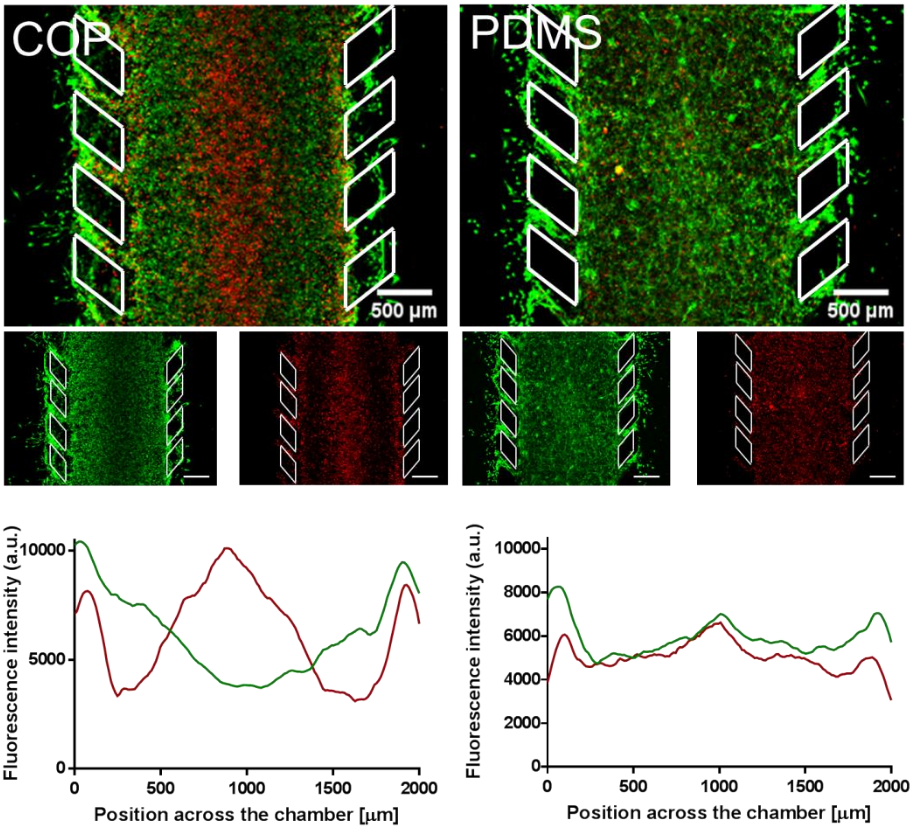

Figure 5.5 Cell death in devices with different oxygen permeability.
4 x 10^7 cells/mL were seeded within the devices and CAM/PI viability staining was done on day 5. In COP device, where oxygen gradients were present, PI stained cells in the center of the chamber, marking necrotic core. On the contrary, homogeneous death was observed in PDMS device, suggesting that hypoxia had an important role in necrotic core formation. Scale bar is 500 µm.

On the other hand, NucGreen Dead stain was added to the cultures to follow the temporal evolution of dead cells during the assay. This stain is fluorescent once bound to DNA, and it cannot cross the cell membrane, which means that it marks cells with compromised membranes, as of late apoptotic or necrotic cells. As seen in Figure 5.6, from the beginning, it was clear that the evolution of the cultures within the devices with different oxygen permeability was different. In the COP device, on the third day of culture, the initiation of the necrotic core was observed in the center of the device, which expanded and was clearly seen on day 5. Meanwhile, homogeneous staining was observed in the PDMS device, with an increase in the number of dead cells. These results supported the hypothesis that the oxygen levels were higher because of the decrease of viable cells in the last days of the experiment.

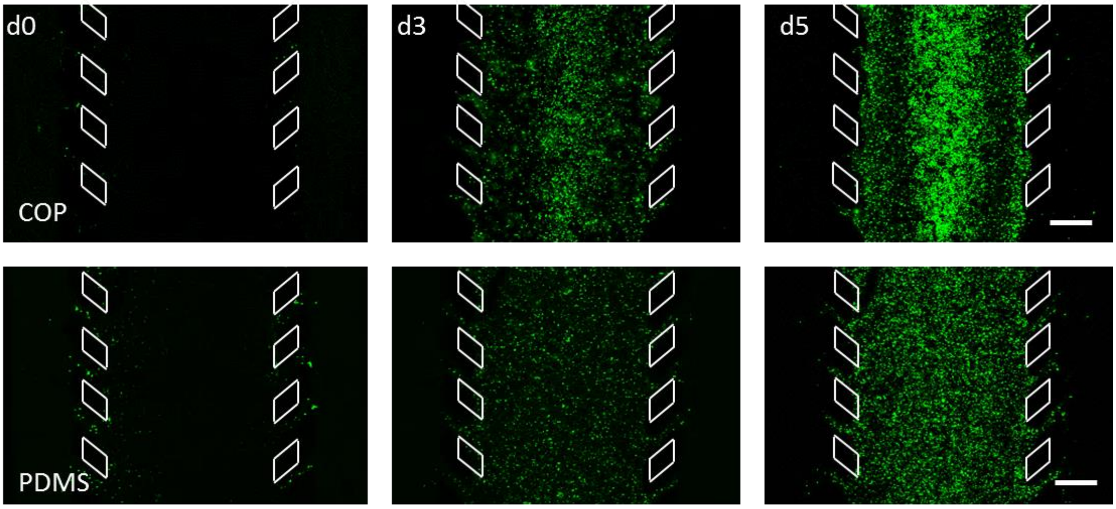

Figure 5.6 Cell death monitoring over time.
NucGreen Dead was added to 4 x 10^7 U251 cells/mL to monitor cell death during the experiment. It stained cells with disrupted cell membranes. Again, it was seen that cells primarily died in the center of the chamber in the COP device, and that homogeneous death was present in the PDMS device. Scale bar is 500 µm.

A few more groups investigated the importance of oxygen gradients for GBM progression. Hee-Gyeong et al. developed a bioprinted model of GBM that permitted the creation of gradients within the tumor. Changing the material used for the top layer (glass or silicone), they fabricated devices with different oxygen permeability. They saw that a necrotic core was only formed in hypoxic conditions[184]. Moreover, Palacio-Castañeda et al. fabricated PDMS gradient devices, similar to ours[327]. They incorporated a poly(methyl methacrylate) (PMMA) layer within the PDMS to prevent oxygen diffusion to decouple oxygen effects. Even though they saw differences in oxygen concentration, a necrotic core was not formed in either of the devices. This was probably the result of a short-term culture (2 days), but also could be affected by incomplete blockade of oxygen diffusion, as they showed that the PMMA layer slowed down the diffusion but did not block it.

5.1.3 Apoptosis activation under different oxygen conditions

To study the apoptosis activation within our devices, immunofluorescence staining was done for the active form of caspase3 on the 5th day of culture. Within the COP device apoptosis was activated only in the transition zones, between the necrotic core and the most oxygenated zone (pillars). In contrast, there was homogeneous apoptosis throughout the chamber in the PDMS device (Figure 5.7A). Furthermore, when labeling was done on patient samples (Figure 5.7B), strong immunoreactivity for cleaved caspase3 was seen in a perinecrotic region (pseudopalisade)[100,328]. Additionally, the same distribution of necrosis and apoptosis was seen in stroke and myocardial infarction[329]. Hence, the oxygen impermeable device can resemble better the physiological characteristics of the ischemic tissue.

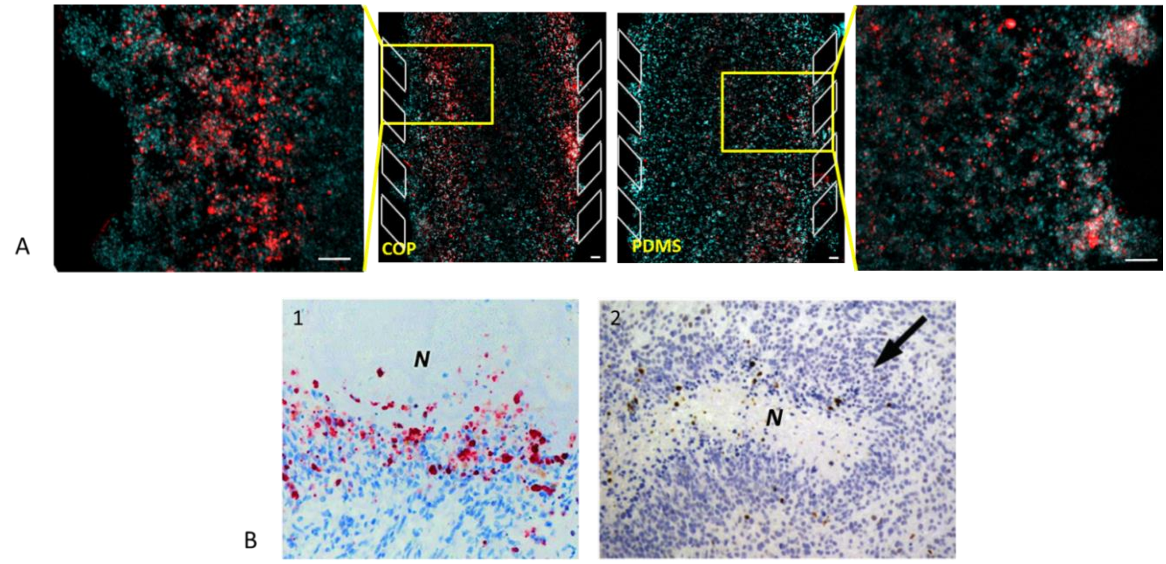

Figure 5.7 Distribution of cleaved caspase-3 in microfluidic devices and patient samples.
A. In COP devices cleaved caspase-3 positive cells were mainly found in the region between pillars and necrotic core, while in PDMS device they were uniformly distributed. Scale bar is 100 µm. B. In patient tissues, positive cells were observed in perinecrotic regions. 1 –adapted from [328] and 2 – adapted from [100].

5.1.4 Temozolomide treatment under different oxygen conditions

Referring to the previously explained importance of hypoxia in generating resistance to therapy, we wanted to study the role of oxygen in chemotherapy response to temozolomide (TMZ) within our devices. As TMZ treatment usually follows the tumor extirpation, when only invading cells remain, lower cellular concentration was used in these experiments (4 x 10^6 cells/mL). Also, lower collagen concentration (2 mg/mL instead of 4 mg/mL), given that the surrounding tissue has lower stiffness than tumor[330,331]. U251 cells were treated with 100 µM TMZ for 5 days, replicating the clinical dosing scheme. After treatment, the culture was left 5 more days to recover. It was observed that TMZ had a stronger effect in the PDMS device (p=0.0012, Figure 5.8), where oxygen concentration was higher, suggesting that hypoxia increased resistance to treatment in our model, as seen in the literature. Musah-Eroje A. and Watson S. showed that TMZ had lower effect on cells grown in 3D compared to 2D, and that was even more prominent in hypoxia[153]. Moreover, hypoxic conditions were shown to activate the expression of different miRNA, which could lead to enhanced TMZ resistance[332,333].

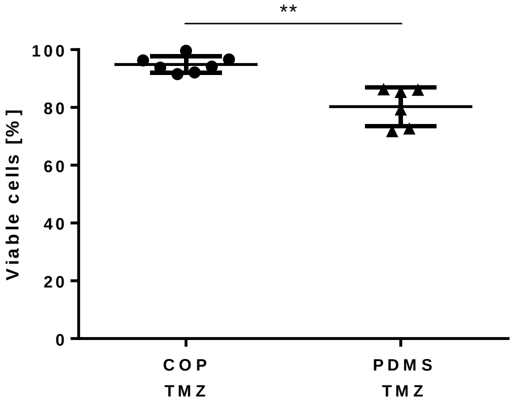

Figure 5.8 Response to TMZ treatment.
4 x 10^6 U251-GFP cells/mL were treated for 5 days with 100 µM TMZ, and left 5 more days to follow the effect of the drug. On day 10, there were significantly more viable cells in COP device compared to PDMS device (p=0.0012), suggesting that hypoxia protected cells from TMZ effect.

5.2 Conclusions

As shown earlier, we demonstrated here that our microfluidic devices allow simulating important glioblastoma behavior. By generating an oxygen-permeable device, we confirmed the importance of hypoxia in GBM progression. The development of hypoxic conditions led to the necrotic core formation, while it did not occur in normoxic conditions. Similar to the patient tissue, cells surrounding central necrosis were positive for the active form of caspase-3, marking apoptosis. Also, as expected, TMZ treatment induced more cell death in normoxic conditions, confirming that hypoxia increases resistance development. Therefore, our models mimic more physiological characteristics of GBM and could be further used to understand better GBM behavior and drug response.

6 Chemoresistance development in the 3D spheroid model

Different in vitro models were used for treatment response studies, apart from the microfluidic devices. As already explained, traditionally used 2D cell culture cannot simulate the complexity of the tissue and the natural behavior of the cells. Hence, more complex 3D systems could help us obtain more physiologically relevant results.

Standard clinical chemotherapy (Stupp protocol) consists of different cycles of a 5-day TMZ treatment followed by 23-day rest. The treatment cycle is usually repeated six times, but the treatment can be prolonged depending on the patient's evolution. The recommended dosage is 150 mg/m^2 per day, and can be increased to 200 mg/mL if there are no strong secondary effects after the first treatment cycle.[6] Here, we studied the response of GBM cells to two treatment cycles, trying to understand the reasons for low treatment efficacy and resistance development.

6.1 Results and discussion

6.1.1 Treatment efficacy in different culture conditions

First of all, we wanted to confirm the different behavior of our GBM cells in 2D and 3D models, so we compared 2D culture, 3D gel culture, simulating the cell-extracellular matrix interactions, and 3D spheroid culture, favoring cell-cell interactions.

6.1.1.1 Optimization of culture conditions

Two glioblastoma cell lines (U251 and U87) were used to simulate the heterogeneity of the tumor, as we observed their different behavior. U87 cells were more proliferative and more metabolically active than U251 cells[334]. Different cell seeding density was tested to encounter the one that allowed long-term culture without the need to trypsinize the cells (data not shown). Furthermore, as seen in Chapter 4, U87 cells have a higher contractile capacity and easily remodel the extracellular matrix. Hence, it was important to choose the seeding density that would not compromise the hydrogel consistency until the end of the experiment (data not shown).

Moreover, U251 and U87 spheroids had different behavior. For spheroid formation, seeded cells were left for two days to establish a compact, stable structure. Figure 6.1. shows the spheroid evolution after formation. We observed that U87 spheroids started growing immediately (Figure 6.1-A), while U251 spheroids decreased in size (Figure 6.1-C). The high proliferation rate of U87 cells led to a six times increase of spheroid size in 14 days (Figure 6.1-B1). Moreover, we observed that the growth of U87 spheroids depended on nutrient availability, as already shown by Panchalingam et al.[253]. If more medium was used for the spheroid maintenance (Figure 6.1-B2), or complete medium was refreshed instead of just one part (Figure 6.1-B3), the conditions were favorable for more cells, so the proliferation was higher, and spheroids were bigger.

Unlike, U251 cells seemed to form strong intercellular connections, which led to spheroid contraction and an almost 50% size decrease (Figure 6.1-D). For further experiments with U251 cells, we decided to leave the spheroids for nine days before starting the treatment, as the descent slope was highest during the first week after the 2-day formation. The data obtained was helpful for the validation of an in silico model of spheroid evolution, developed by our colleagues from the University of Seville (article under major revision in Computer Methods and Programs in Biomedicine).

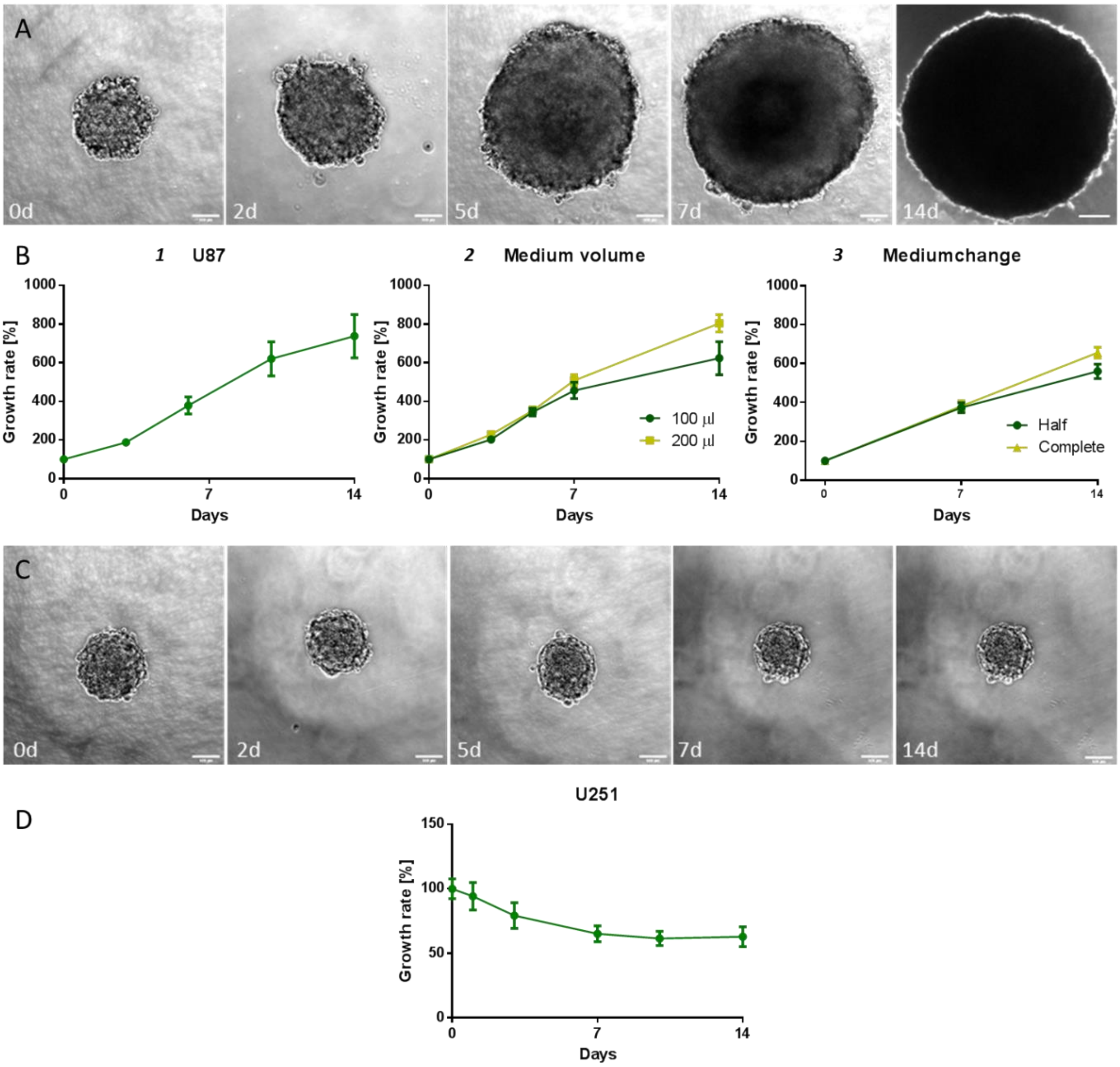

Figure 6.1 Spheroid evolution.
A. U87 spheroids were highy proliferative and increased their size significantly, which was quantified in B1. Their growth depended on the availability of nutrients, and the increase was higher if more medium was used for maintanance (B2) or refresh (B3). C. U251 spheroids continued compacting the spheroid after the initial formation and significantly decreased their size, shown in D. Scale bar is 100 µm.

6.1.1.2 Response to TMZ treatment in different in vitro models

Described cultures were treated with 100 µM TMZ for five consecutive days and then maintained in a fresh growth medium to study the TMZ efficacy. In this case, the experiment was stopped on day 21 because of the confluence of the control 2D cell culture. Therapy effectiveness is shown in Figure 6.2, where the percentage of viable cells is normalized to the corresponding control sample. As it was shown in Chapter 1 and summarized in Table 1.3, cells were more sensitive in 2D culture than in 3D culture in either of the conditions studied. Also, U251 cells were more resistant than U87 cells, probably due to their different proliferation rates, although huge heterogeneity is reported in the literature about the response of these cell lines to TMZ[335,336].

The mechanism of action of TMZ could explain the response observed. TMZ is a methylating agent affecting proliferating cells by blocking the replication fork and inducing the cell cycle arrest in a G2/M phase, leading to activation of senescence and cell death[337–339]. Therefore, as U251 cells were less proliferative than U87 cells, the efficacy of the treatment was lower and higher viability was observed. Likewise, lower proliferation in 3D cell culture (see 1.4) could lead to a lower response to TMZ treatment compared to 2D culture.

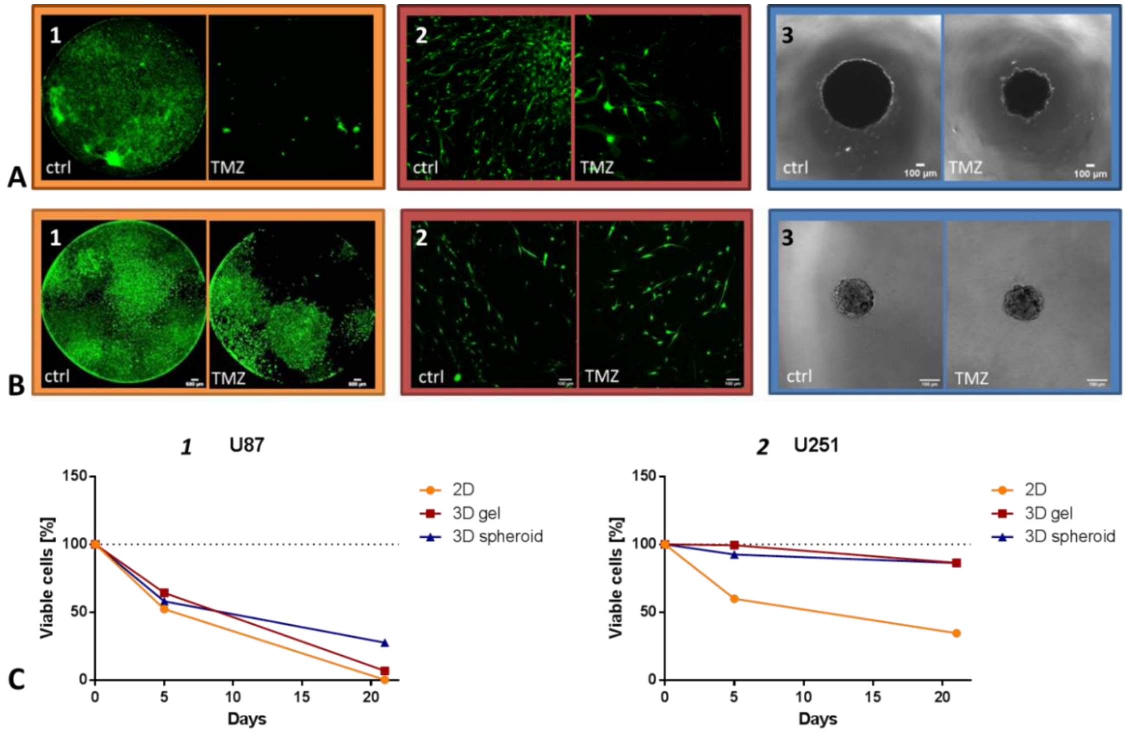

Figure 6.2 Response to TMZ in different in vitro models.
TMZ effect was studied on U87 (A) and U251 (B) cell lines, in 2D culture (1), 3D gel culture (2) and 3D spheroid culture (3) on day 21. As can be appreciated on confocal images in A and B, and quantified by CCK8 assay (C), cells in 2D were the most sensitive ones. Moreover, TMZ effect was weaker on U251 cells. Scale bars are 500 µm for A1 and B1, and 100 µm for the rest.

Further experiments were focused on spheroids, as they simulated chemical gradients present in the solid tumor and were responsible for tumor progression. Moreover, this culture can be easily maintained for long-term experiments. Although both cell lines have been previously used as GBM models, we decided to follow our experiments with U87 since U251 spheroids showed characteristics more compatible with low-grade astrocytoma tumors.

6.1.2 Treatment scheme testing

As explained earlier, classical clinical treatment consists of 5-day TMZ treatment and 23-day rest, repeated several times, depending on the patient's evolution. Different dosing schemes have been part of clinical trials to improve the TMZ efficacy, and they have been usually used to treat recurrent GBM. Some of them are a 7-day treatment in a 14-day cycle (7+7), 21-day treatment in a 28-day cycle (half TMZ dose, 21+7), and everyday treatment (28/28, ¼ - ½ dose). However, they all have demonstrated a low clinical effect on patients´ overall survival rates[340,341].

The study of the response of our spheroid culture to clinical treatment was our primary interest. However, the pilot study was conducted with some alternative dosing schemes in a search for a potential better response to TMZ. Hence, spheroids were treated just once in 28 days (x+28), once a week (x+7), and once every four days (x+4) (Figure 6.3).

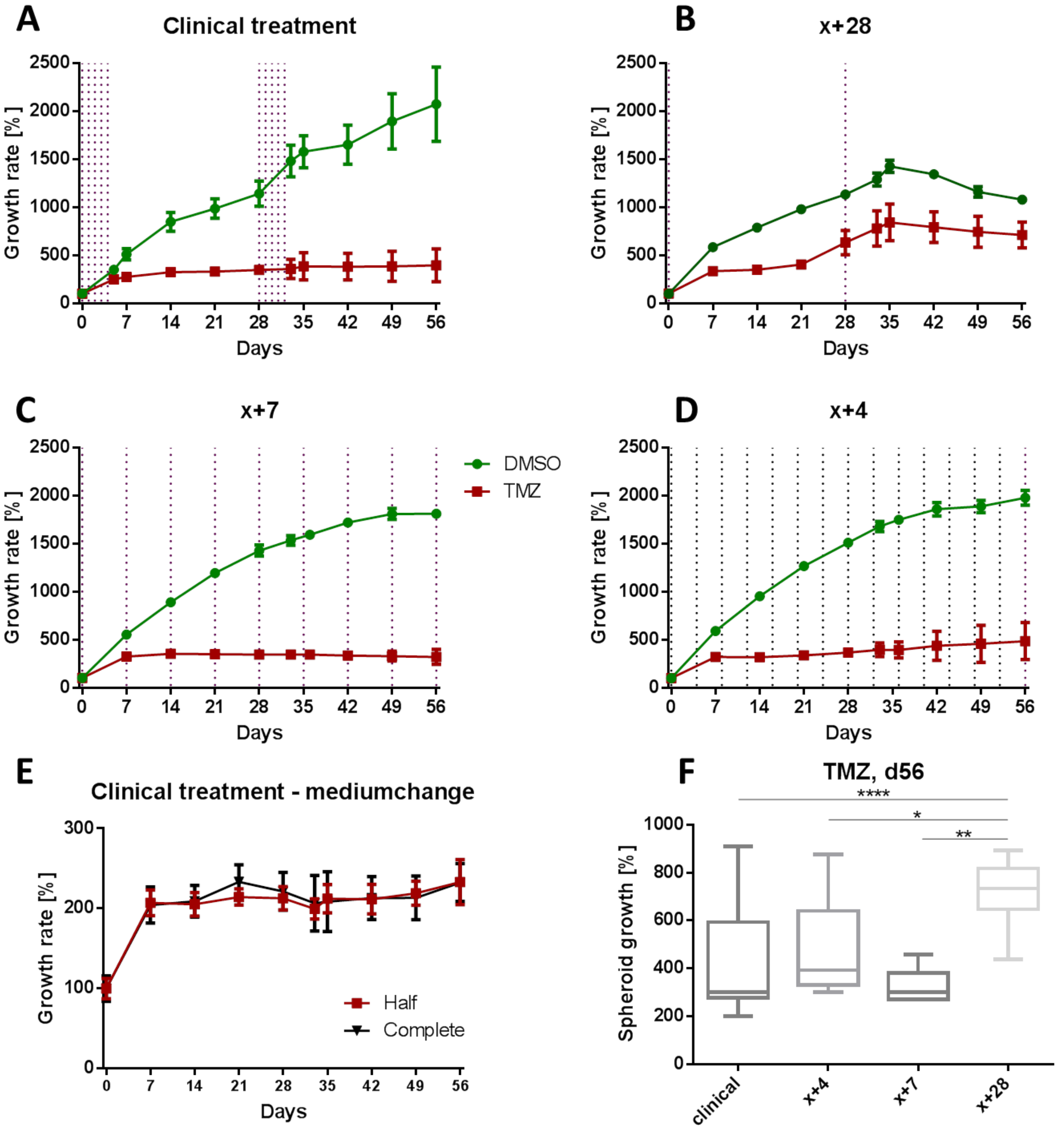

Figure 6.3 Testing of different TMZ dosing schemes.
U87 spheroids were treated following the clinical treatment scheme (5 days TMZ + 23 days rest, A), once in 28 days (x+28, B), once a week (x+7, C) and once every four days (x+4, D). Two-month treatment was applied. Spheroid areas were measured in Fiji and growth evolution was presented normalized to the first day of the experiment. Green lines represent control (DMSO treated) and red lines TMZ treated spheroids. Vertical dot lines mark treatment days. Moreover, the effect of medium change was studied on the growth of treated spheroids (E). Since there was no difference, growth of the treated spheroids on day 56 was compared directly, without normalization and was presented as a box plot (F). ****p <0.0001, *** p <0.001, ** p< 0.01, * p < 0.05

First of all, some differences were seen in the growth of control spheroids, but, as shown in 6.1.2. spheroid growth depended on nutrient availability. The same test was done with treated spheroids. Still, no difference was observed in their growth, as shown in Figure 6.3E. Given that, the behavior of treated spheroids with different treatment schemes was compared without normalization to control.

We observed that the response was very similar in all dosing schemes during the first two weeks. Spheroids grew significantly up to day 7 when their size was stabilized. In the x+28 scheme, as shown in Figure 6.3B, spheroids started increasing their size slowly after day 14, but the growth was more prominent and similar to control growth from day 21. After the second TMZ dose on day 28, the delayed effect was seen again, as spheroids continued growing until day 35 when they stabilized. The evolution of spheroids in this treatment scheme signified that just one TMZ dose is insufficient to prevent tumor progression. In clinical, x+7, and x+4 schemes (Figure 6.3A, C, and D), spheroid size was stable and homogeneous up to day 21, but, later on, higher heterogeneity was observed. However, the spheroid growth and differences between these treatment schemes were insignificant at the end of the experiment.

Detailed analysis of treated spheroids in the second treatment cycle showed that, even though all the spheroids were treated the same way and maintained in the same conditions, not all had the same behavior. As it can be observed in Figure 6.4, the aforementioned heterogeneity was a result of the presence of spheroids that restarted their growth, suggesting the possible resistance development (TMZ-R).

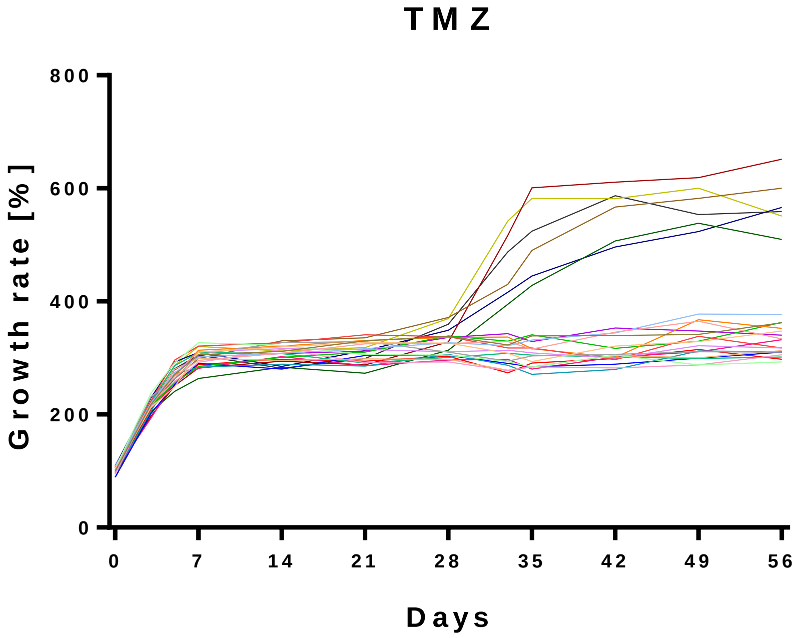

Figure 6.4 Behavior of individual spheroids in one experiment.
Spheroids from the clinical treatment scheme are presented as an example. Up to day 21 all spheroids had similar behavior. Then, two populations could be distinguished, one that maintained the size, and another that reactivated the growth.

In x+28 dosing scheme, all spheroids reactivated the proliferation, even though they did not reach the same level, indicating that just one TMZ dose is not sufficient to prevent tumor progression. On the contrary, in clinical treatment, x+7 and x+4 schemes, separation of two populations was observed (Figure 6.5). In one treated population, spheroids maintained their size, while the proliferation and growth were reactivated in the other. We observed that 25% of spheroids gained resistance in clinical treatment, 17% in x+7, and 40% in x+4 treatment. These results might indicate that temporally spaced treatments could be more effective. Beier et al. showed that an alternating dosing scheme (7+7) decreased the number of clonogenic cells compared to continuous dosing (21+7) in neurosphere culture[342]. However, they used different TMZ concentrations depending on the treatment scheme, while we used the same concentration to control the number of variables between the conditions. It seemed that x+7 treatment scheme could improve the effect of TMZ and lower the resistance development. However, a more extensive study should be conducted to confirm this hypothesis.

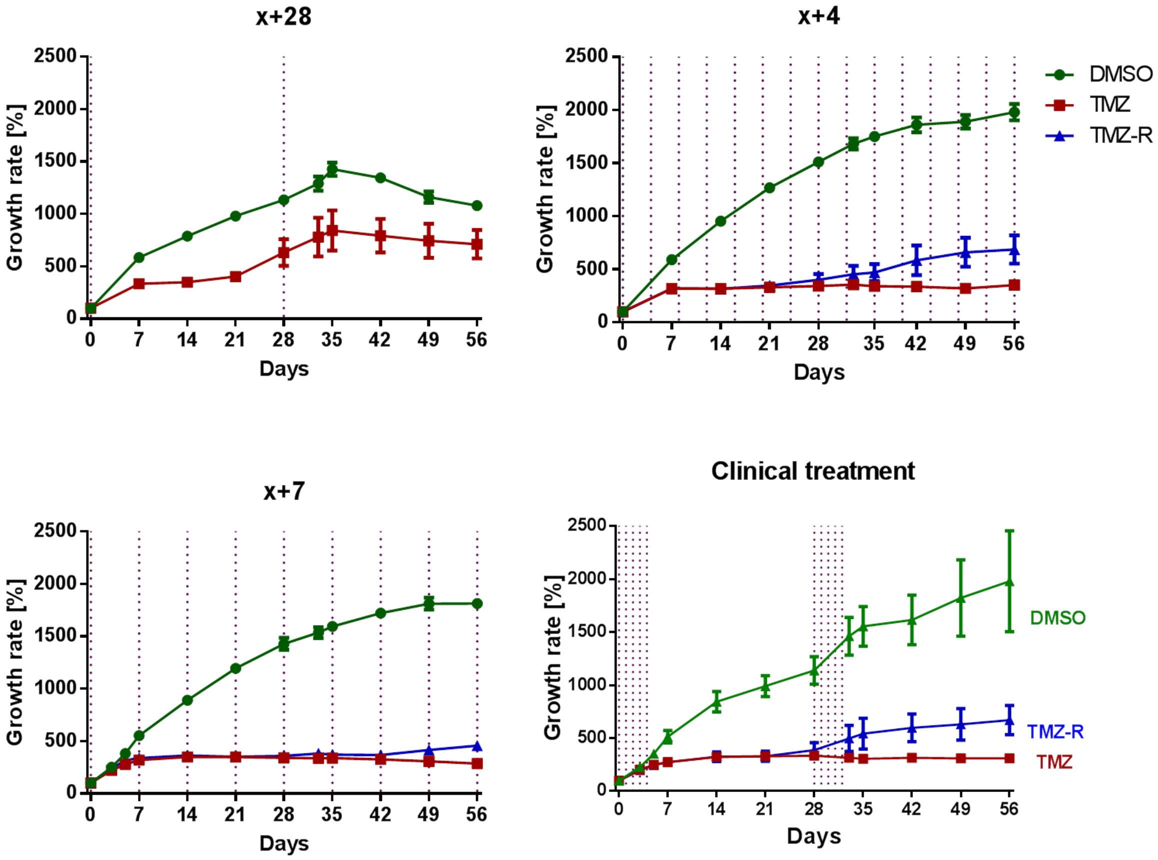

Figure 6.5 Separation of resistant spheroid populations.
In x+28 scheme all spheroids behaved similarly, while in the rest of the schemes two populations of treated spheroids could be identified.

6.1.3 Study of the characteristics of resistant spheroids

As primarily planned, and after the confirmation that none of the treatment schemes improved the TMZ effect significantly, a clinical treatment scheme was used for further studies to explore better the response of GBM spheroids and the characteristics of the resistant ones.

Control U87 spheroids grew up to 2000% in 56 days, which was undoubtedly significant growth ($p<0.0001$). As shown in Figure 6.6, treated spheroids, instead of declining, increased their size to 300% ($p<0.0001$). We observed that the growth of the treated spheroids was the most pronounced during the first five days (up to 250%, $p<0.0001$) when the effect of TMZ started to be significant. Later on, the growth was slightly lower up to day 14 (from 250% to 320% increase), and then the size was stabilized with a minor increase (from 320% to 335%). During the second TMZ treatment and up to day 35, spheroids reduced their size to 305%. Up to day 56, the tendency was stable, with a slight increase (310%). All the changes in the second treatment cycle were insignificant.

Moreover, the population of TMZ-R spheroids (25±5% of the entire treated population) had the same growth compared with the other treated spheroids during the first 21 days. However, they started afterward expanding and reached doubled size of the stable treated group, as shown in figure 6.6. Nevertheless, although the cells recovered their proliferative capacity, the slope of the growth curve was significantly lower than in control spheroids ($p<0.0001$), suggesting the presence of non-proliferating cells or a slower division rate.

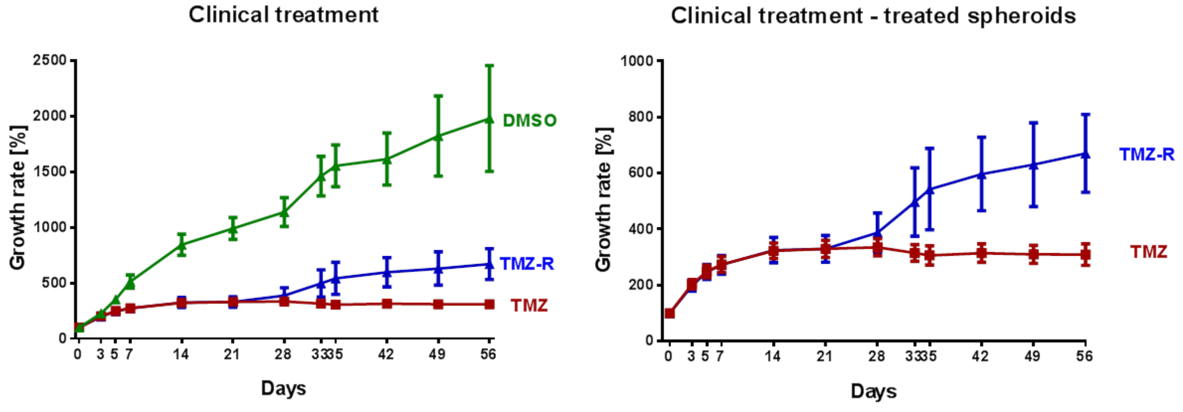

Figure 6.6 Spheroid evolution with clinical treatment scheme.
A. All spheroid populations. B. Closer look to treated spheroids.

The evolution of the growth curve after the first TMZ cycle might signify that TMZ could also activate senescence, the process in which cells stop dividing but do not die[343,344], effectuating a cytostatic response instead of cytotoxic. Different groups have already demonstrated the cytostatic effect of TMZ in 2D cell culture, and that it was even more common than the cytotoxic effect[337,339,345,346]. Senescence was considered an irreversible process, but different studies have recently demonstrated that senescent cells can re-enter the cell cycle and activate proliferation[347,348]. Oliveira Silva et al. observed this effect in 2D GBM cell culture after TMZ treatment, as senescence was the dominant state on day 10 in p53 wild type cell lines (U87), but 2 days later, proliferative capacity was recovered[349].

6.1.3.1 Changes in spheroid morphology

Viability staining at the end of the experiment confirmed that spheroids were alive in all experimental groups (Figure 6.7A). However, differences not only in spheroid size but also in cell size were observed. Cells in the control spheroids were the smallest ones and the most homogeneous. All treated cells were highly heterogeneous but significantly bigger than control cells. However, cells from TMZ-R spheroids were, in turn, significantly smaller than the cells from the TMZ group (Figure 6.7C). Cell size change has also been described in 2D cell culture after TMZ treatment. Wang et al. showed that TMZ up-regulated dynein, cytoplasmic 2, heavy chain 1 (DHC2), a cytoskeleton protein, which promoted protrusion synthesis, extension, and maintenance[350]. This may explain why TMZ can induce changes in cell morphology. Moreover, the interplay of cell growth activation and cell cycle blockade leads to cell volume increase and DNA-to-cytoplasm ratio disruption, which further promote senescence[351].

Additionally, nuclear size was measured, and a similar tendency was observed (Figure 6.7B,D). As mentioned earlier, TMZ produces G2/M arrest, and at this point, cells have already replicated DNA, and more chromosomes can be present, so nuclei can be larger[336].

To study better the spheroid evolution, histology sections and hematoxylin and eosin staining were performed. Additionally, immunohistochemistry was done for Ki-67, a widely used marker for cell proliferation, as it accumulates during the S, G2, and M phases of the cell cycle[352]. Results are shown in Figure 6.8.

At the beginning of the experiment, before separating the control and treated group, all cells had heterogeneous round nuclei. Moreover, around 5% of cells were Ki-67 positive. On day 5, as spheroids grew, control cells were more elongated, and approximately 65% of them marked positive for Ki-67, meaning a high proliferation rate. Nuclei were significantly bigger compared to day 0 ($p<0.0001$, Figure 6.9) with more prominent nucleolus and open chromatin, signifying transcriptionally active cells. Similar nuclei were observed in treated spheroids, also on day 5, but they were even bigger compared to control nuclei. The proliferation rate observed in TMZ treated spheroids on day 5 was slightly lower than in control spheroids (50%). Unlike control spheroids, some apoptotic cells were seen in treated spheroids, signifying that TMZ has some cytotoxic effect. Moreover, nuclei were more separated in TMZ treated samples than in control ones (data not shown), suggesting that cells could be bigger in treated spheroids. At this point, differences in size between control and treated spheroids started to be significant (p<0.0001).

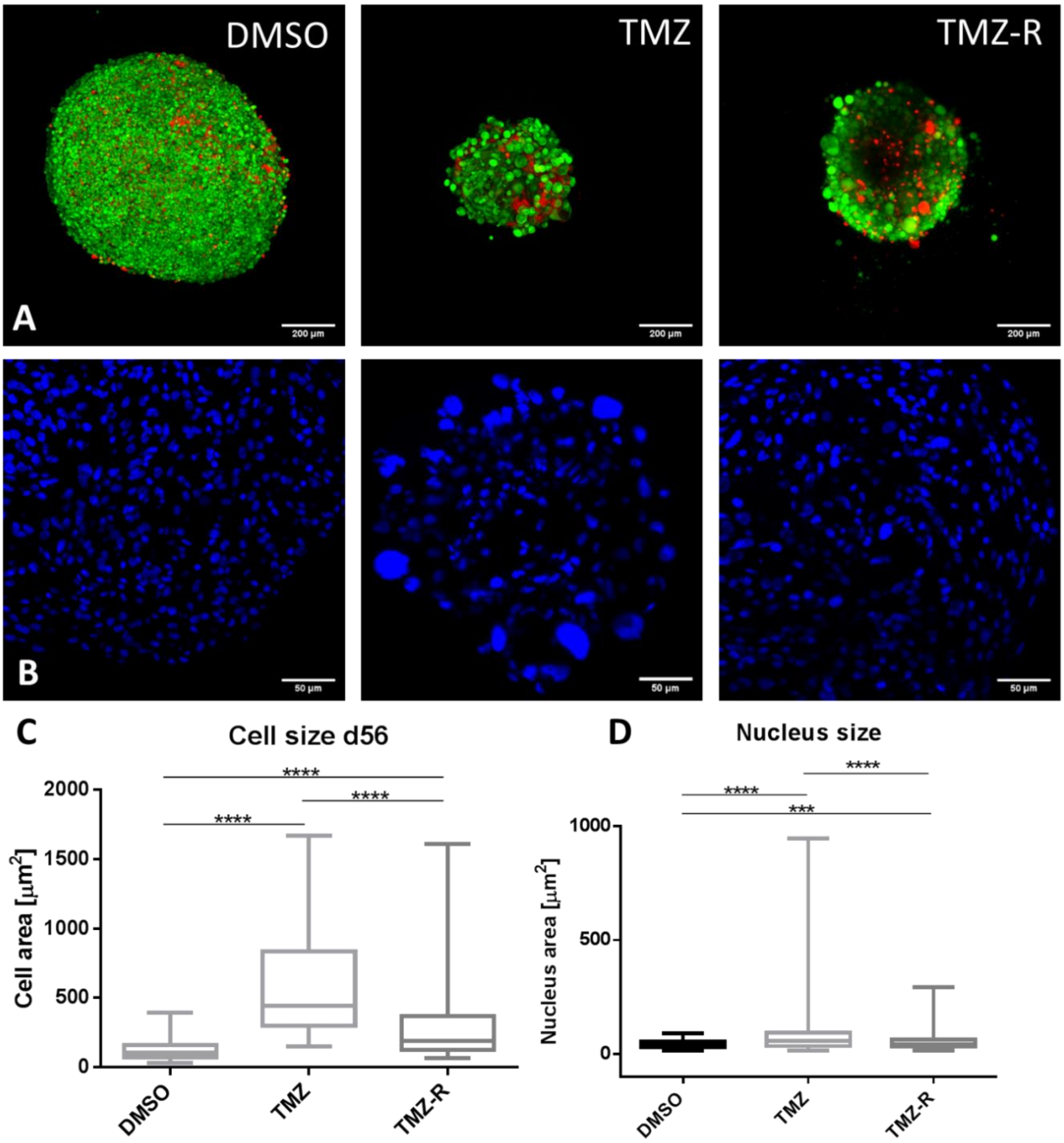

Figure 6.7 Comparison of cell and nucleus size in control and treated spheroids.
A. Confocal images of CAM/PI stained spheroids confirming cell viability after 56 days. Scale bar is 200 µm. B. Confocal images of Hoechst 33342 stained spheroid sections. Scale bar is 50 µm. Fiji was used to measure elements on these images, and results are presente8 as box plots of C. Cell size and D. Nucleus size. ****p <0.0001, *** p <0.001, ** p< 0.01, * p < 0.05

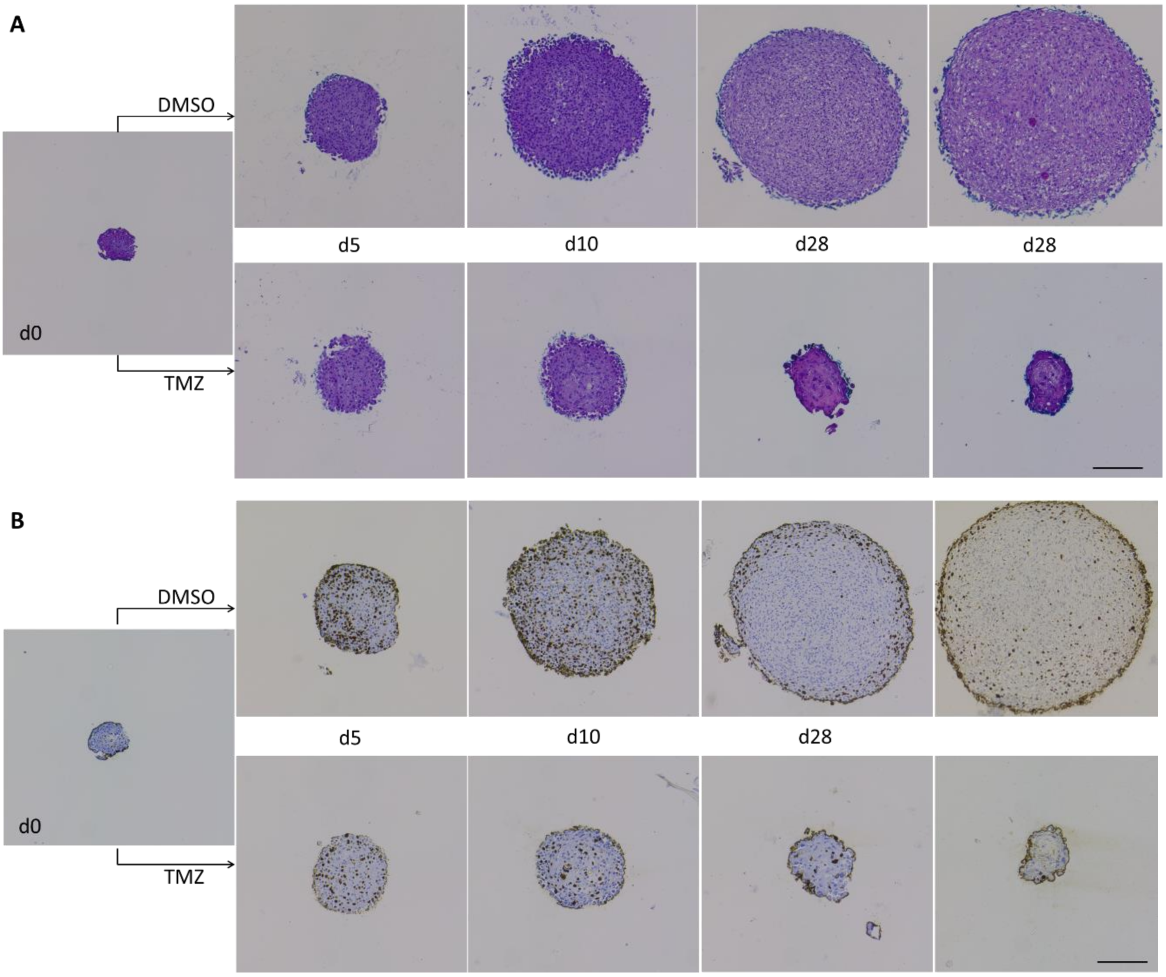

Figure 6.8 Histological characterization of U87 spheroids during the first treatment cycle.
Spheroids were prepared as formalin-fixed paraffin-embedded blocks and 3µm sections were analyzed. A. Hematoxylin and eosin staining revealing the spheroid morphology. B. Immunohistochemical detection of proliferation marker KI-67. Scale bar is 200 µm.

Table 6.1 Proportion of Ki-67 positive cells in control and TMZ-treated spheroids

	Day 0	**Day 5**	**Day 10**	**Day 28**	**Day 56**
DMSO	5%	65%	35%	18%	10%
TMZ	5%	50%	30%	7%	7%
TMZ-R	/	/	/	/	20-60%

On day 10, a high level of proliferating cells was still present in control spheroids, even though it was lower than on day 5 (35%). Positive cells were preferentially located closer to the borders of the spheroid. Many vacuoles were observed in the central part, which could result from cell death, edema, or cytoplasm reorganization. As the spheroids in this phase had a radius around 400 µm, gradients of nutrients, oxygen and waste could be responsible for the explained morphology. Treated spheroids had a radius of approximately 200 µm at this point, so a significant difference in size between control and treated spheroids could be clearly appreciated (see Figures 6.6 and 6.8). In treated spheroids, a lower number of Ki-67 positive cells (30%) was observed, and they were distributed throughout the spheroid. Nuclei size was not changed compared to day 5, neither in control nor in the treated group.

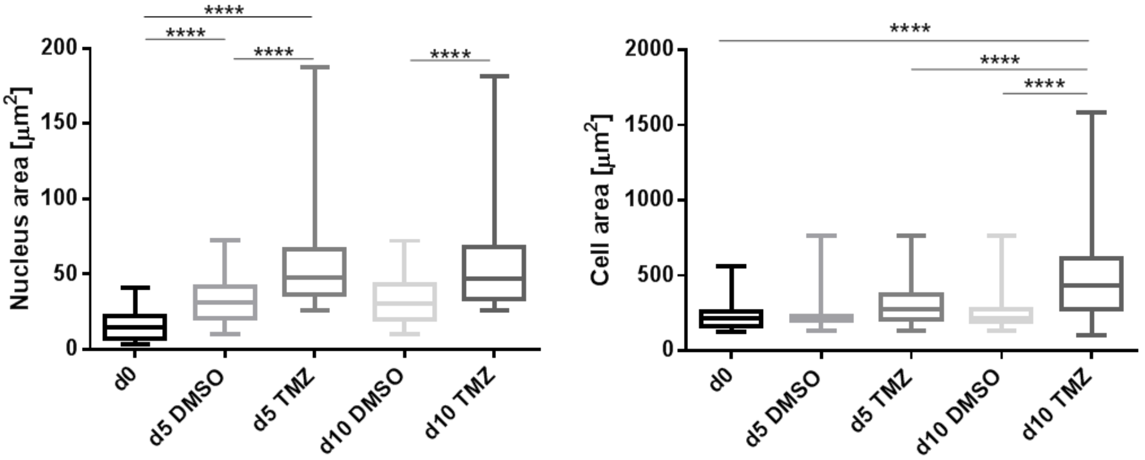

Figure 6.9 Nucleus and cell size during the first 10 days of the treatment cycle.
A. Nucleus area was measured from H&E images. B. Cell size was measured as cell area from CAM/PI images. ****p <0.0001, *** p <0.001, ** p< 0.01, * p < 0.05

To check if the lower nuclear density observed in TMZ treated spheroids resulted, at least partially, from the cell size increase, as hypothesized above, we measured the cell area of CAM-stained spheroids. Results shown in Figure 6.9B indicate that the size of treated cells on day 10 increased significantly (p<0.0001) compared to the control group at the same time point. Moreover, those differences were also significant when the size of TMZ treated cells at day 10 was compared with TMZ treated cells on day 5 and day 0.

These results suggested that the initial growth of treated spheroids resulted from both proliferation and increase of the cell size, explaining the significant difference in spheroid diameter among the control and the TMZ treated group.

At the end of the first cycle, on day 28, the distribution of the nuclei in control spheroids was messier, and their size was heterogeneous. Some apoptotic cells were observed. Ki-67 positive cells (18%) were present only on the spheroid´s surface. Moreover, between nuclei, some fibrous structures were perceived. Whether those structures correspond to the synthesized extracellular matrix or cytoplasmic condensation is still under investigation. Treated cells had more rounded morphology and more heterochromatin. Around 7% Ki-67 positive cells were present, demonstrating a significant increase in the cell proliferation rate difference when compared to the control at this time point.

At the end of the experiment (day 56, shown in Figure 6.10), there were more apoptotic cells and more vacuolated nuclei in a control spheroid. Around 10% of cells marked positive for Ki-67, following the tendency observed of reduction in proliferation as the days of the experiment progress. Meanwhile, giant nuclei with prominent nucleolus were present on the surface of the treated spheroid, while small ones were located in the center. The Ki-67 positive rate did not change from day 28 in TMZ treated spheroids. A more disintegrated zone was observed in the center of the spheroid, potentially signifying cell death. Regarding TMZ-R spheroids, we observed two clearly different zones, one more similar to the treated spheroids, with prominent nuclei and low Ki-67 positivity, and another more similar to control spheroids, with small nuclei and a high level of Ki-67 positive cells (20-60%). At the end of the experiment (day 56), TMZ-R spheroids had the same size as control spheroids around day 10, when there was a high level of proliferating cells. Ki-67 expression percentages along the experiment have been summarized in Table 6.1.

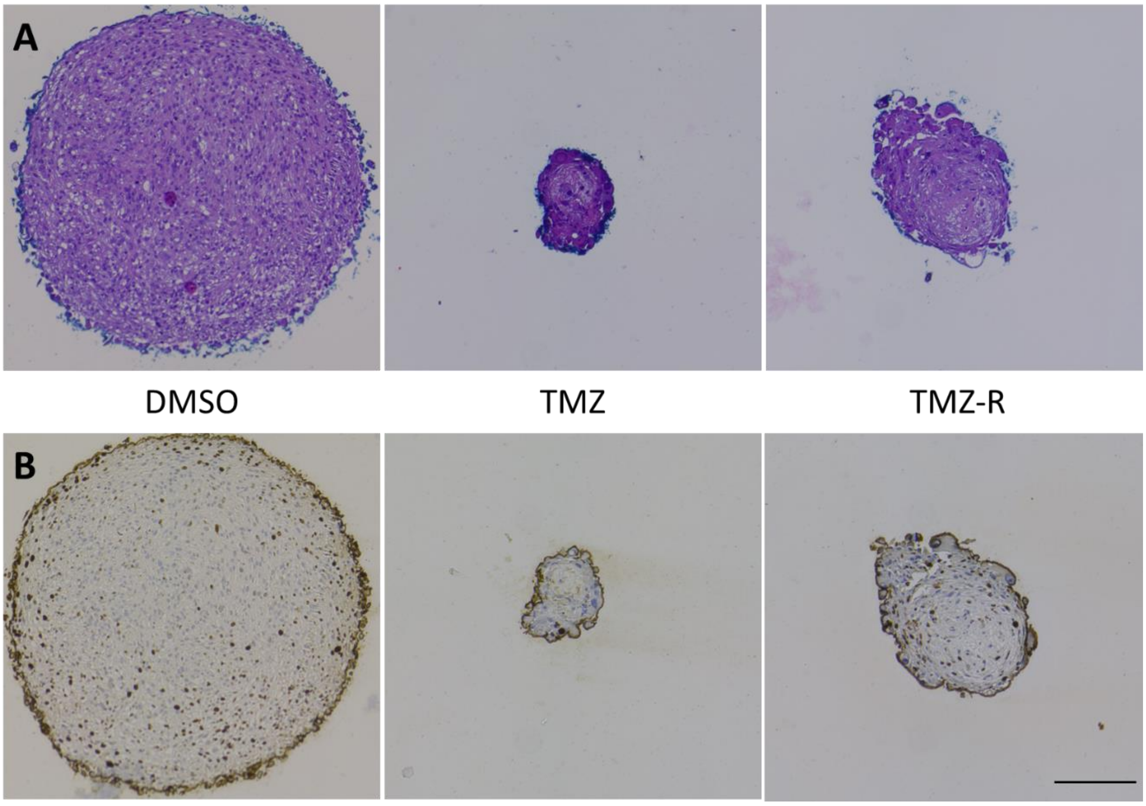

Figure 6.10 Histological characterization of the spheroids at the end of the second cycle (day 56). Hematoxylin and eosin staining (A) and immunohistochemical detection of KI-67 (B) demonstrate differences between different spheroid groups. Scale bar is 200 µm.

To sum up, the cells forming TMZ-R spheroids were bigger than DMSO spheroids, but significantly smaller than TMZ spheroid, and so were the nuclei. On the histology image, two parts could be distinguished within these spheroids. One of them was more similar to treated spheroids, with vacuolated cells, bigger nuclei, and low proliferation rate. The other part had the morphology of the control spheroid, with small nuclei, and high proliferation.

6.1.3.2 Changes in the expression of genes related to drug resistance

Different signaling pathways are involved in drug resistance development, so it is important to study the mechanisms responsible for resistance development. To determine the changes produced in our spheroids, we used the RT2 profiler PCR array, which allowed simultaneous analysis of 84 genes related to cancer drug resistance. The genes studied controlled the cell cycle, DNA damage and repair, drug metabolism, drug resistance, or coded hormone receptors, growth factor receptors, and transcription factors. Results of the arrays were presented as volcano plots, which take into account fold regulation and statistical significance and can be seen in Figure 6.11. The change in the expression was considered relevant if the absolute value of fold regulation was higher than two and statistically significant (p<0.05).

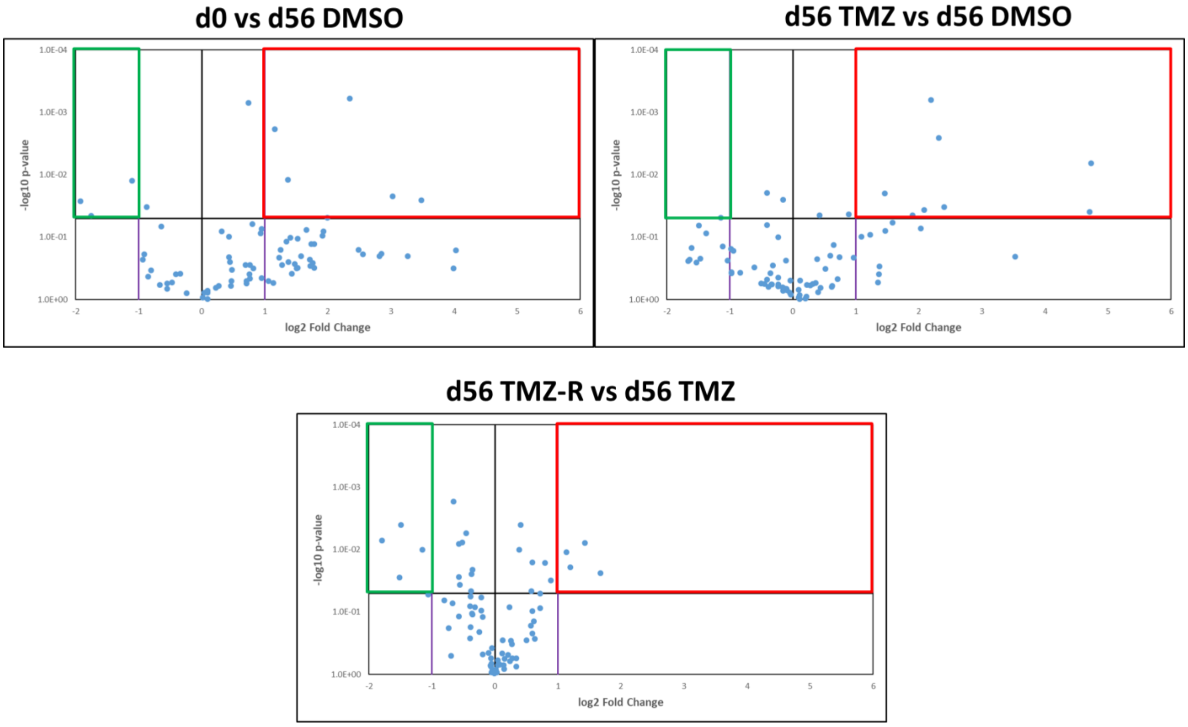

Figure 6.11 Cancer drug resistance gene expression in different spheroid populations.
Volcano plots comparing fold changes of gene expression between samples indicated in the title of each plot. Each dot represents one gene. Horizontal line represents p-value of 0.05, vertical black line fold value of zero and violet fold change of 2. Red framed dots are upregulated significantly, while the green framed dots are downregulated significantly.

To understand the temporal evolution of our spheroids, we compared the gene expression at the beginning and the end of the experiment in the control group. Six genes were significantly up-regulated, signifying that the simple growth and spontaneous change of the conditions within the spheroid (gradients in the interior) could lead to the enhanced expression of genes associated with resistance development. Enhanced genes were coding for transcription factors (*AHR, NFKB2*), hormone receptors (*ESR2, RXRB*), growth factor receptor (*IGF1R*), and drug metabolism (*SULT1E1*). Most of the genes are reported as overexpressed in GBM and related to stem cell phenotype, which leads to faster tumor progression and poor response to therapy[353–357]. However, *RXRB* and *ESR2* are also described as tumor suppressors[358,359]. Moreover, *SULT1E1*, apart from being a xenobiotic catalyzer, could inhibit breast cancer growth and invasion[360]. Overexpression of tumor suppressor genes could be related to the lower proliferation rates observed in control spheroids on day 56.

On the other hand, three genes were down-regulated in control spheroids on day 56 compared to day 0 (*ABCB1*, *ABCG2*, and *CYP1A1*). *ABCB1* and *ABCG2* proteins are dominant efflux proteins on the blood-brain barrier and are responsible for low therapy response[24,25,97,99,361]. These transporters are down-regulated in aberrant microvessels in GBM compared to the healthy brain[362]. Moreover, they are up-regulated in drug-resistant and stem cells. However, mRNA and protein expressions do not always correlate, depending on the post-transcriptional regulation[363]. *CYP1A1*, one of the most important members of the CYP450 family, is involved in the metabolism of different endogenous and exogenous compounds[364].

To determine if the treatment disrupts gene expression, we compared TMZ and control (DMSO) spheroids on day 56. Eight genes were up-regulated, and one was down-regulated in the treated group. The most enhanced genes in the treated group were the ones involved in drug metabolism (*CYP1A1*, *CYP2B6*, *CYP2C19*, *NAT2* and *SULT1E1*), then cell cycle (*CCND1* and *CDKN1A*) and the one coding for one growth factor receptor (*ERBB4*). The function of drug metabolism genes is unknown in GBM. Their up-regulation reduces chemotherapy efficacy in other tumors[365]. However, the metabolism of TMZ does not depend on enzyme activity, as it is spontaneously degraded in physiological pH, so a more detailed study of these genes is needed. Affected cell cycle genes have opposite functions. Cyclin D1 (*CCND1*) controls cell cycle progression, while *CDKN1A* is involved in cell cycle arrest. Simultaneous activation of these genes was shown important for senescence activation. When cell growth is active, and the cycle is blocked, cells grow, but they cannot divide, so the senescence is activated[366].

Apart from up-regulated genes, *MYC* was significantly down-regulated. As a proto-oncogene, its down-regulation leads to cell cycle arrest, apoptosis, and reduced proliferation, and Yamaki et al. showed that TMZ suppresses MYC[367]. Gene expression changes seen in treated spheroids reinforce our hypothesis about the cytostatic effect of TMZ.

Finally, to discover genes contributing to the TMZ resistance, we compared gene expression between TMZ and TMZ-R spheroids. Four genes were up-regulated in resistant spheroids, and they were associated with drug metabolism (*ARNT*), growth factor receptor (*ERBB2*), transcription factor (*MYC*), and drug resistance (*TOP2A*). *MYC*, apart from being proto-oncogen, was shown responsible for drug resistance in different tumors, including GBM[368]. The role of the rest of the genes in GBM is still largely unknown. *ARNT*, coding for HIF1b, supports tumor growth and angiogenesis, and up-regulates multidrug resistance proteins in some cancers[369]. *ERBB2* is involved in GSC maintenance and tumor progression[370]. *TOP2A* is overexpressed in proliferating cells and correlates with aggressive tumors[371]. It was shown that TMZ inhibits *TOP2A*[372], which was seen in treated spheroids compared to control (even though the change was not significant). However, in TMZ-R it was up-regulated compared to TMZ spheroids, possibly promoting the recovery from the TMZ effects. Five genes were down-regulated compared to TMZ spheroids. They were involved in drug metabolism (*CYP1A1*, *CYP2C19*, *NAT2*), drug resistance (*ABCC3*), or coded for hormone receptor (*AR*). The function of these genes is not well known in GBM. AR is involved in tumor progression and induces resistance to TMZ[373,374]. The specific function of Abcc3 has not yet been discovered, but its expression is high in GBM and can be used as a prognostic marker[375]. Lower expression of *NAT2* was shown to induce higher metastasis and lower survival in colorectal cancer[376].

Having all in mind, a heterogeneous population of cells in TMZ-R spheroids was observed, and that´s why we consider it is important to study the spatial expression of these genes, to understand better the role they have in TMZ-R spheroids. Moreover, distribution of these gene’s encoded proteins could help us identify some post-transcriptional events that could affect the gene based conclusions.

6.3 Conclusions

We replicated a clinical TMZ dosing scheme in the spheroid in vitro model to study the tumor progression and resistance development. U87 spheroids were highly proliferative, replicating the tumor growth. At the beginning of the experiment, there were a lot of proliferating cells in all parts of the spheroid. However, as the spheroid size increased and gradients were generated toward the center, proliferating cells were only present on the spheroid´s surface, where the environmental conditions were more favorable. Moreover, we observed that simple tumor progression led to the enhanced expression of resistance-associated genes, maybe due to the changes in their environmental conditions.

TMZ treatment prevented fast growth in most spheroids by decreasing the number of proliferating cells. Moreover, the treatment increased cell and nuclei size, executing more cytostatic than cytotoxic effects. In addition, TMZ treatment induced cell cycle arrest, prevented tumor progression, and enhanced the expression of membrane transporters responsible for drug efflux.

The cellular population was heterogeneous in the treated spheroid group, so one part of the spheroids could recover from the TMZ effects, reactivating proliferation and acquiring resistance. The behavior of these TMZ resistant spheroids was exactly the same as in treated spheroids during the first three weeks of treatment. However, they started growing again after that period and did not respond to the second TMZ cycle. In addition, they enhanced the expression of both inhibitors and promoters of tumor progression, confirming the mixed cellular population seen on the histology sections. More detailed analysis related to the spatial expression of those genes should be done to correlate with the corresponding spheroid zone.

Overall, spheroids can be a valuable platform for studying tumor progression and drug response, as they can mimic tumor morphology and different populations present in the tumor. In addition, a detailed study of gene expression in different conditions could help develop and test new therapies that would affect all components.

7 Study of tumor microenvironment by using spatial transcriptomics

Different bulk and single-cell multi-omics techniques are being used to study the tumor on different levels (RNA, DNA, proteins, lipids, metabolism)[377]. Still, it is very important to understand the context in which the cells find themselves, how they are organized and how that organization conditions them. Spatial transcriptomics is a relatively new technique, prospering in last years and named method of the year in 2020[378]. It allows combining classical histological methods with in situ hybridization, in situ sequencing, or next-generation sequencing, revealing the microenvironmental context and interactions between elements.

Different commercially available technologies were developed to potentiate these studies and are reviewed in[378,379]. Nanostring and 10x genomics technologies have the highest potential for obtaining the most detailed information. GeoMx digital spatial profiler from Nanostring combines fluorescence protein labeling that enables morphology recognition and gene expression analysis thanks to the incubation with oligonucleotide tags. The region of interest has to be selected and then exposed to UV light to release cleaved probes that will be used for library construction and sequencing. On the other hand, Visium slides have four capture areas containing 5000 barcoded spots of 55 μm with millions of oligonucleotide chains (see Figure 7.1). These chains include poly(dT) sequence, which allows binding of poly-adenylated mRNA. Additionally, the chains include a unique molecular identifier (UMI) and specific sequence coding its exact location on the slide. After tissue permeabilization and retrotranscription of the hybridized mRNA, the DNA transcribed will carry barcodes from the spot where it was synthesized, so it is possible to correlate gene expression with a specific tissue region after the sequencing.

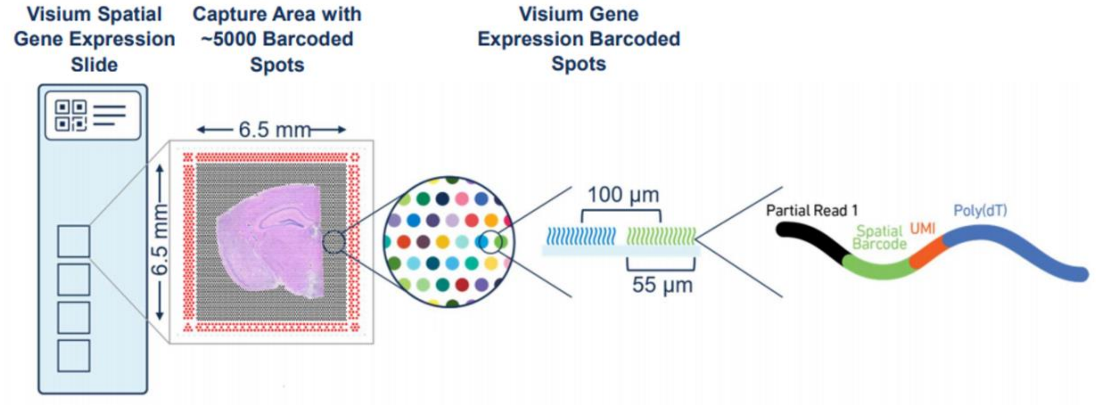

Figure 7.1 Visium spatial gene expression slide.
Image: 10x Genomics

We have chosen for our studies Visium technology because it allows the study of the complete tissue section, correlation with classical H&E image, and, unlike GeoMx, it does not require specific laboratory equipment.

7.1 Results and discussion

Our primary idea was to study differences in TME and genes responsible for drug resistance development between primary and recurrent glioblastomas from the same patient. However, it was difficult to obtain paired samples of sufficient quality. Recurrent GBM cannot always be extirpated, depending on the patient age and state, size of the tumor and zone it occupies[380]. Moreover, samples are generally stored as formalin-fixed paraffin-embedded (FFPE) blocks, as they are used for the diagnosis, but the Visium technique was firstly developed for fresh-frozen tissues. Furthermore, for the correct functioning of the technique, the tissue morphology and RNA should be well preserved. As the tissues were snap-frozen and stored at -80°C, RNA usually had good quality. However, in our experience, some RNA was degraded, possibly because of the presence of big necrotic zone, insufficient or slow freezing, or repeated freeze-thaw cycles. Moreover, freezing without fixation affects the tissue by forming ice crystals, so the morphology is lost. Hence, the optimization of freezing conditions has to be done.

We obtained three primary GBM samples to study the heterogeneity of the tumor and its microenvironment. Patient data are presented in Table 7.1.

Table 7.1 GBM sample characteristics

Sample	Age	Sex	Survival (months after surgery)	Brain zone
GBM1	53	Male	19	Right temporo-parietal
GBM2	71	Female	18	Right frontal
GBM3	78	Female	15	Right temporal

7.1.1 Tissue optimization

First, the permeabilization conditions had to be optimized to assure sufficient RNA release and prevent RNA leaking to surrounding spots. For this purpose, tissue sections were placed on Visium Spatial Tissue Optimization slide, stained with H&E (Figure 7.2A) and then permeabilized for different lengths of time. Next, cDNA synthesis was done with fluorescently labeled nucleotides, and tissue was enzymatically removed (Figure 7.2B) to visualize synthesized cDNA on the slide (Figure 7.3C).

Thirty-minute permeabilization was chosen as optimal, as the fluorescence was the brightest, and the complete tissue section was marked. Moreover, no fluorescence was seen out of the tissue, meaning no RNA was leaking.

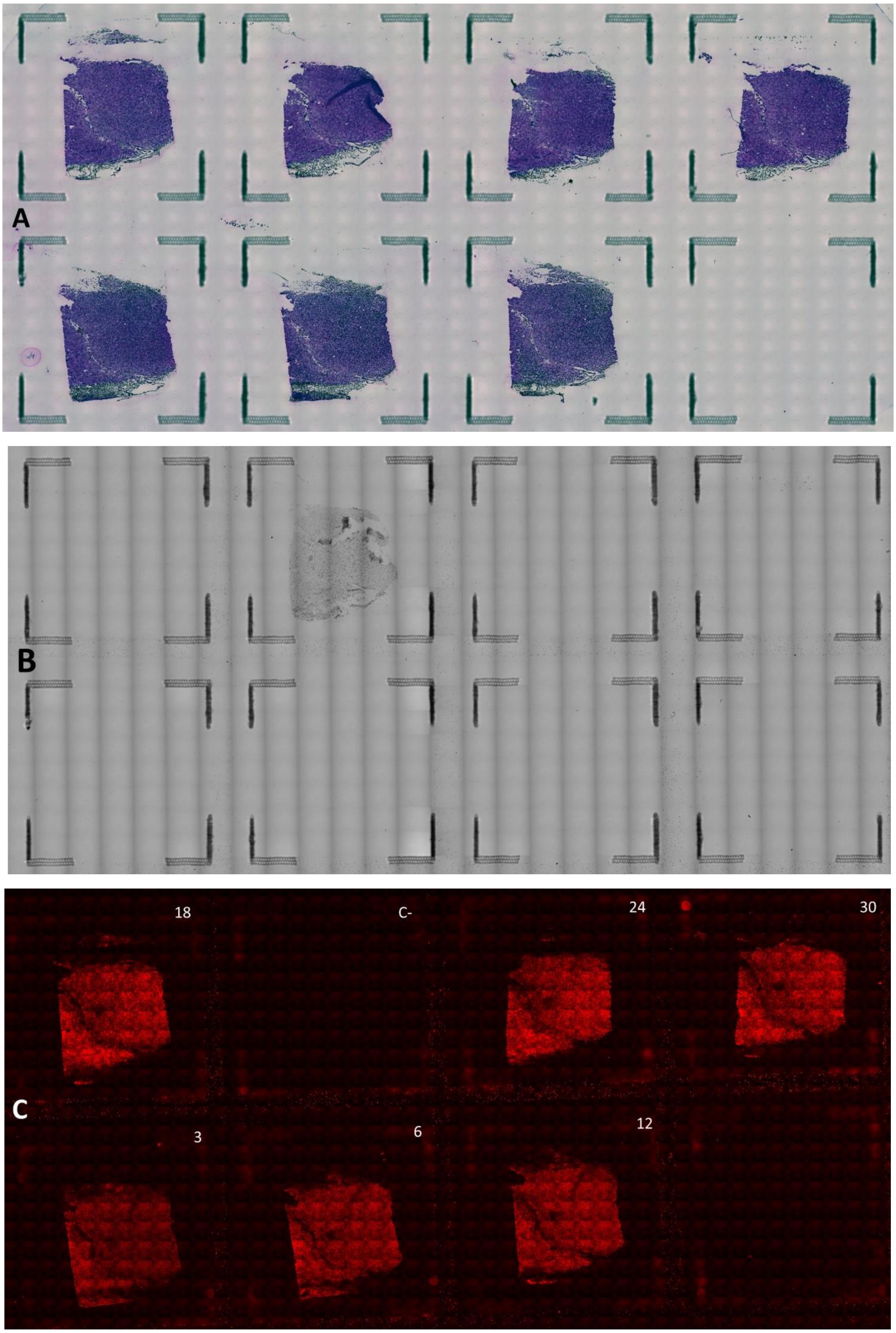

Figure 7.2 Tissue optimization.
To identify optimal tissue permeabilization time, sections were placed on the slide, and stained with H&E (A). Next, tissue vas permeabilized for different period of time (3, 6, 12, 18, 24, and 30 min), and cDNA was synthesized using fluorescent nucleotides. Finally, tissue was removed (B) and cDNA visualized with TRITC filter (C).

7.1.2 Spatial transcriptomics

7.1.2.1 Tumor morphology

H&E staining was done to obtain the image of the tumor morphology (Figure 7.3) that will later be associated with gene expression.

On the GBM1 section, we could differentiate the high density of tumor cells on the left and the artefacted zone on the right. Some nuclei in the artefacted zone seemed to be necrotic, but it was hard to confirm because of the bad morphology. Also, a necrotic zone is more fragile and could be broken more easily during the sectioning. Next to this zone, a higher density of vessels can be seen compared to the rest of the section.

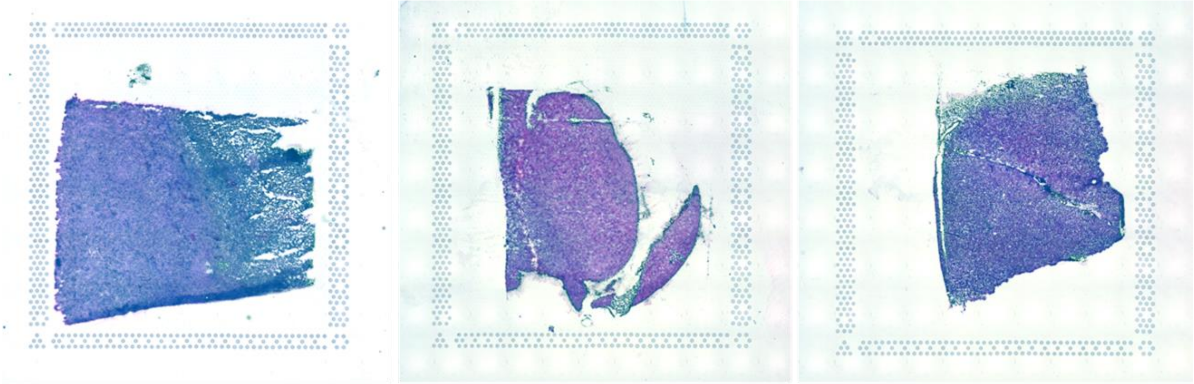

Figure 7.3 Histology of the studied GBM samples.
H&E images of tissue sections. A. GBM1, B. GBM2, C. GBM3.

GBM2 had low cell density and morphology more similar to a healthy brain. However, more vessels could be seen in the upper-right part, perhaps denoting the transition zone between tumor and healthy tissue, for which they are characteristic. Morphology of GBM3 was not well preserved, but the section seemed tumoral, even though the tumor cell density was lower, more similar to the peripheral zone of the tumor. It was homogeneous, with a blood vessel in the middle.

As the morphology of GBM1 was conserved better and it was more similar to typical GBM, this sample was used for a more detailed analysis of gene expression and tumor microenvironment. However, some general results obtained with GBM2 and GBM3 will also be shown, as they sustain the heterogeneity present in this tumor.

After H&E staining, the samples were processed for spatial transcriptomics analysis by permeabilization, cDNA synthesis, library construction and sequencing. As synthesized DNA included the spatial barcode from the slide spots, it was possible to align the histological image with the sequenced data.

7.1.2.2 Quality control

First of all, quality control was done, by checking for each spot the number of Unique Molecular Identifiers (UMI, nCount), number of genes detected (nFeature), and percentage of mitochondrial and hemoglobin genes. Low nCount and nFeature mean insufficient permeabilization or technical problems during the processing. Aigh percentage of mitochondrial genes signifies damaged or dying cells. High hemoglobin presence can suggest blood contamination. All samples used had enough quality, without removing spots from the analysis. The detected numbers of UMIs and genes per spot were in concordance with numbers obtained by other groups[381]

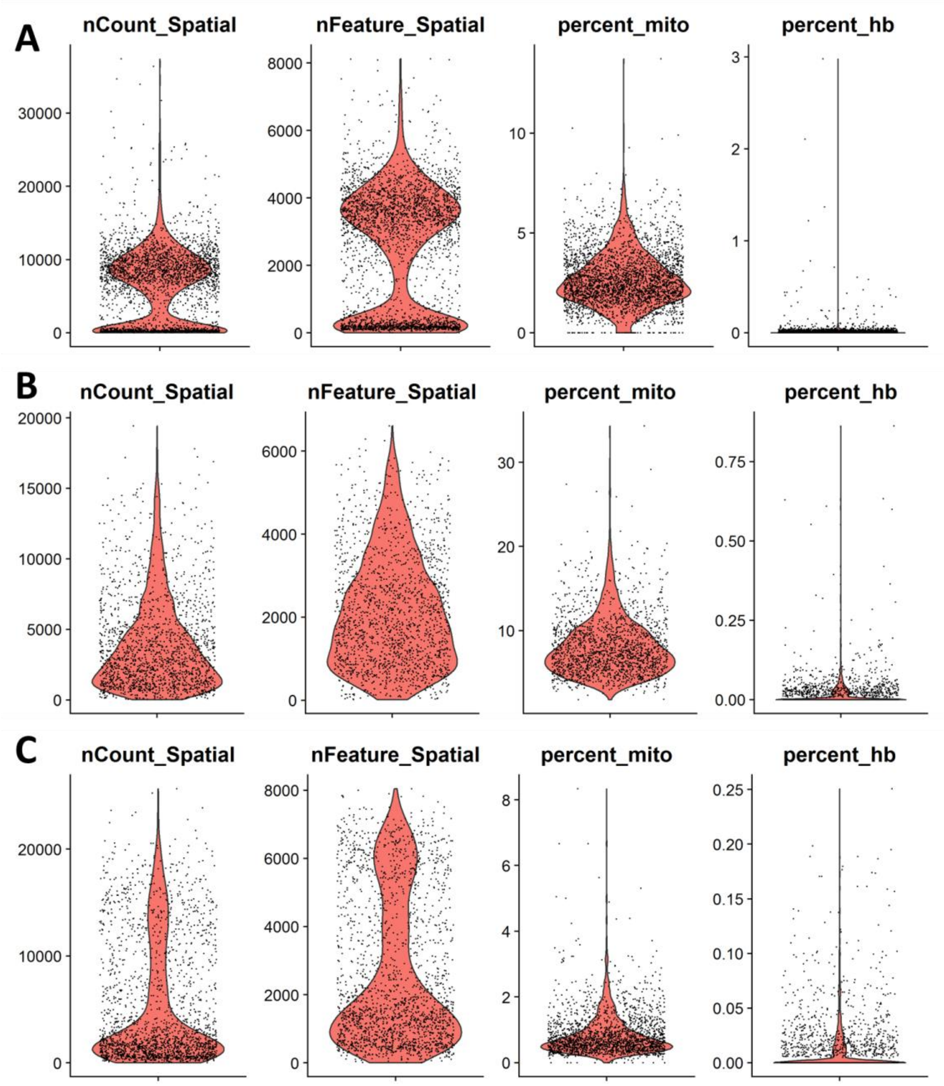

Figure 7.4 Quality check of the RNA sequencing data.
A. GBM1, B. GBM2, C. GBM3. Quality check of the samples is assessed by quantification of total number of molecules detected in each spot (nCount), number of genes detected in each spot (nFeature). Low nCount and nFeature signifies dead/dying cells or empty spot, while high values marks doublets. Moreover, percentage of mitochondial and globine genes is used as a control marker, since their high expression is a sign of damaged cells or blood contamination, respectively.

7.1.2.3 Detection of individual genes – drug resistance and spatially differential genes

As one of the main objectives of this thesis was to evaluate drug resistance development, we wanted to study the expression of genes related to resistance, explained in the previous chapter. Therefore, since the studied tissue was not in contact with TMZ, we visualized the expression of the detected enhanced genes in control spheroids. Changes in expression levels were calculated within the sample, searching for the zones with higher expression of resistance-related genes. We could detect the exact spots with active expression within the tissue (Figure 7.5). *AHR* was the most prevalent and with the highest expression. It is known to promote cell proliferation and invasiveness, hence tumor progression. NFKB2 was preferentially located in the zone close to an artefacted region, while the rest of the genes were more homogeneously distributed within the tissue.

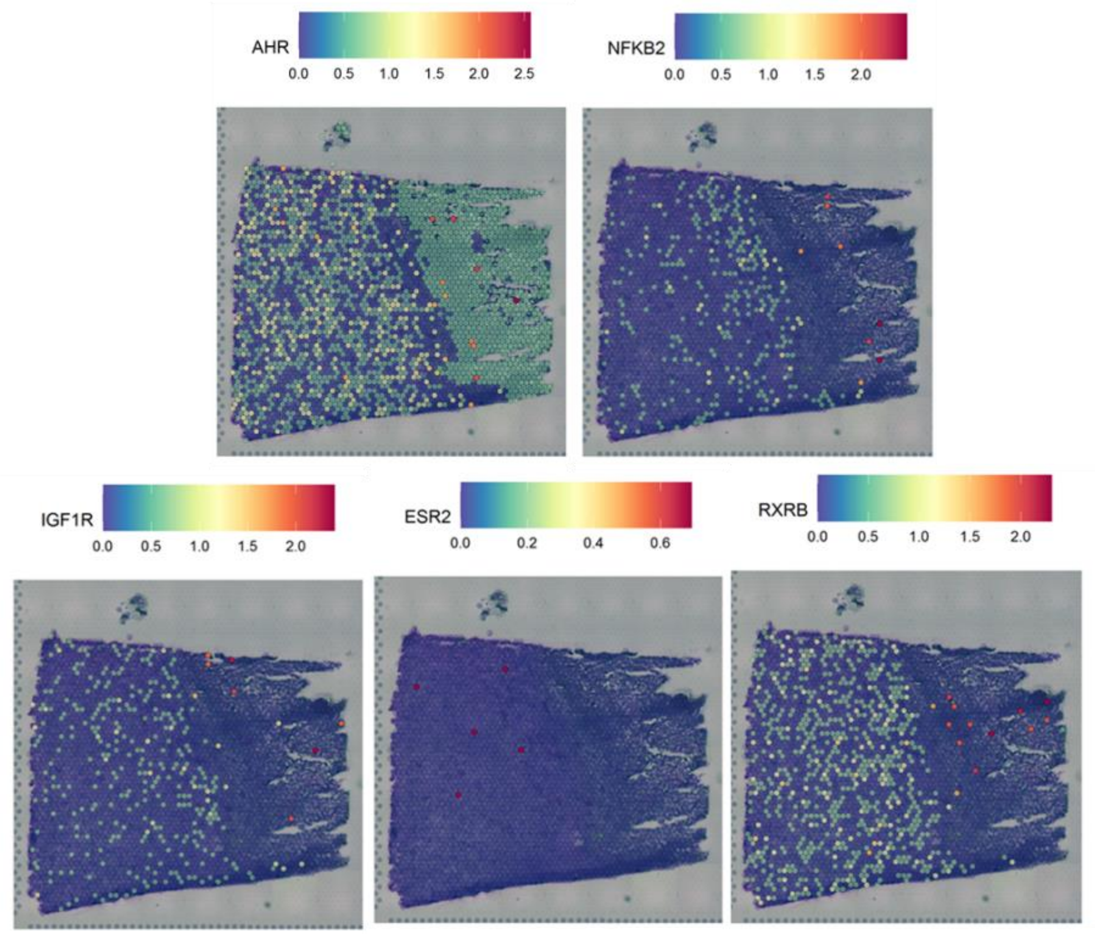

Figure 7.5 Detection of the expression of genes of interest.
Cancer drug resistance genes upregulated because of the progression of the tumor, detected in 6.1.3.2, were visualized on GBM1 sample

Moreover, to find spatially differential genes in the studied tissue, we compared each spot with the surrounding spots, and some of the identified genes are presented in Figure 7.6. By doing this, we observed one decisive advantage of the technique. Some genes were expressed in a thin tissue region and would probably be lost in other types of analysis. It was shown that if just a small number of cells expresses one gene, it can be concealed in the bulk study, or the expressing cells can be missing in the single cell analysis. Moreover, both of these techniques miss spatial information. With spatial RNAseq we can observe the precise location of gene expression and understand its relationship with other genes and morphological context[377].

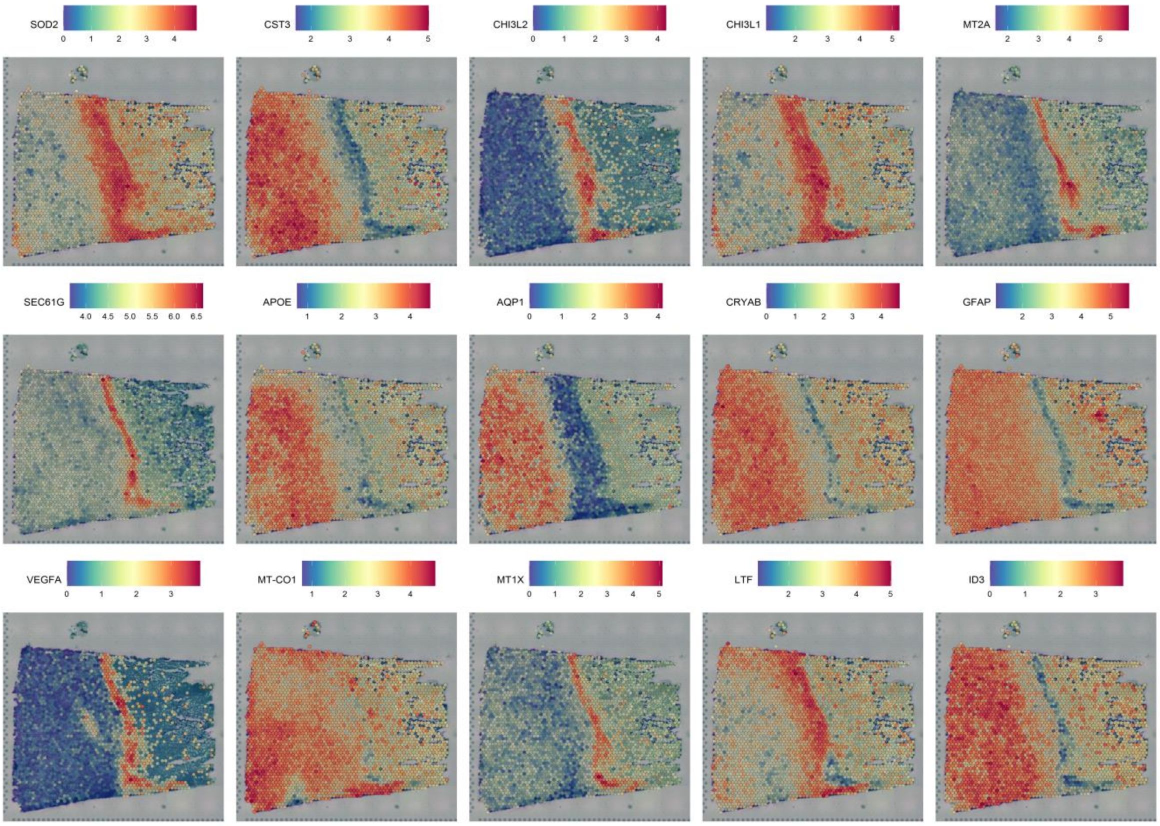

Figure 7.6 Detection of the spatially differential genes in GBM1.
Expression of the each spot was compared to the surrounding spots to encounter differentially expressed genes.

7.1.2.4 Detection of grouped genes – molecular subtypes

Depending on the genetic and transcriptomic alterations observed in the tumor, different GBM molecular subtypes can be distinguished. They are named classical, mesenchymal, neural and proneural subtypes. They have different gene expression patterns, TME composition and different prognoses. Hence it is essential to characterize well the tumor for each patient. Verhaak et al. described an 840-gene list that includes the expression patterns relevant to each subtype and allows identification[51].

Table 7.2 Gene signature of GBM molecular subtypes by Verhaak

Classical	Mesenchymal	Neural	Proneural
EGFR	*CHI3L1*	*NEFL*	*PDGFRA*
NES	*MET*	*GABRA1*	*NKX2-2*
NOTCH3	*CD44*	*SYT1*	*OLIG2*
JAG1	*MERTK*	*SLC12A5*	*DCK*
LFNG	*TRADD*		*DLL3*
SMO	*RELB*		*ASCL1*
GAS1	*TNFRSF1A*		*TCF4*
GLI2			

As proof of concept, we used a few specific genes for each subtype, presented in Table 7.2, to define the molecular subtype of the tumor. However, we observed that different molecular subtypes were present in the same section. For example, GBM1 was a combination of classical and mesenchymal subtypes (Figure 7.7). In GBM2, the neural subtype was the most prominent one (Figure 7.8). This is understandable considering that the morphology of this tissue and the gene expression profile are more similar to a healthy brain. Finally, in GBM3, subtype determination was not so precise, but it was similar to GBM1, the combination of mesenchymal and classical subtype (Figure 7.9).

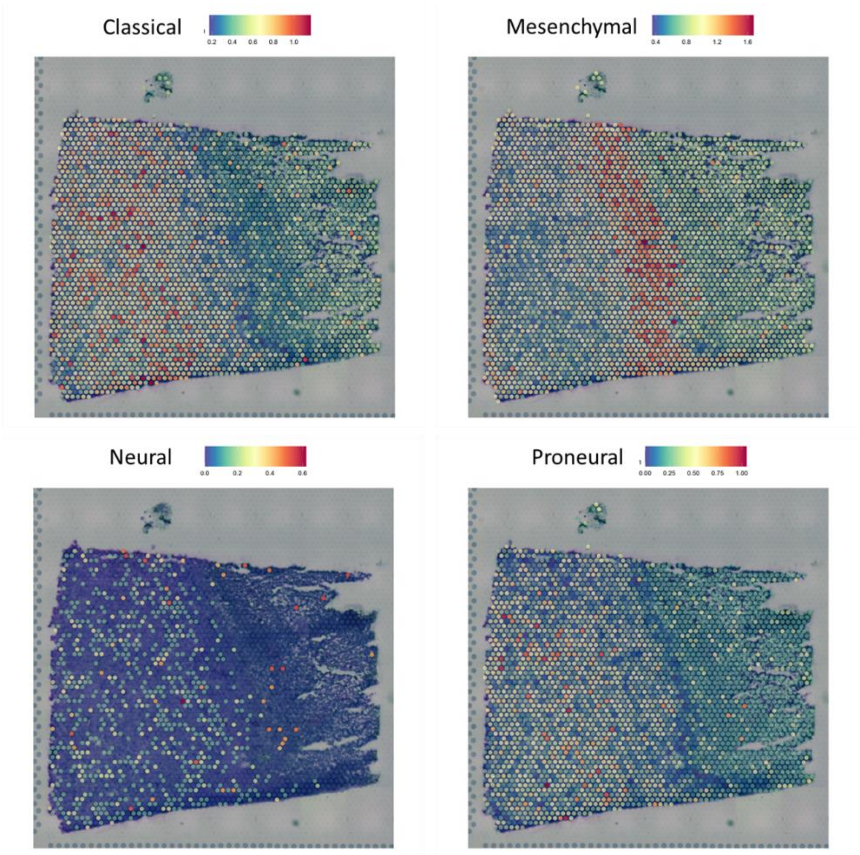

Figure 7.7 Molecular subtype determination of GBM1

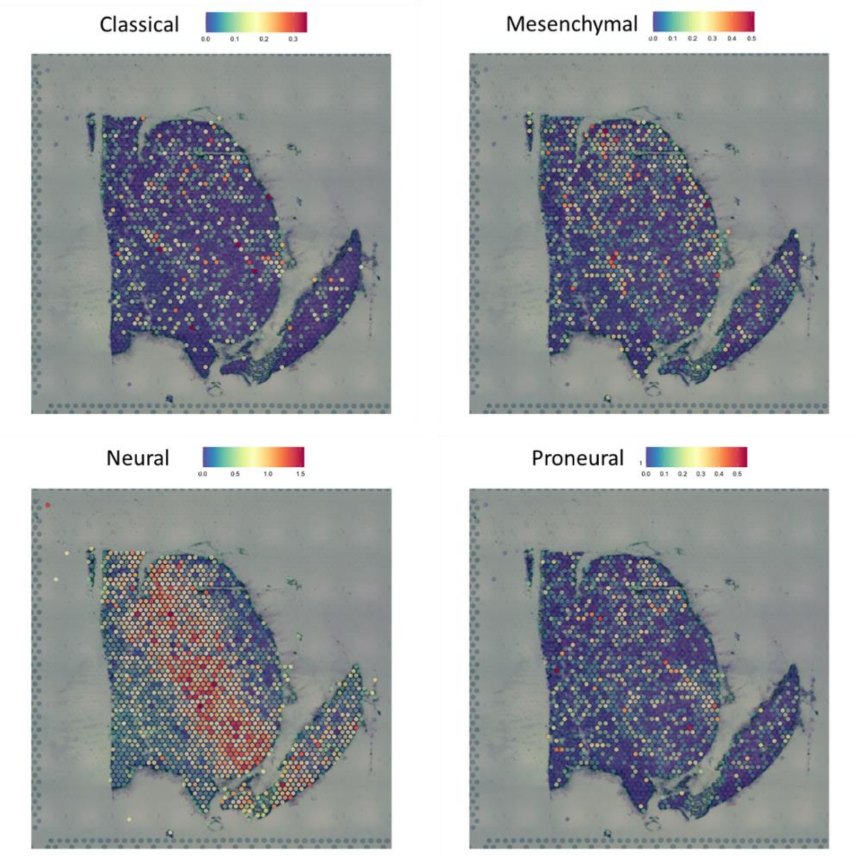

Figure 7.8 Molecular subtype determination of GBM2

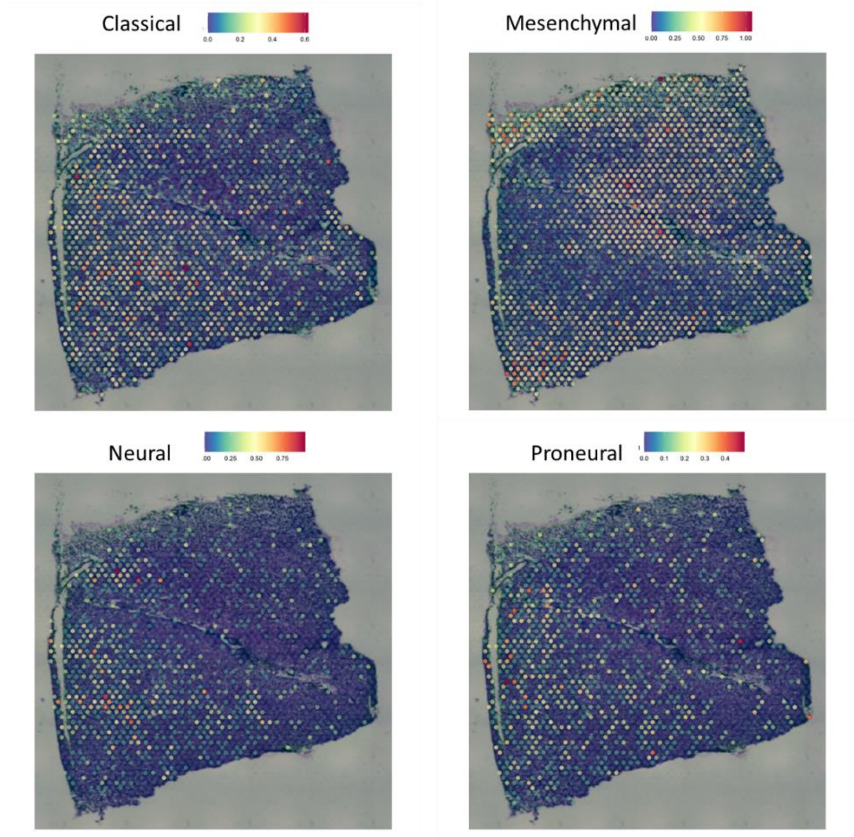

Figure 7.9 Subtype determination of GBM3

We observed that the specific molecular subtype was primarily influenced by the strong expression of one gene. Nevertheless, it gave us an insight into the subtype distribution within the tissue. The study of the complete gene list will be performed to examine better the GBM subtypes and their organization within the tumor.

Different subtypes within the same tumor were already described in the literature. For example, Kim et al. showed that samples from different parts of the same tumor could be identified as a different subtype. Moreover, Puchalski et al. created GBM atlas, where they correlated histology images with gene expression data from distinguished laser microdissected features[55]. However, spatial transcriptomics allows the spatial visualization of GBM subtypes in one tissue section without its disturbance. Hence, a better correlation between the histology and molecular subtype could be studied, and interactions between subtypes could be further explored.

7.1.2.5 Detection of transcriptomic clusters

Principal Component Analysis (PCA), *t*-distributed stochastic neighbor embedding (*t*-SNE) and Uniform Manifold Approximation and Projection (UMAP) dimension reduction techniques were used to determine the similarities in expression patterns between the spots and the Louvain method was applied for spot clustering. Even though the sections were morphologically homogeneous, the gene expression analysis showed that various clusters could be separated within each sample, suggesting that spatial determinants affected gene expression.

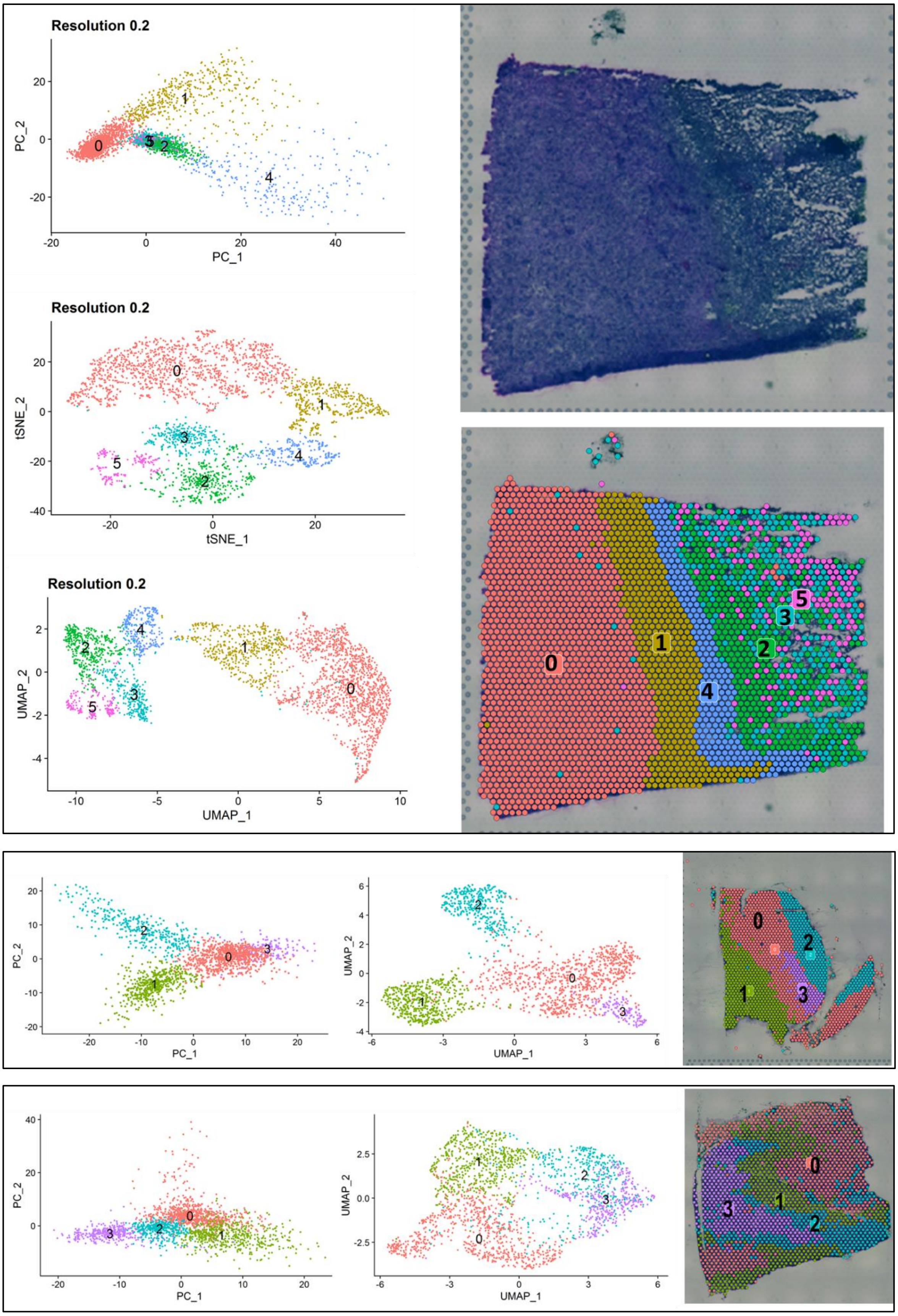

Figure 7.10 Determination of transcriptional clusters in GBM samples.

PCA was done for dimension reduction and result filtering. tSNE and UMAP techniques showed the spatial dependency of the clusters. Since UMAP separates better the detected clusters, it is more commonly used, and here showed for GBM2 and GBM3.

Quality control was also done for clusters. For example, as shown in Figure 7.11, the artefacted zone of GBM1 had a low rate of molecule detection, which could support our hypothesis about the necrotic zone.

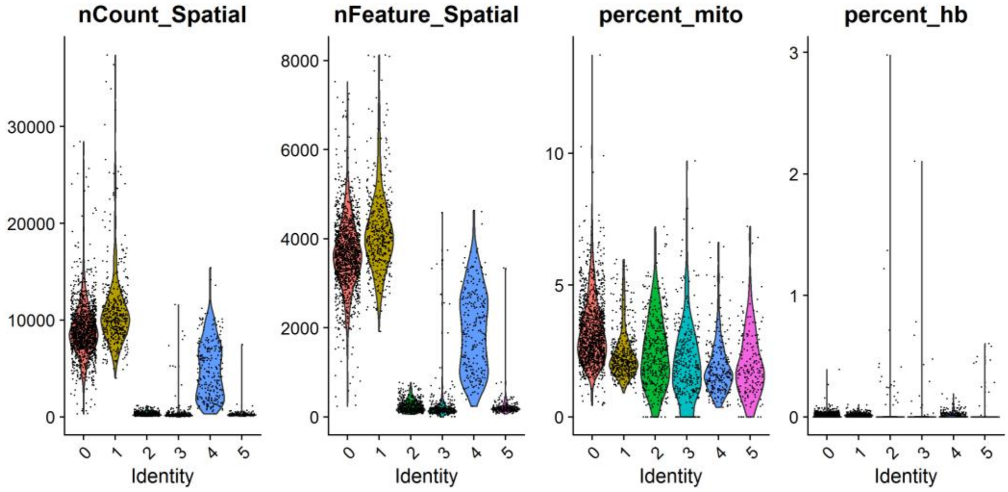

Figure 7.11 Quality control of data captured in each cluster of GBM1.

When we checked gene markers of each cluster in GBM1, we observed, for example, that the above-mentioned zone with higher vascular density coincided with differential increased expression of *VEGFA* and *CHI3L2*, genes involved in angiogenesis[382] (Figure 7.12). Additionally, *MT2A* was described to mark the core of newly diagnosed glioblastoma[383]. It was seen in a thin zone next to the artefacted area, supporting the necrotic core hypothesis.

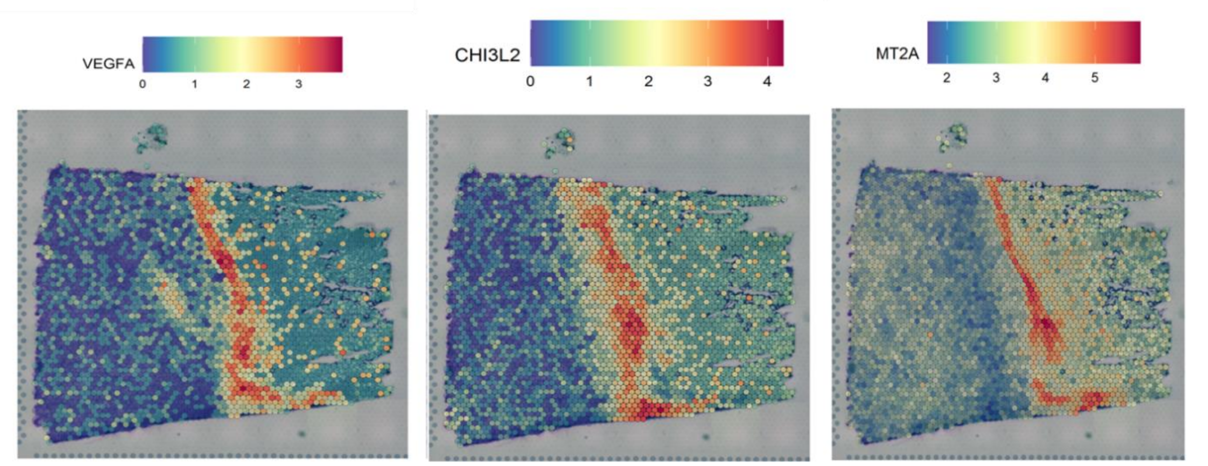

Figure 7.12 Visualization of some of the differentially expressed genes.

Moreover, we observed that clusters in GBM1 sample were organized in waves. Differentially expressed genes were extracted for each spatial cluster and used to make a functional analysis. A low number of active cells in clusters 3 and 5 expressed Myc targets V1, supporting metabolic changes and cell survival. TNFa signaling via NF-kB pathway, related to tumor progression and invasion, was enriched in cluster 2. In the adjacent cluster

4, a hypoxic pathway was the most prominent. Furthermore, epithelial-mesenchymal transition (EMT) was characteristic in cluster 1 and oxidative phosphorylation (OXPHOS) in cluster 0. This cluster distribution suggested evolution from the necrotic zone on the right, through the hypoxic and invasive zone, to the region with higher oxygen concentration.

It was demonstrated that hypoxia induces changes in metabolism and activation of the glycolytic pathway, which supports abnormal cell proliferation. Moreover, it was considered that glycolysis was the predominant metabolic process in tumors, and that OXPHOS was downregulated in cancers (Warburg effect). Even though glycolysis (both aerobic and anaerobic) has an important role in generating metabolites needed for tumor growth, it was shown that OXPHOS remains the primary source of ATP, and that mitochondrial metabolism is involved in different processes supporting tumor progression.

To confirm the differences in metabolism between clusters, we examined genes associated with the tricarboxylic acid (TCA) cycle and glycolysis. As shown in Figure 7.13, we observed that TCA cycle was mostly activated in clusters 0 and 1, confirming OXPHOS and EMT, since TCA is related to both processes[384]. On the other hand, glycolysis was enhanced in hypoxic cluster 4, as expected.

7.2 Conclusions

Spatial transcriptomics is a powerful technique that allows detailed study of the gene expression and its correlation with the tissue structure. Here we had tissues with homogeneous morphology. However, gene expression analysis of those samples revealed different transcriptomic clusters, suggesting high tumoral heterogeneity. We could visualize the expression of genes of interest, hence GBM molecular subtypes and processes relevant for the tumor progression. For example, we detected different molecular subtypes within the same tissue and their spatial distribution. Moreover, we observed that the pathway enrichment depended on the distance from the necrotic core, and that glycolysis was the principal metabolic process in the adjacent hypoxic zone. The more detailed analysis could reveal the presence of different cell types, such as immune system components, important for tumor progression and potential therapy. Furthermore, the detailed comparison of GBM tissues from different patients could reveal their similarities and differences, potentially marking the common targets within the huge heterogeneity.

Some general results were presented here to explain the technique and highlight its potential. Unfortunately, because of the temporal limitations and the quantity of the data obtained, a more detailed study could not be finished in the framework of this thesis and remains a future task.

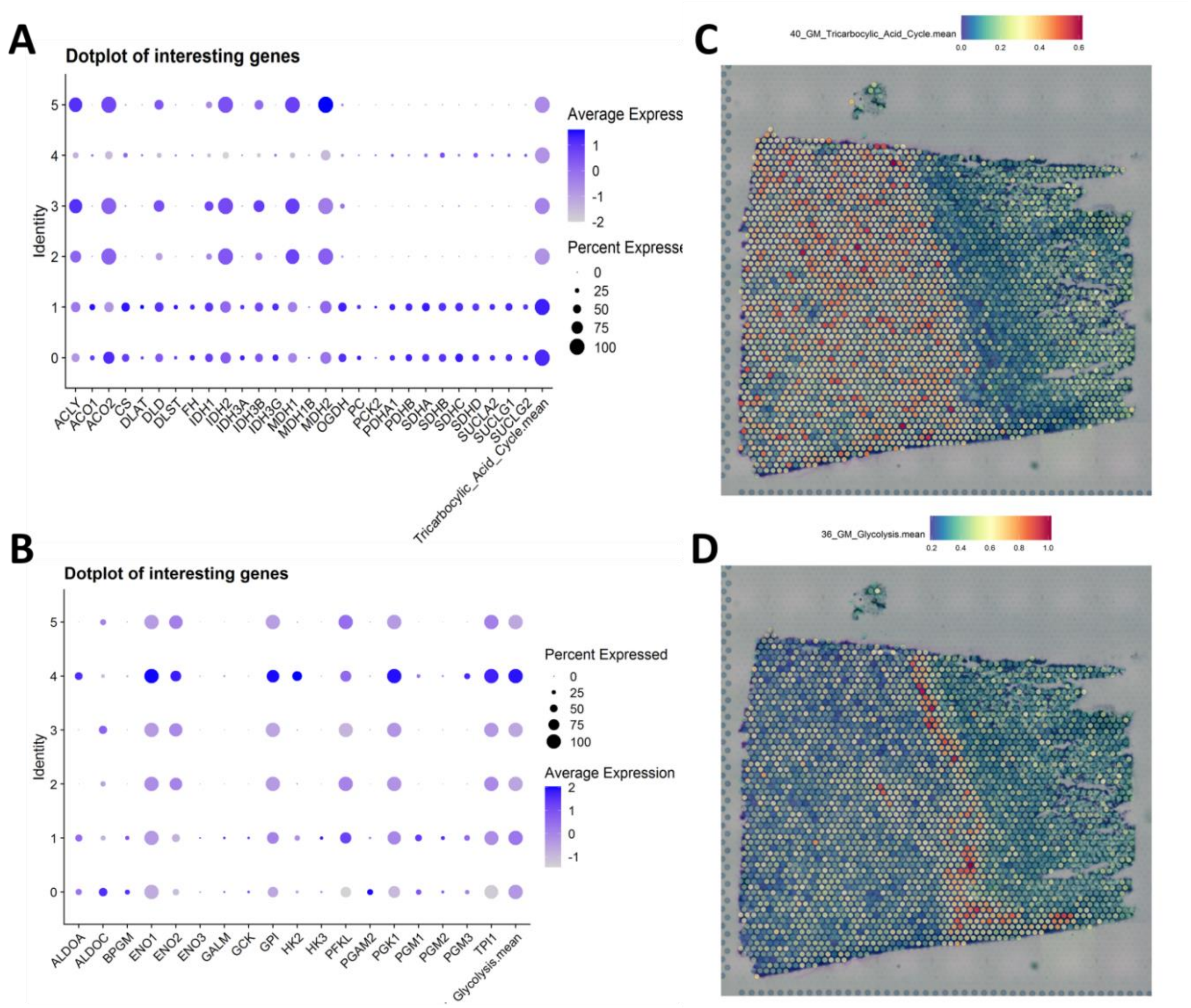

Figure 7.13 Detection of gene expression related to glucose metabolism.
Tricarboxylic acid cycle (A) and glycolysis (B) related genes were studied in clusters of GBM1 and presented as dot plots. Mean of the expression is also presented spatially (C, D).

8 Conclusions and future work

8.1 Conclusions

Throughout this work, the role of the microenvironment in GBM progression has been studied using different methods. This chapter summarizes the most important conclusions made during this PhD dissertation.

- 3D in vitro models in combination with microfluidics allow the incorporation of different components of the complex microenvironment and their physiological recreation. Hence, this system represents a powerful tool for a more precise recreation of the tumor architecture.
- Hypoxia is a trigger for GBM progression in our microfluidic devices. It promotes necrotic core formation in the regions with the lowest oxygen concentration, and activates apoptosis in the surrounding regions, which has also been described in the patient tissue. Moreover, in our biomimetic in vitro models, we have observed that hypoxia protects the tumor from the effects of temozolomide.
- The heterogeneity and plasticity of GBM cells are huge. We have been able to recreate the GBM drug resistance process in vitro using a 3D model based on spheroids treated with the currently clinically used TMZ scheme. Regardless of receiving the same treatment, a population of spheroids reactivated proliferation and growth and had different morphological and transcriptomic characteristics.
- Spatial transcriptomics allows the detailed study of precious patient tissue and the correlation of gene expression data with tumor morphology. In our study, this technique confirmed the high heterogeneity of GBM. The location of the gene expression should be considered to understand better the role of those genes in tumor progression and tumor heterogeneity
- A more multidisciplinary approach should be considered to study the tumor microenvironment in order to integrate and correlate all the cell functional aspects with their microenvironment.

8.2 Future work

This thesis has laid the basis for future studies about the GBM microenvironment using in vitro and ex vivo models. Some of them are elaborated below.

- Incorporate different components of GBM TME into the microfluidic platform, such as immune system cells, vasculature, and a more physiological extracellular matrix (hyaluronic acid).
- Characterize better evolution of cultures within microfluidic devices with different gas permeability. Measure oxygen concentration using integrated sensors or nanoparticles and use the downstream techniques optimized in this thesis to study the different behavior of these cultures.
- As our device allowed the physiologic-like evolution of GBM, it could be used for drug testing. Moreover, oxygen-based nanocarriers have been developed recently to enhance the oxygenation of solid hypoxic tumors and the treatment effectivity[385,386], which could be tested in our devices.
- Study further the upregulated genes in the resistant spheroid population and search for the potential combination treatment. For example, MYC was overexpressed in resistant spheroids, so it could be a potential therapeutic target.
- Validate the spheroid model by comparing results with primary and recurrent GBM samples.
- Continue data processing of results obtained from spatial transcriptomics experiments to characterize better the GBM TME. Compare the studied tumor samples searching for some common targets or relate them with other environmental aspects. Combine this technique with other omics techniques (MALDI imaging) to get the most information possible.

9 *Conclusiones y trabajo futuro*

9.1 Conclusiones

A lo largo de este trabajo, se ha estudiado el papel del microentorno en la progresión del GBM utilizando diferentes métodos. En este capítulo se resumen las conclusiones más importantes de esta tesis doctoral.

- Los modelos 3D in vitro, en combinación con la microfluídica, permiten la incorporación de diferentes componentes del complejo microentorno tumoral y su recreación fisiológica. Por lo tanto, este sistema representa una poderosa herramienta para una simulación más precisa de la arquitectura tumoral.
- La hipoxia es un desencadenante de la progresión de GBM en nuestros dispositivos microfluídicos. Promueve la formación de núcleos necróticos en las regiones con menor concentración de oxígeno y activa la apoptosis en las regiones circundantes, lo que también se ha descrito en el tejido del paciente. Además, en nuestros modelos biomiméticos in vitro hemos observado que la hipoxia protege al tumor de los efectos de la temozolomida.
- La heterogeneidad y plasticidad de las células de GBM son enormes. Hemos podido recrear el proceso de resistencia a fármacos de GBM in vitro, utilizando un modelo 3D basado en esferoides tratados con TMZ, utilizando el esquema clínico actualmente en uso. Independientemente de haber recibido el mismo tratamiento, una población de esferoides reactivó la proliferación y el crecimiento y presentó características morfológicas y transcriptómicas diferentes.
- La transcriptómica espacial permite el estudio detallado del valioso tejido del paciente y la correlación de los datos de expresión génica con la morfología del tumor. En nuestro estudio se confirmó la alta heterogeneidad del GBM con esta técnica. Se debe considerar la ubicación de la expresión génica para comprender mejor el papel de esos genes en la progresión tumoral y la heterogeneidad tumoral.
- De igual modo, un enfoque más multidisciplinario debería tenerse en cuenta para estudiar el microentorno tumoral, con el fin de integrar y correlacionar todos los aspectos funcionales de la célula con su microentorno.

9.2 Trabajo futuro

Esta tesis ha sentado las bases para futuros estudios sobre el microentorno de GBM utilizando modelos in vitro y ex vivo. Algunas de ellas se desarrollan a continuación.

- Incorporar diferentes componentes del microentorno del GBM en plataformas microfluídicas, como células del sistema inmunitario, vascularización y una matriz extracelular más fisiológica (ácido hialurónico).
- Caracterizar mejor la evolución de los cultivos dentro de los dispositivos microfluídicos con diferente permeabilidad a los gases. Medir la concentración de oxígeno utilizando sensores integrados o nanopartículas, y utilizar las técnicas optimizadas en esta tesis para estudiar el comportamiento diferente de estos cultivos.
- Como nuestro dispositivo permitió una evolución similar a la fisiológica del GBM, podría usarse para hacer pruebas de tratamiento. Además, recientemente se han desarrollado varias nanoparticulas para mejorar la oxigenación de tumores sólidos hipóxicos y la efectividad del tratamiento, lo que podría probarse también en nuestros dispositivos.
- Estudiar más en profundidad los genes sobreexpresados en la población de esferoides resistentes y buscar el posible tratamiento combinado. A la vista de los resultados obtenidos, el gen MYC (sobreexpresado en los esferoides resistentes) podría ser una potencial nueva diana terapéutica.
- Validar el modelo de esferoide comparando los resultados con muestras de GBM primarias y recurrentes.
- Continuar el procesamiento de datos obtenidos de los experimentos de transcriptómica espacial para caracterizar mejor el microentorno del GBM. Comparar las muestras tumorales estudiadas buscando dianas comunes o relacionarlas con otros aspectos ambientales. Combinar esta técnica con otras técnicas ómicas (MALDI imaging) para obtener la mayor cantidad de información posible.

10 Thesis contributions

Journal publications.

1. Stanković T*, **Ranđelović T***, Dragoj M, Stojković Burić S, Fernández L, Ochoa I, Pérez-García VM, Pešić M. In vitro biomimetic models for glioblastoma – a promising tool for drug response studies. Drug Resist. Updat. 2021 Mar; 55:100753. doi: 10.1016/j.drup.2021.100753. Epub 2021 Feb 20. PMID: 33667959.
   *Authors contributed equally.
2. Ayensa-Jiménez J, Pérez-Aliacar M, Randelovic T, Sanz-Herrera JA, Doweidar MH, Doblaré M. Analysis of the Parametric Correlation in Mathematical Modeling of In Vitro Glioblastoma Evolution Using Copulas. Mathematics. 2021; 9(1):27. https://doi.org/10.3390/math9010027
3. Ayensa-Jimenez J, Pérez-Aliacar M, Randelovic T, Olivan S, Fernandez L, Sanz-Herrera JA, Ochoa I, H Doweidar M, Doblare M. Mathematical formulation and parametric analysis of in vitro cell models in microfluidic devices. Application to different stages of glioblastoma evolution. Sci Rep. 10, 21193 (2020). https://doi.org/10.1038/s41598-020-78215-3
4. Lacalle D, Castro-Abril HA, Randelovic T, Dominguez C, Heras J, Mata E, Mata G, Mendez Y, Pascual V, Ochoa I. SpheroidJ: An Open-Source Set of Tools for Spheroid Segmentation. Comput Methods Program Biomed. 2020, 105837, doi: 10.1016/j.cmpb.2020.105837
5. Benítez-Mateos AI, Moreno-de Redrojo L, Randelovic T, López-Gallego F. Micro-compartmentalized cell-free protein synthesis in hydrogel μ-channels. ACS Synth. Biol. 2020, 9, 11, 2971–2978
6. Virumbrales-Muñoz M, Ayuso JM, Lacueva A, Randelovic T, Livingston MK, Beebe DJ, Oliván S, Pereboom D, Doblare M, Fernández L, Ochoa I. Enabling cell recovery from 3D cell culture microfluidic devices for tumour microenvironment biomarker profiling. Sci Rep. 2019 Apr 17;9(1):6199. doi: 10.1038/s41598-019-42529-8. Erratum in: Sci Rep. 2020 Jan 15;10(1):757. PMID: 30996291; PMCID: PMC6470149.

Book chapter

Ayensa-Jimenez J, Doweidar M, Randelovic T, Fernandez L, Olivan S, Ochoa I, Doblare M. On the simulation of organ-on-chip cell processes: Application to an in vitro model of glioblastoma evolution. Advances in Biomechanics and Tissue Regeneration. pp. 313 - 342. Elsevier, 2019.

Manuscripts under revision or under preparation

1. Carrasco-Mantis A, Castro-Abril H, Randelovic T, Ochoa I, Doblare M, Sanz-Herrera J.A. A mechanobiological model for tumor spheroids evolution: application to glioblastoma. *Manuscript under major revision in Computer Methods and Programs in Biomedicine*
2. Gonzalez-Lana S, Randelovic T, Monge R, Ciriza J, Ochoa I, Sanchez-Somolinos C. Surface functionalization to control biomimetic mechanical environment in COP-based microfluidic devices. *Manuscript in preparation for Lab-on-a-chip*
3. **Ranđelović T**, Lacueva A, Marques Larraz V, Marquina I, Ochoa I. Heterogeneous response to TMZ treatment in 3D spheroid models – chemoresistance development. *Manuscript in preparation for Cancers*
4. **Ranđelović T**, Vazquez E, Marques Larraz V, Benguria A, Claramonte de la Viuda M, Andrés Sanz JA, Dopazo A, Marquina I, Sanz-Pamplona R, Ochoa I. Spatial transcriptomics as a powerful tool for studying glioblastoma heterogeneity. *Manuscript in preparation for Acta Neuropathologica*

Conference proceedings

1. **Randelovic T**, Marquina I, Alfaro J, Fernandez L, Olivan S, Ochoa I. Glioblastoma on chip – the role of microenvironment in tumor progression and drug resistance development, EUROBIOTECH, Krakow, Poland, 23-25/09/2019. Oral presentation
2. **Randelovic T**. Cell culture2.0: Novel in vitro models based on biomimetic microfluidic chips to simulate the tumour microenvironment. Workshop NanoOncologia, Zaragoza, Spain, 16/01/2018. Oral presentation.
3. **Randelovic T**, Bayona C, Olaizola Rodrigo C, Ochoa I. Deciphering the role of oxygen in glioblastoma progression inside organ on chip models. EUROoCS conference 2021, 1-2/07/2021. Poster.
4. Ayensa-Jiménez J*, **Randelovic T***, Pérez M, Doweidar M, Ochoa I, Doblaré M, Fernández L. Glioblastoma on chip – combination of in vitro and in silico models in the race for a good preclinical model. EUROoCS conference 2020, 8-9/07/2020. Poster.

11 References

1. Louis, D. N. *et al.* The 2016 World Health Organization Classification of Tumors of the Central Nervous System: a summary. *Acta Neuropathol.* **131**, 803–820 (2016).
2. Moore, K. & Kim, L. Primary Brain Tumors: Characteristics, Practical Diagnostic and Treatment Approaches. in *Glioblastoma: Molecular Mechanisms of Pathogenesis and Current Therapeutic Strategies* (ed. Ray, S. K.) 43–75 (Springer New York, 2010). doi:10.1007/978-1-4419-0410-2_2
3. Ostrom, Q. T. *et al.* CBTRUS Statistical Report: Primary Brain and Other Central Nervous System Tumors Diagnosed in the United States in 2012-2016. *Neuro. Oncol.* **21**, V1–V100 (2019).
4. Wesseling, P. & Capper, D. WHO 2016 Classification of gliomas. *Neuropathol. Appl. Neurobiol.* **44**, 139–150 (2018).
5. Wen, P. Y. *et al.* Glioblastoma in adults: a Society for Neuro-Oncology (SNO) and European Society of Neuro-Oncology (EANO) consensus review on current management and future directions. *Neuro. Oncol.* **22**, 1073–1113 (2020).
6. Stupp, R. *et al.* Radiotherapy plus Concomitant and Adjuvant Temozolomide for Glioblastoma. *N. Engl. J. Med.* **352**, 987–996 (2005).
7. Mrugala, M. M. Advances and Challenges in the Treatment of Glioblastoma: A Clinician’s Perspective. *Discov. Med.* **15**, 221–230 (2013).
8. Mrugala, M. M., Ruzevick, J., Zlomanczuk, P. & Lukas, R. V. Tumor Treating Fields in Neuro-Oncological Practice. *Current Oncology Reports* **19**, 1–8 (2017).
9. Tataranu, L. G. *et al.* Current Trends in Glioblastoma Treatment. in *Brain Tumors - An Update* (eds. Agrawal, A. & Moscote-Salazar, L. R.) (InTech, 2018). doi:10.5772/intechopen.75049
10. Bernstein, J. J. & Woodard, C. A. Glioblastoma cells do not intravasate into blood vessels. *Neurosurgery* **36**, 124–132 (1995).
11. Liu, C. J., Shamsan, G. A., Akkin, T. & Odde, D. J. Glioma Cell Migration Dynamics in Brain Tissue Assessed by Multimodal Optical Imaging. *Biophysj* **117**, 1179–1188 (2019).
12. Mair, D. B., Ames, H. M. & Li, R. Mechanisms of invasion and motility of high-grade gliomas in the brain. *Molecular Biology of the Cell* **29**, 2509–2515 (2018).
13. Krol, I. *et al.* Detection of circulating tumour cell clusters in human glioblastoma. *Br. J. Cancer* **119**, 487–491 (2018).
14. Hamilton, J. D. *et al.* Glioblastoma Multiforme Metastasis Outside the CNS: Three Case Reports and Possible Mechanisms of Escape. *J. Clin. Oncol.* **32**, e80–e84

(2014).

15. Giese, A. & Westphal, M. Glioma Invasion in the Central Nervous System. *Neurorurgery* **39**, 235–252 (1996).
16. Böttger, K., Hatzikirou, H., Chauviere, A. & Deutsch, A. Investigation of the migration/proliferation dichotomy and its impact on avascular glioma invasion. *Math. Model. Nat. Phenom.* **7**, 105–135 (2012).
17. Oliveira, A. I. *et al.* Crosstalk between glial and glioblastoma cells triggers the 'go-or-grow' phenotype of tumor cells. *Cell Commun. Signal.* **15**, (2017).
18. Kathagen-Buhmann, A. *et al.* Glycolysis and the pentose phosphate pathway are differentially associated with the dichotomous regulation of glioblastoma cell migration versus proliferation. *Neuro. Oncol.* **18**, 1219–1229 (2016).
19. Tiek, D. M. *et al.* Alterations in Cell Motility, Proliferation, and Metabolism in Novel Models of Acquired Temozolomide Resistant Glioblastoma. *Sci. Rep.* **8**, (2018).
20. Agarwal, S., Sane, R., Oberoi, R., Ohlfest, J. R. & Elmquist, W. F. Delivery of molecularly targeted therapy to malignant glioma, a disease of the whole brain. *Expert reviews in molecular medicine* **13**, e17 (2011).
21. Haumann, R., Videira, J. C., Kaspers, G. J. L., van Vuurden, D. G. & Hulleman, E. Overview of Current Drug Delivery Methods Across the Blood–Brain Barrier for the Treatment of Primary Brain Tumors. *CNS Drugs* **34**, 1121–1131 (2020).
22. Khaddour, K., Johanns, T. M. & Ansstas, G. The landscape of novel therapeutics and challenges in glioblastoma multiforme: Contemporary state and future directions. *Pharmaceuticals* **13**, 1–26 (2020).
23. Dyrna, F., Hanske, S., Krueger, M. & Bechmann, I. The blood-brain barrier. *Journal of Neuroimmune Pharmacology* **8**, 763–773 (2013).
24. Begley, D. ABC Transporters and the Blood-Brain Barrier. *Curr. Pharm. Des.* **10**, 1295–1312 (2004).
25. Li, W. *et al.* Overcoming ABC transporter-mediated multidrug resistance: Molecular mechanisms and novel therapeutic drug strategies. *Drug Resistance Updates* **27**, 14–29 (2016).
26. Wang, J. Q. *et al.* Multidrug resistance proteins (MRPs): Structure, function and the overcoming of cancer multidrug resistance. *Drug Resist. Updat.* **54**, (2021).
27. Bicker, J., Alves, G., Fortuna, A. & Falcão, A. Blood-brain barrier models and their relevance for a successful development of CNS drug delivery systems: A review. *European Journal of Pharmaceutics and Biopharmaceutics* **87**, 409–432 (2014).

28. Zhang, H. *et al.* Chemical molecular-based approach to overcome multidrug resistance in cancer by targeting P-glycoprotein (P-gp). *Medicinal Research Reviews* **41**, 525–555 (2021).
29. He, Q. *et al.* Towards Improvements for Penetrating the Blood–Brain Barrier—Recent Progress from a Material and Pharmaceutical Perspective. *Cells* **7**, 24 (2018).
30. Sharifzad, F. *et al.* Glioblastoma cancer stem cell biology: Potential theranostic targets. *Drug Resist. Updat.* **42**, 35–45 (2019).
31. Aum, D. J. *et al.* Molecular and cellular heterogeneity: the hallmark of glioblastoma. *Neurosurg. Focus* **37**, E11 (2014).
32. Mei, X., Chen, Y. S., Chen, F. R., Xi, S. Y. & Chen, Z. P. Glioblastoma stem cell differentiation into endothelial cells evidenced through live-cell imaging. *Neuro. Oncol.* **19**, 1109–1118 (2017).
33. Suvà, M. L. *et al.* Reconstructing and reprogramming the tumor-propagating potential of glioblastoma stem-like cells. *Cell* **157**, 580–594 (2014).
34. Dirkse, A. *et al.* Stem cell-associated heterogeneity in Glioblastoma results from intrinsic tumor plasticity shaped by the microenvironment. *Nat. Commun.* **10**, 1–16 (2019).
35. Kondo, T. Glioblastoma-initiating cell heterogeneity generated by the cell-of-origin, genetic/epigenetic mutation and microenvironment. *Semin. Cancer Biol.* (2021). doi:10.1016/j.semcancer.2020.12.003
36. Assaraf, Y. G. *et al.* The multi-factorial nature of clinical multidrug resistance in cancer. *Drug Resist. Updat.* **46**, (2019).
37. Gacche, R. N. & Assaraf, Y. G. Redundant angiogenic signaling and tumor drug resistance. *Drug Resist. Updat.* **36**, 47–76 (2018).
38. Gonen, N. & Assaraf, Y. G. Antifolates in cancer therapy: Structure, activity and mechanisms of drug resistance. *Drug Resist. Updat.* **15**, 183–210 (2012).
39. Xu, H. *et al.* A dynamic in vivo-like organotypic blood-brain barrier model to probe metastatic brain tumors. *Sci. Rep.* **6**, (2016).
40. Jiang, W. *et al.* Long non-coding RNAs as a determinant of cancer drug resistance: Towards the overcoming of chemoresistance via modulation of lncRNAs. *Drug Resistance Updates* **50**, (2020).
41. Leonetti, A. *et al.* MicroRNAs as a drug resistance mechanism to targeted therapies in EGFR-mutated NSCLC: Current implications and future directions. *Drug Resist. Updat.* **42**, 1–11 (2019).

42. Lepeltier, E. *et al.* Nanomedicine to target multidrug resistant tumors. *Drug Resistance Updates* **52**, (2020).

43. Mosca, L., Ilari, A., Fazi, F., Assaraf, Y. G. & Colotti, G. Taxanes in cancer treatment: Activity, chemoresistance and its overcoming. *Drug Resist. Updat.* **54**, (2021).

44. Niewerth, D. *et al.* Molecular basis of resistance to proteasome inhibitors in hematological malignancies. *Drug Resist. Updat.* **18**, 18–35 (2015).

45. Wijdeven, R. H., Pang, B., Assaraf, Y. G. & Neefjes, J. Old drugs, novel ways out: Drug resistance toward cytotoxic chemotherapeutics. *Drug Resist. Updat.* **28**, 65–81 (2016).

46. Zhitomirsky, B. & Assaraf, Y. G. Lysosomes as mediators of drug resistance in cancer. *Drug Resist. Updat.* **24**, 23–33 (2016).

47. DeCordova, S. *et al.* Molecular Heterogeneity and Immunosuppressive Microenvironment in Glioblastoma. *Frontiers in Immunology* **11**, (2020).

48. Perrin, S. L. *et al.* Glioblastoma heterogeneity and the tumour microenvironment: Implications for preclinical research and development of new treatments. *Biochemical Society Transactions* **47**, 625–638 (2019).

49. Son, B. *et al.* The role of tumor microenvironment in therapeutic resistance. *Oncotarget* **8**, 3933–3945 (2017).

50. Comba, A. *et al.* Uncovering Spatiotemporal Heterogeneity of High-Grade Gliomas: From Disease Biology to Therapeutic Implications. *Front. Oncol.* **0**, 3040 (2021).

51. Verhaak, R. G. W. *et al.* Integrated Genomic Analysis Identifies Clinically Relevant Subtypes of Glioblastoma Characterized by Abnormalities in PDGFRA, IDH1, EGFR, and NF1. *Cancer Cell* **17**, 98–110 (2010).

52. Zhang, P., Xia, Q., Liu, L., Li, S. & Dong, L. Current Opinion on Molecular Characterization for GBM Classification in Guiding Clinical Diagnosis, Prognosis, and Therapy. *Front. Mol. Biosci.* **0**, 241 (2020).

53. Sottoriva, A. *et al.* Intratumor heterogeneity in human glioblastoma reflects cancer evolutionary dynamics. *Proc. Natl. Acad. Sci. U. S. A.* **110**, 4009 (2013).

54. Prabhu, A., Kesarwani, P., Kant, S., Graham, S. F. & Chinnaiyan, P. Histologically defined intratumoral sequencing uncovers evolutionary cues into conserved molecular events driving gliomagenesis. *Neuro. Oncol.* **19**, 1599–1606 (2017).

55. Puchalski, R. B. *et al.* An anatomic transcriptional atlas of human glioblastoma. *Science* **360**, 660 (2018).

56. Kim, E. L. *et al.* Intratumoral Heterogeneity and Longitudinal Changes in Gene

Expression Predict Differential Drug Sensitivity in Newly Diagnosed and Recurrent Glioblastoma. *Cancers (Basel).* **12**, 520 (2020).

57. Menyhárt, O. & Győrffy, B. Multi-omics approaches in cancer research with applications in tumor subtyping, prognosis, and diagnosis. *Comput. Struct. Biotechnol. J.* **19**, 949–960 (2021).
58. Andrieux, G. & Chakraborty, S. Editorial: Integration of Multi-Omics Techniques in Cancer. *Front. Genet.* **12**, 1447 (2021).
59. Gómez-Oliva, R. *et al.* Evolution of Experimental Models in the Study of Glioblastoma: Toward Finding Efficient Treatments. *Front. Oncol.* **10**, 3245 (2021).
60. Luo, X. & Weiss, W. A. Utility of human-derived models for glioblastoma. *Cancer Discov.* **10**, 907–909 (2020).
61. Pine, A. R. *et al.* Tumor microenvironment is critical for the maintenance of cellular states found in primary glioblastomas. *Cancer Discov.* **10**, 964–979 (2020).
62. Kijima, N. & Kanemura, Y. Mouse Models of Glioblastoma. in *Glioblastoma* 131–139 (Codon Publications, 2017). doi:10.15586/codon.glioblastoma.2017.ch7
63. Borrego-Soto, G., Ortiz-López, R. & Rojas-Martínez, A. Ionizing radiation-induced DNA injury and damage detection in patients with breast cancer. *Genetics and Molecular Biology* **38**, 420–432 (2015).
64. de Almeida, L. C., Calil, F. A., Machado-Neto, J. A. & Costa-Lotufo, L. V. DNA damaging agents and DNA repair: From carcinogenesis to cancer therapy. *Cancer Genetics* **252**–**253**, 6–24 (2021).
65. Huang, R. X. & Zhou, P. K. DNA damage response signaling pathways and targets for radiotherapy sensitization in cancer. *Signal Transduction and Targeted Therapy* **5**, (2020).
66. Woods, D. & Turchi, J. J. Chemotherapy induced DNA damage response Convergence of drugs and pathways. *Cancer Biology and Therapy* **14**, 379–389 (2013).
67. Ali, M. Y. *et al.* Radioresistance in glioblastoma and the development of radiosensitizers. *Cancers* **12**, 1–29 (2020).
68. Bighetti-Trevisan, R. L., Sousa, L. O., Castilho, R. M. & Almeida, L. O. Cancer Stem Cells: Powerful Targets to Improve Current Anticancer Therapeutics. *Stem Cells International* **2019**, (2019).
69. Bao, S. *et al.* Glioma stem cells promote radioresistance by preferential activation of the DNA damage response. *Nature* **444**, 756–760 (2006).

70. Sun, S., Lee, D. & Leung, G. K. K. Chemoresistance in glioma. in *New Advances on Disease Biomarkers and Molecular Targets in Biomedicine* 243–270 (Humana Press Inc., 2013). doi:10.1007/978-1-62703-456-2_14

71. Cahill, D. P. *et al.* Loss of the mismatch repair protein MSH6 in human glioblastomas is associated with tumor progression during temozolomide treatment. *Clin. Cancer Res.* **13**, 2038–2045 (2007).

72. Felsberg, J. *et al.* Promoter methylation and expression of MGMT and the DNA mismatch repair genes MLH1, MSH2, MSH6 and PMS2 in paired primary and recurrent glioblastomas. *Int. J. Cancer* **129**, 659–670 (2011).

73. Montaldi, A. P. & Sakamoto-Hojo, E. T. Methoxyamine sensitizes the resistant glioblastoma T98G cell line to the alkylating agent temozolomide. *Clin. Exp. Med.* **13**, 279–288 (2013).

74. Cui, Q. *et al.* Modulating ROS to overcome multidrug resistance in cancer. *Drug Resist. Updat.* **41**, 1–25 (2018).

75. Yang, H. *et al.* The role of cellular reactive oxygen species in cancer chemotherapy. *Journal of Experimental and Clinical Cancer Research* **37**, 266 (2018).

76. Lee, H. C. *et al.* Increased expression of antioxidant enzymes in radioresistant variant from U251 human glioblastoma cell line. *Int. J. Mol. Med.* **13**, 883–887 (2004).

77. Oliva, C. R., Moellering, D. R., Gillespie, G. Y. & Griguer, C. E. Acquisition of Chemoresistance in Gliomas Is Associated with Increased Mitochondrial Coupling and Decreased ROS Production. *PLoS One* **6**, (2011).

78. Polewski, M. D. *et al.* Increased expression of system x c-in glioblastoma confers an altered metabolism and chemoresistance. *Mol Cancer Res* **14**, 1229–1242 (2016).

79. Hou, X., Jiang, J., Tian, Z. & Wei, L. Autophagy and tumour chemotherapy. in *Advances in Experimental Medicine and Biology* **1207**, 351–374 (Springer, 2020).

80. Knizhnik, A. V. *et al.* Survival and Death Strategies in Glioma Cells: Autophagy, Senescence and Apoptosis Triggered by a Single Type of Temozolomide-Induced DNA Damage. *PLoS One* **8**, e55665 (2013).

81. Pawlowska, E., Szczepanska, J., Szatkowska, M. & Blasiak, J. An Interplay between Senescence, Apoptosis and Autophagy in Glioblastoma Multiforme-Role in Pathogenesis and Therapeutic Perspective. *Int. J. Mol. Sci.* **19**, (2018).

82. Russo, M. & Russo, G. L. Autophagy inducers in cancer. *Biochem. Pharmacol.* **153**, 51–61 (2018).

83. Ruano, Y. *et al.* Identification of survival-related genes of the phosphatidylinositol 3′-

kinase signaling pathway in glioblastoma multiforme. *Cancer* **112**, 1575–1584 (2008).

84. Chen, Y. *et al.* VAMP8 facilitates cellular proliferation and temozolomide resistance in human glioma cells. *Neuro. Oncol.* **17**, 407–418 (2015).
85. Hu, B. *et al.* Fibulin-3 promotes glioma growth and resistance through a novel paracrine regulation of Notch signaling Bin. *Cancer Res* **72**, 3873–3885 (2012).
86. Fanfone, D., Idbaih, A., Mammi, J., Gabut, M. & Ichim, G. Profiling anti-apoptotic bcl-xl protein expression in glioblastoma tumorspheres. *Cancers (Basel).* **12**, 1–14 (2020).
87. Jin, F. *et al.* Comparison between cells and cancer stem-like cells isolated from glioblastoma and astrocytoma on expression of anti-apoptotic and multidrug resistance-associated protein genes. *Neuroscience* **154**, 541–550 (2008).
88. Capper, D. *et al.* Stem-cell-like glioma cells are resistant to TRAIL/Apo2L and exhibit down-regulation of caspase-8 by promoter methylation. *Acta Neuropathol.* **117**, 445–456 (2009).
89. Daniele, S. *et al.* Bax Activation Blocks Self-Renewal and Induces Apoptosis of Human Glioblastoma Stem Cells. *ACS Chem. Neurosci.* **9**, 85–99 (2018).
90. Ma, J. *et al.* Biochemical changes associated with a multidrug-resistant phenotype of a human glioma cell line with temozolomide-acquired resistance. *Biochem. Pharmacol.* **63**, 1219–1228 (2002).
91. Trejo-Solís, C. *et al.* Autophagic and apoptotic pathways as targets for chemotherapy in glioblastoma. *International Journal of Molecular Sciences* **19**, (2018).
92. Valdés-Rives, S. A., Casique-Aguirre, D., Germán-Castelán, L., Velasco-Velázquez, M. A. & González-Arenas, A. Apoptotic Signaling Pathways in Glioblastoma and Therapeutic Implications. *BioMed Research International* **2017**, (2017).
93. Hombach-Klonisch, S. *et al.* Glioblastoma and chemoresistance to alkylating agents: Involvement of apoptosis, autophagy, and unfolded protein response. *Pharmacology and Therapeutics* **184**, 13–41 (2018).
94. Yamada, K. *et al.* Essential gene pathways for glioblastoma stem cells: Clinical implications for prevention of tumor recurrence. *Cancers* **3**, 1975–1995 (2011).
95. Calatozzolo, C. *et al.* Expression of drug resistance proteins Pgp, MRP1, MRP3, MRP5 AND GST-π in human glioma. *J. Neurooncol.* **74**, 113–121 (2005).
96. Garrido, W. *et al.* Chemoresistance in High-Grade Gliomas: Relevance of Adenosine Signalling in Stem-Like Cells of Glioblastoma Multiforme. *Curr. Drug Targets* **15**,

931–942 (2014).

97. Jin, Y. *et al.* ABCG2 is related with the grade of glioma and resistance to mitoxantone, a chemotherapeutic drug for glioma. *J. Cancer Res. Clin. Oncol.* **135**, 1369–1376 (2009).
98. de Trizio, I., Errede, M., d’Amati, A., Girolamo, F. & Virgintino, D. Expression of P-gp in Glioblastoma: What we can Learn from Brain Development. *Curr. Pharm. Des.* **26**, 1428–1437 (2020).
99. Declèves, X., Amiel, A., Delattre, J.-Y. & Scherrmann, J.-M. Role of ABC Transporters in the Chemoresistance of Human Gliomas. *Curr. Cancer Drug Targets* **6**, 433–445 (2006).
100. Brat, D. J. *et al.* Pseudopalisades in Glioblastoma Are Hypoxic, Express Extracellular Matrix Proteases, and Are Formed by an Actively Migrating Cell Population. *Cancer Res.* **64**, 920–927 (2004).
101. Colwell, N. *et al.* Hypoxia in the glioblastoma microenvironment: Shaping the phenotype of cancer stem-like cells. *Neuro. Oncol.* **19**, 887–896 (2017).
102. Heddleston, J. M., Li, Z., McLendon, R. E., Hjelmeland, A. B. & Rich, J. N. The hypoxic microenvironment maintains glioblastoma stem cells and promotes reprogramming towards a cancer stem cell phenotype. *Cell Cycle* **8**, 3274–3284 (2009).
103. Li, Z. *et al.* Hypoxia-inducible factors regulate tumorigenic capacity of glioma stem cells. *Cancer Cell* **15**, 501–13 (2009).
104. Soeda, A. *et al.* Hypoxia promotes expansion of the CD133-positive glioma stem cells through activation of HIF-1alpha. *Oncogene* **28**, 3949–3959 (2009).
105. Kolenda, J. *et al.* Effects of hypoxia on expression of a panel of stem cell and chemoresistance markers in glioblastoma-derived spheroids. *J. Neurooncol.* **103**, 43–58 (2011).
106. Raz, S. *et al.* Severe hypoxia induces complete antifolate resistance in carcinoma cells due to cell cycle arrest. *Cell Death Dis.* **5**, (2014).
107. Chou, C. W. *et al.* Tumor cycling hypoxia induces chemoresistance in glioblastoma multiforme by upregulating the expression and function of ABCB1. *Neuro. Oncol.* **14**, 1227–1238 (2012).
108. Uribe, D. *et al.* Multidrug resistance in glioblastoma stem-like cells: Role of the hypoxic microenvironment and adenosine signaling. *Molecular Aspects of Medicine* **55**, 140–151 (2017).

109. Amberger-Murphy, V. Hypoxia helps glioma to fight therapy. *Curr. Cancer Drug Targets* **9**, 381–390 (2009).

110. Huang, S., Qi, P., Zhang, T., Li, F. & He, X. The HIF‑1α/miR‑224‑3p/ATG5 axis affects cell mobility and chemosensitivity by regulating hypoxia‑induced protective autophagy in glioblastoma and astrocytoma. *Oncol. Rep.* **41**, 1759–1768 (2019).

111. Sanzey, M. *et al.* Comprehensive analysis of glycolytic enzymes as therapeutic targets in the treatment of glioblastoma. *PLoS One* **10**, (2015).

112. Hjelmeland, A. B. *et al.* Acidic stress promotes a glioma stem cell phenotype. *Cell Death Differ.* **18**, 829–840 (2011).

113. Ezhilarasan, R., Mohanam, I. & Govindarajan, Kathiravan Mohanam, S. Glioma cells suppress hypoxia-induced endothelial cell apoptosis and promote angiogenic process. *Int J Oncol* **30**, 701–707 (2007).

114. Tamura, R. *et al.* The role of vascular endothelial growth factor in the hypoxic and immunosuppressive tumor microenvironment: perspectives for therapeutic implications. *Medical Oncology* **37**, (2020).

115. Zhang, M., Ye, G., Li, J. & Wang, Y. Recent advance in molecular angiogenesis in glioblastoma: the challenge and hope for anti-angiogenic therapy. *Brain Tumor Pathol.* **32**, 229–236 (2015).

116. Xu, H. *et al.* Activation of hypoxia signaling induces phenotypic transformation of glioma cells: implications for bevacizumab antiangiogenic therapy. *Oncotarget* **6**, 11882–93 (2015).

117. Zhu, T. S. *et al.* Endothelial cells create a stem cell niche in glioblastoma by providing Notch ligands that nurture self-renewal of cancer stem-like cells. *Cancer Res* **71**, 6061–6072 (2012).

118. Charles, N. *et al.* Perivascular Nitric Oxide Activates Notch Signaling and Promotes Stem-like Character in PDGF-induced Glioma Cells. *Cell Stem Cell* **6**, 141–152 (2010).

119. Fessler, E., Borovski, T. & Medema, J. P. Endothelial cells induce cancer stem cell features in differentiated glioblastoma cells via bFGF. *Mol. Cancer* **14**, 157 (2015).

120. Belousov, A. *et al.* The Extracellular Matrix and Biocompatible Materials in Glioblastoma Treatment. *Front. Bioeng. Biotechnol.* **7**, 341 (2019).

121. Virga, J. *et al.* Differences in extracellular matrix composition and its role in invasion in primary and secondary intracerebral malignancies. *Anticancer Res.* **37**, 4119–4126

(2017).

122. Farace, C. *et al.* Microenvironmental modulation of decorin and lumican in temozolomide-resistant glioblastoma and neuroblastoma cancer stem-like cells. *PLoS One* **10**, 1–18 (2015).

123. Coppola, S. *et al.* A mechanopharmacology approach to overcome chemoresistance in pancreatic cancer. *Drug Resist. Updat.* **31**, 43–51 (2017).

124. Erickson, A. E., Lan Levengood, S. K., Sun, J., Chang, F. C. & Zhang, M. Fabrication and Characterization of Chitosan–Hyaluronic Acid Scaffolds with Varying Stiffness for Glioblastoma Cell Culture. *Adv. Healthc. Mater.* **7**, (2018).

125. Ulrich, T. A., De Juan Pardo, E. M. & Kumar, S. The mechanical rigidity of the extracellular matrix regulates the structure, motility, and proliferation of glioma cells. *Cancer Res.* **69**, 4167–4174 (2009).

126. Freeman, A. E. & Hoffman, R. M. In vivo-like growth of human tumors in vitro. *Proc. Natl. Acad. Sci. U. S. A.* **83**, 2694–2698 (1986).

127. Jung, S. *et al.* Tracking the invasiveness of human astrocytoma cells by using green fluorescent protein in an organotypical brain slice model. *J. Neurosurg.* **94**, 80–89 (2001).

128. Saji Joseph, J., Tebogo Malindisa, S. & Ntwasa, M. Two-Dimensional (2D) and Three-Dimensional (3D) Cell Culturing in Drug Discovery. in *Cell Culture* (ed. Mehanna, R. A.) (IntechOpen, 2019). doi:10.5772/intechopen.81552

129. Bell, H. S., Whittle, I. R., Walker, M., Leaver, H. A. & Wharton, S. B. The development of necrosis and apoptosis in glioma: experimental findings using spheroid culture systems*. *Neuropathol. Appl. Neurobiol.* **27**, 291–304 (2001).

130. Nath, S. & Devi, G. R. Three-dimensional culture systems in cancer research: Focus on tumor spheroid model. *Pharmacol. Ther.* **163**, 94–108 (2016).

131. Weiswald, L. B., Bellet, D. & Dangles-Marie, V. Spherical Cancer Models in Tumor Biology. *Neoplasia (United States)* **17**, 1–15 (2015).

132. Hoarau-Véchot, J., Rafii, A., Touboul, C. & Pasquier, J. Halfway between 2D and animal models: Are 3D cultures the ideal tool to study cancer-microenvironment interactions? *Int. J. Mol. Sci.* **19**, (2018).

133. Lee, J. *et al.* Tumor stem cells derived from glioblastomas cultured in bFGF and EGF more closely mirror the phenotype and genotype of primary tumors than do serum-cultured cell lines. *Cancer Cell* **9**, 391–403 (2006).

134. Lenting, K., Verhaak, R., Mark Ter Laan, ·, Wesseling, P. & Leenders, W. Glioma:

experimental models and reality. *Acta Neuropathol* **3**, 263–282 (2017).

135. Xiao, W., Sohrabi, A. & Seidlits, S. K. Integrating the glioblastoma microenvironment into engineered experimental models. *Futur. Sci. OA* (2017). doi:10.4155/fsoa-2016-0094

136. Bjerkvig, R., Tonnesen, A., Laerum, O. D. & Backlund, E. O. Multicenter tumor spheroids from human gliomas maintained in organ culture. *J. Neurosurg.* **72**, 463–475 (1990).

137. Christensen, K. *et al.* Immunohistochemical expression of stem cell, endothelial cell, and chemosensitivity markers in primary glioma spheroids cultured in serum-containing and serum-free medium. *Neurosurgery* **66**, 933–947 (2010).

138. De Witt Hamer, P. C., Leenstra, S., Van Noorden, C. J. F. & Zwinderman, A. H. Organotypic glioma spheroids for screening of experimental therapies: How many spheroids and sections are required? *Cytom. Part A* **75**, 528–534 (2009).

139. Mahesparan, R. *et al.* Extracellular matrix-induced cell migration from glioblastoma biopsy specimens in vitro. *Acta Neuropathol.* **97**, 231–239 (1999).

140. Andreatta, F. *et al.* The organoid era permits the development of new applications to study glioblastoma. *Cancers* **12**, 1–16 (2020).

141. Klein, E., Hau, A. C., Oudin, A., Golebiewska, A. & Niclou, S. P. Glioblastoma Organoids: Pre-Clinical Applications and Challenges in the Context of Immunotherapy. *Frontiers in Oncology* **10**, (2020).

142. Zhang, C., Jin, M., Zhao, J., Chen, J. & Jin, W. Organoid models of glioblastoma: advances, applications and challenges. *Am. J. Cancer Res.* **10**, 2242–2257 (2020).

143. Lancaster, M. A. & Knoblich, J. A. Organogenesis in a dish: Modeling development and disease using organoid technologies. *Science (80-.).* **345**, 1247125 (2014).

144. Hubert, C. G. *et al.* A three-dimensional organoid culture system derived from human glioblastomas recapitulates the hypoxic gradients and cancer stem cell heterogeneity of tumors found in vivo. *Cancer Res.* **76**, 2465–2477 (2016).

145. Jacob, F. *et al.* A Patient-Derived Glioblastoma Organoid Model and Biobank Recapitulates Inter- and Intra-tumoral Heterogeneity. *Cell* **180**, 188-204.e22 (2020).

146. Lv, D., Hu, Z., Lu, L., Lu, H. & Xu, X. Three‑dimensional cell culture: A powerful tool in tumor research and drug discovery (Review). *Oncol. Lett.* **14**, 6999–7010 (2017).

147. Ananthanarayanan, B., Kim, Y. & Sanjay, K. Elucidating the mechanobiology of

malignant brain tumors using a brain matrix-mimetic hyaluronic acid hydrogel platform. *Biomaterials* **32**, 7913–7923 (2011).

148. Cheng, V. *et al.* High-content analysis of tumour cell invasion in three-dimensional spheroid assays. *Oncoscience* **2**, 596–606 (2015).
149. Ulrich, T. A., Jain, A., Tanner, K., MacKay, J. L. & Kumar, S. Probing cellular mechanobiology in three-dimensional culture with collagen-agarose matrices. *Biomaterials* **31**, 1875–1884 (2010).
150. Rao, S. S. *et al.* Glioblastoma Behaviors in Three-Dimensional Collagen- Hyaluronan Composite Hydrogels. *ACS Appl Mater Interfaces* **5**, 9276–9284 (2013).
151. Bayat, N. *et al.* The anti-angiogenic effect of atorvastatin in glioblastoma spheroids tumor cultured in fibrin gel: In 3D in vitro model. *Asian Pacific J. Cancer Prev.* **19**, 2553–2560 (2018).
152. Ahmed, E. M., Bandopadhyay, G., Coyle, B. & Grabowska, A. A HIF-independent, CD133-mediated mechanism of cisplatin resistance in glioblastoma cells. *Cell. Oncol.* **41**, 319–328 (2018).
153. Musah-Eroje, A. & Watson, S. A novel 3D in vitro model of glioblastoma reveals resistance to temozolomide which was potentiated by hypoxia. *J. Neurooncol.* **142**, 231–240 (2019).
154. Koh, I. *et al.* The mode and dynamics of glioblastoma cell invasion into a decellularized tissue-derived extracellular matrix-based three-dimensional tumor model. *Sci. Rep.* **8**, 4608 (2018).
155. Benson, K., Galla, H. J. & Kehr, N. S. Cell adhesion behavior in 3D hydrogel scaffolds functionalized with D - Or L -aminoacids. *Macromol. Biosci.* **14**, 793–798 (2014).
156. Kievit, F. M. *et al.* Chitosan-alginate 3D scaffolds as a mimic of the glioma tumor microenvironment. *Biomaterials* **31**, 5903–5910 (2010).
157. Zustiak, S. P. *et al.* Three-dimensional matrix stiffness and adhesive ligands affect cancer cell response to toxins. *Biotechnol. Bioeng.* **113**, 443–452 (2016).
158. Wang, C., Tong, X. & Yang, F. Bioengineered 3D Brain Tumor Model To Elucidate the Effects of Matrix Stiffness on Glioblastoma Cell Behavior Using PEG-Based Hydrogels. *Mol. Pharm.* **11**, 2115−2125 (2014).
159. Pedron, S., Becka, E. & Harley, B. A. C. Regulation of glioma cell phenotype in 3D matrices by hyaluronic acid. *Biomaterials* **34**, 7408–7417 (2013).
160. Gomez-Roman, N., Stevenson, K., Gilmour, L., Hamilton, G. & Chalmers, A. J. A

novel 3D human glioblastoma cell culture system for modeling drug and radiation responses. *Neuro. Oncol.* **19**, 229–241 (2016).

161. Rao, S. S. *et al.* Mimicking white matter tract topography using core-shell electrospun nanofibers to examine migration of malignant brain tumors. *Biomaterials* **34**, 5181–5190 (2013).
162. Ma, L. *et al.* The comparison genomics analysis with glioblastoma multiforme (GBM) cells under 3D and 2D cell culture conditions. *Colloids Surfaces B Biointerfaces* **172**, 665–673 (2018).
163. Li, Q. *et al.* Scalable Production of Glioblastoma Tumor-initiating Cells in 3 Dimension Thermoreversible Hydrogels. *Sci. Rep.* **6**, 31915 (2016).
164. Jia, W., Lu, R., Martin, T. A. & Jiang, W. G. The role of claudin-5 in blood-brain barrier (BBB) and brain metastases (Review). *Mol. Med. Rep.* **9**, 779–785 (2014).
165. Wang, C., Tong, X., Jiang, X. & Yang, F. Effect of Matrix Metalloproteinase-Mediated Matrix Degradation on Glioblastoma Cell Behavior in 3D PEG-based Hydrogels. *J. Biomed. Mater. Res. Part A* (2016). doi:10.1002/jbm.a.35947
166. Martínez-Ramos, C. & Lebourg, M. Three-dimensional constructs using hyaluronan cell carrier as a tool for the study of cancer stem cells. *J. Biomed. Mater. Res. - Part B Appl. Biomater.* **103**, 1249–1257 (2015).
167. Cha, J. & Kim, P. Biomimetic Strategies for the Glioblastoma Microenvironment. *Front. Mater.* **4**, 45 (2017).
168. Caliari, S. R. & Burdick, J. A. A Practical Guide to Hydrogels for Cell Culture. *Nat. Methods* **13**, 405 (2016).
169. Johnson, J. *et al.* Quantitative analysis of complex glioma cell migration on electrospun polycaprolactone using time-lapse microscopy. *Tissue Eng. - Part C Methods* **15**, 531–540 (2009).
170. Unal, S. *et al.* Polycaprolactone/gelatin/hyaluronic acid electrospun scaffolds to mimic glioblastoma extracellular matrix. *Materials (Basel).* **13**, (2020).
171. Sharma, P., Sheets, K., Elankumaran, S. & Nain, A. S. The mechanistic influence of aligned nanofibers on cell shape, migration and blebbing dynamics of glioma cells. *Integr. Biol.* **5**, 1036–1044 (2013).
172. Saleh, A. *et al.* A novel 3D nanofibre scaffold conserves the plasticity of glioblastoma stem cell invasion by regulating galectin-3 and integrin-β1 expression. *Sci. Rep.* **9**, 1–14 (2019).
173. Shafiee, A. & Atala, A. Printing Technologies for Medical Applications. *Trends Mol.*

Med. **22**, 254–265 (2016).

174. Zhang, Y. S. *et al.* Bioprinting the Cancer Microenvironment. *ACS Biomater. Sci. Eng.* **2**, 1710–1721 (2016).
175. Dai, X., Ma, C., Lan, Q. & Xu, T. 3D bioprinted glioma stem cells for brain tumor model and applications of drug susceptibility. *Biofabrication* **8**, 045005 (2016).
176. Heinrich, M. A. *et al.* 3D-Bioprinted Mini-Brain: A Glioblastoma Model to Study Cellular Interactions and Therapeutics. *Adv. Mater.* **31**, 1806590 (2019).
177. Hermida, M. A. *et al.* Three dimensional in vitro models of cancer: Bioprinting multilineage glioblastoma models. *Adv. Biol. Regul.* **75**, 100658 (2020).
178. Lee, C., Abelseth, E., de la Vega, L. & Willerth, S. M. Bioprinting a novel glioblastoma tumor model using a fibrin-based bioink for drug screening. *Mater. Today Chem.* **12**, 78–84 (2019).
179. Maloney, E. *et al.* Immersion bioprinting of tumor organoids in multi-well plates for increasing chemotherapy screening throughput. *Micromachines* **11**, (2020).
180. Smits, I. P. M., Blaschuk, O. W. & Willerth, S. M. Novel N-cadherin antagonist causes glioblastoma cell death in a 3D bioprinted co-culture model. *Biochem. Biophys. Res. Commun.* **529**, 162–168 (2020).
181. Tang, M. *et al.* Three-dimensional bioprinted glioblastoma microenvironments model cellular dependencies and immune interactions. *Cell Res.* 1–21 (2020). doi:10.1038/s41422-020-0338-1
182. Wang, X. *et al.* 3D bioprinted glioma cell-laden scaffolds enriching glioma stem cells via epithelial–mesenchymal transition. *J. Biomed. Mater. Res. - Part A* **107**, 383–391 (2019).
183. Wang, X. *et al.* 3D bioprinted glioma microenvironment for glioma vascularization. *J. Biomed. Mater. Res. Part A* jbm.a.37082 (2020). doi:10.1002/jbm.a.37082
184. Yi, H. *et al.* A bioprinted human-glioblastoma-on-a-chip for the identification of patient-specific responses. *Nat. Biomed. Eng.* **3**, 509–519 (2019).
185. Hoyle, H. W., Smith, L. A., Williams, R. J. & Przyborski, S. A. Applications of novel bioreactor technology to enhance the viability and function of cultured cells and tissues. *Interface Focus* **10**, (2020).
186. Martin, I., Wendt, D. & Heberer, M. The role of bioreactors in tissue engineering. *Trends in Biotechnology* **22**, 80–86 (2004).
187. Selden, C. & Fuller, B. Role of bioreactor technology in tissue engineering for clinical use and therapeutic target design. *Bioengineering* **5**, (2018).

188. Wang, B., Wang, Z., Chen, T. & Zhao, X. Development of Novel Bioreactor Control Systems Based on Smart Sensors and Actuators. *Frontiers in Bioengineering and Biotechnology* **8**, (2020).

189. Bregenzer, M. E. *et al.* Integrated cancer tissue engineering models for precision medicine. *PLoS One* **14**, (2019).

190. Guller, A. E., Grebenyuk, P. N., Shekhter, A. B., Zvyagin, A. V & Deyev, S. M. Bioreactor-Based Tumor Tissue Engineering. *Acta Naturae* **8**, 44–58 (2016).

191. Serra, M., Brito, C., Correia, C. & Alves, P. M. Process engineering of human pluripotent stem cells for clinical application. *Trends in Biotechnology* **30**, 350–359 (2012).

192. Ahmed, S., Chauhan, V. M., Ghaemmaghami, A. M. & Aylott, J. W. New generation of bioreactors that advance extracellular matrix modelling and tissue engineering. *Biotechnol. Lett.* **41**, 1–25 (2019).

193. Li, Q. *et al.* Scalable Culturing of Primary Human Glioblastoma Tumor-Initiating Cells with a Cell-Friendly Culture System. *Sci. Rep.* **8**, (2018).

194. Whitesides, G. M. The origins and the future of microfluidics. *Nature* **442**, 368–373 (2006).

195. Ayuso, J. M. *et al.* Development and characterization of a microfluidic model of the tumour microenvironment. *Sci. Rep.* **6**, 36086 (2016).

196. Paguirigan, A. L. & Beebe, D. J. Microfluidics meet cell biology: bridging the gap by validation and application of microscale techniques for cell biological assays. *Bioessays* **30**, 811–21 (2008).

197. Han, J. *et al.* Rapid emergence and mechanisms of resistance by U87 glioblastoma cells to doxorubicin in an in vitro tumor microfluidic ecology. *Proc. Natl. Acad. Sci. U. S. A.* **113**, 14283–14288 (2016).

198. Huang, Y., Agrawal, B., Clark, P. a, Williams, J. C. & Kuo, J. S. Evaluation of cancer stem cell migration using compartmentalizing microfluidic devices and live cell imaging. *J. Vis. Exp.* e3297 (2011). doi:10.3791/3297

199. Jo, Y., Choi, N., Kim, H. N. & Choi, J. Probing characteristics of cancer cells cultured on engineered platforms simulating different microenvironments. *Artif. Cells, Nanomedicine, Biotechnol.* **46**, 1170–1179 (2018).

200. Liu, W. *et al.* Assay of glioma cell responses to an anticancer drug in a cell-based microfluidic device. *Microfluid. Nanofluidics* **9**, 717–725 (2010).

201. Rezk, R. *et al.* Spatial heterogeneity of cell-matrix adhesive forces predicts human

glioblastoma migration. *Neuro-Oncology Adv.* **2**, 1–11 (2020).

202. Vadivelu, R., Kamble, H., Shiddiky, M. & Nguyen, N.-T. Microfluidic Technology for the Generation of Cell Spheroids and Their Applications. *Micromachines* **8**, 94 (2017).
203. Ayuso, J. M. *et al.* Glioblastoma on a microfluidic chip: Generating pseudopalisades and enhancing aggressiveness through blood vessel obstruction events. *Neuro. Oncol.* **19**, 503–513 (2017).
204. Lee, K. H. K. H. *et al.* Integration of microfluidic chip with biomimetic hydrogel for 3D controlling and monitoring of cell alignment and migration. *J. Biomed. Mater. Res. - Part A* **102**, 1164–1172 (2014).
205. Qazi, H., Shi, Z.-D. & Tarbell, J. M. Fluid shear stress regulates the invasive potential of glioma cells via modulation of migratory activity and matrix metalloproteinase expression. *PLoS One* **6**, e20348 (2011).
206. Samiei, E., Seyfoori, A., Toyota, B., Ghavami, S. & Akbari, M. Investigating programmed cell death and tumor invasion in a three-dimensional (3d) microfluidic model of glioblastoma. *Int. J. Mol. Sci.* **21**, 3162 (2020).
207. Andrei, L. *et al.* Advanced technological tools to study multidrug resistance in cancer. *Drug Resist. Updat.* 100658 (2019). doi:10.1016/j.drup.2019.100658
208. Logun, M., Zhao, W., Mao, L. & Karumbaiah, L. Microfluidics in Malignant Glioma Research and Precision Medicine. *Adv. Biosyst.* **2**, (2018).
209. Quereda, V. *et al.* A Cytotoxic Three-Dimensional-Spheroid, High-Throughput Assay Using Patient-Derived Glioma Stem Cells. *SLAS Discov.* **23**, 842–849 (2018).
210. Sarkar, S. & Yong, V. W. Inflammatory cytokine modulation of matrix metalloproteinase expression and invasiveness of glioma cells in a 3-dimensional collagen matrix. *J. Neurooncol.* **91**, 157–164 (2009).
211. Merz, C. *et al.* Neutralization of the CD95 ligand by APG101 inhibits invasion of glioma cells in vitro. *Anticancer. Drugs* **26**, 716–727 (2015).
212. Kinsella, P., Clynes, M. & Amberger-Murphy, V. Imatinib and docetaxel in combination can effectively inhibit glioma invasion in an in vitro 3D invasion assay. *J. Neurooncol.* **101**, 189–198 (2011).
213. An, Z., Gluck, C. B., Choy, M. L. & Kaufman, L. J. Suberoylanilide hydroxamic acid limits migration and invasion of glioma cells in two and three dimensional culture. *Cancer Lett.* **292**, 215–227 (2010).
214. Iwasaki, K., Rogers, L. R., Barnett, G. H., Estes, M. L. & Barna, B. P. Effect of

recombinant tumor necrosis factor-α on three-dimensional growth, morphology, and invasiveness of human glioblastoma cells in vitro.pdf. *J. Neurosurg.* **78**, 952–958 (1993).

215. Amiri, A. *et al.* Inhibition of carbonic anhydrase IX in glioblastoma multiforme. *Eur. J. Pharm. Biopharm.* **109**, 81–92 (2016).

216. Yahyanejad, S. *et al.* NOTCH blockade combined with radiation therapy and temozolomide prolongs survival of orthotopic glioblastoma. *Oncotarget* **7**, (2016).

217. Sarisozen, C. *et al.* Nanomedicine based curcumin and doxorubicin combination treatment of glioblastoma with scFv-targeted micelles: In vitro evaluation on 2D and 3D tumor models. *Eur. J. Pharm. Biopharm.* **108**, 54–67 (2016).

218. Zhang, I. *et al.* Pharmacological inhibition of lipid droplet formation enhances the effectiveness of curcumin in glioblastoma. *Eur. J. Pharm. Biopharm.* **100**, 66–76 (2016).

219. Dilnawaz, F. & Sahoo, S. K. Enhanced accumulation of curcumin and temozolomide loaded magnetic nanoparticles executes profound cytotoxic effect in glioblastoma spheroid model. *Eur. J. Pharm. Biopharm.* **85**, 452–462 (2013).

220. Mouhieddine, T. H. *et al.* Metformin and ara-a effectively suppress brain cancer by targeting cancer stem/progenitor cells. *Front. Neurosci.* **9**, (2015).

221. Berthier, S. *et al.* Anticancer properties of sodium selenite in human glioblastoma cell cluster spheroids. *J. Trace Elem. Med. Biol.* **44**, 161–176 (2017).

222. de Kruijff, R. M. *et al.* The therapeutic potential of polymersomes loaded with 225Ac evaluated in 2D and 3D in vitro glioma models. *Eur. J. Pharm. Biopharm.* **127**, 85–91 (2018).

223. Oh, H. C. *et al.* Combined effects of niclosamide and temozolomide against human glioblastoma tumorspheres. *J. Cancer Res. Clin. Oncol.* 1–12 (2020). doi:10.1007/s00432-020-03330-7

224. Shojaei, S. *et al.* Simvastatin increases temozolomide-induced cell death by targeting the fusion of autophagosomes and lysosomes. *FEBS J.* **287**, 1005–1034 (2020).

225. Lee, D. W., Lee, S. Y., Doh, I., Ryu, G. H. & Nam, D. H. High-Dose Compound Heat Map for 3D-Cultured Glioblastoma Multiforme Cells in a Micropillar and Microwell Chip Platform. *Biomed Res. Int.* **2017**, 7218707 (2017).

226. Fan, Y., Nguyen, D. T., Akay, Y., Xu, F. & Akay, M. Engineering a Brain Cancer Chip for High-throughput Drug Screening. *Sci. Rep.* **6**, 25062 (2016).

227. Akay, M. *et al.* Drug Screening of Human GBM Spheroids in Brain Cancer Chip. *Sci.*

Rep. **8**, 15423 (2018).

228. Pang, L. *et al.* Construction of single-cell arrays and assay of cell drug-resistance in an integrated microfluidics. *Lab Chip* (2016). doi:10.1039/C6LC01000H
229. Huang, Y. *et al.* Three-dimensional hydrogel is suitable for targeted investigation of amoeboid migration of glioma cells. *Mol. Med. Rep.* **17**, 250–256 (2018).
230. Jia, W. W. *et al.* Effects of three-dimensional collagen scaffolds on the expression profiles and biological functions of glioma cells. *Int. J. Oncol.* **52**, 1787–1800 (2018).
231. Jiguet Jiglaire, C. *et al.* Ex vivo cultures of glioblastoma in three-dimensional hydrogel maintain the original tumor growth behavior and are suitable for preclinical drug and radiation sensitivity screening. *Exp. Cell Res.* **321**, 99–108 (2014).
232. Kievit, F. M. *et al.* Proliferation and enrichment of CD133+ glioblastoma cancer stem cells on 3D chitosan-alginate scaffolds. *Biomaterials* **35**, 9137–9143 (2014).
233. Wang, K. *et al.* Culture on 3D Chitosan-Hyaluronic Acid Scaffolds Enhances Stem Cell Marker Expression and Drug Resistance in Human Glioblastoma Cancer Stem Cells. *Adv. Healthc. Mater.* (2016). doi:10.1002/adhm.201600684
234. Wang, X. *et al.* Enrichment of glioma stem cell-like cells on 3D porous scaffolds composed of different extracellular matrix. *Biochem. Biophys. Res. Commun.* **498**, 1052–1057 (2018).
235. Fayzullin, A. *et al.* Phenotypic and Expressional Heterogeneity in the Invasive Glioma Cells. *Transl. Oncol.* **12**, 122–133 (2019).
236. Florczyk, S. J. *et al.* Porous chitosan-hyaluronic acid scaffolds as a mimic of glioblastoma microenvironment ECM. *Biomaterials* **34**, 10143–50 (2013).
237. Lv, D. *et al.* A three-dimensional collagen scaffold cell culture system for screening anti-glioma therapeutics. *Oncotarget* **7**, 56904–56914 (2016).
238. Wang, X. *et al.* Bioprinting of glioma stem cells improves their endotheliogenic potential. *Colloids Surfaces B Biointerfaces* **171**, 629–637 (2018).
239. He, W. *et al.* Proteomic comparison of 3D and 2D glioma models reveals increased HLA-E expression in 3D models is associated with resistance to NK cell-mediated cytotoxicity. *J. Proteome Res.* **13**, 2272–2281 (2014).
240. Fernandez-Fuente, G., Mollinedo, P., Grande, L., Vazquez-Barquero, A. & Fernandez-Luna, J. L. Culture dimensionality influences the resistance of glioblastoma stem-like cells to multikinase inhibitors. *Mol. Cancer Ther.* **13**, 1664–72 (2014).
241. Levin, V. A., Panchabhai, S., Shen, L. & Baggerly, K. A. Protein and phosphoprotein

levels in glioma and adenocarcinoma cell lines grown in normoxia and hypoxia in monolayer and three-dimensional cultures. *Proteome Sci.* **10**, 5 (2012).

242. Yang, M. Y. *et al.* An innovative three-dimensional gelatin foam culture system for improved study of glioblastoma stem cell behavior. *J. Biomed. Mater. Res. B. Appl. Biomater.* **103**, 618–628 (2015).
243. Ma, N. K. L. *et al.* Collaboration of 3D context and extracellular matrix in the development of glioma stemness in a 3D model. *Biomaterials* **78**, 62–73 (2016).
244. Pedron, S. & Harley, B. A. C. Impact of the biophysical features of a 3D gelatin microenvironment on glioblastoma malignancy. *J. Biomed. Mater. Res. - Part A* **101**, 3404–3415 (2013).
245. Herrera-Perez, M., Voytik-Harbin, S. & Rickus, J. L. Extracellular matrix properties regulate the migratory response of glioblastoma stem cells in 3D culture. *Tissue Eng. Part A* **21**, 2572–2582 (2015).
246. Kievit, F. M. *et al.* Modeling the tumor microenvironment using chitosan-alginate scaffolds to control the stem-like state of glioblastoma cells. *Biomater. Sci.* **4**, 610–613 (2016).
247. Kaphle, P., Li, Y. & Yao, L. The mechanical and pharmacological regulation of glioblastoma cell migration in 3D matrices. *J. Cell. Physiol.* **234**, 3948–3960 (2019).
248. Heffernan, J. M., Overstreet, D. J., Le, L. D., Vernon, B. L. & Sirianni, R. W. Bioengineered Scaffolds for 3D Analysis of Glioblastoma Proliferation and Invasion. *Ann. Biomed. Eng.* **43**, 1965–1977 (2015).
249. Wang, C. *et al.* Matrix stiffness modulates patient-derived glioblastoma cell fates in 3D hydrogels. *Tissue Eng. Part A* (2020). doi:10.1089/ten.tea.2020.0110
250. Zhu, D., Trinh, P., Li, J., Grant, G. & Yang, F. Gradient hydrogels for screening stiffness effects on patient-derived glioblastoma xenograft cellfates in <scp>3D</scp>. *J. Biomed. Mater. Res. Part A* jbm.a.37093 (2020). doi:10.1002/jbm.a.37093
251. Unal, S. *et al.* Glioblastoma cell adhesion properties through bacterial cellulose nanocrystals in polycaprolactone/gelatin electrospun nanofibers. *Carbohydr. Polym.* **233**, (2020).
252. Grundy, T. J. *et al.* Differential response of patient- derived primary glioblastoma cells to environmental stiffness. *Nat. Publ. Gr.* 4–13 (2016). doi:10.1038/srep23353
253. Panchalingam, K. M. *et al.* Bioprocessing of Human Glioblastoma Brain Cancer Tissue. *Tissue Eng. Part A* **16**, 1169–1177 (2010).

254. Kingsmore, K. M. *et al.* Interstitial flow differentially increases patient-derived glioblastoma stem cell invasion via CXCR4, CXCL12, and CD44-mediated mechanisms. *Integr. Biol. (United Kingdom)* **8**, 1246–1260 (2016).

255. Munson, J. M., Bellamkonda, R. V. & Swartz, M. A. Interstitial flow in a 3d microenvironment increases glioma invasion by a cxcr4-dependent mechanism. *Cancer Res.* **73**, 1536–1546 (2013).

256. Li Petri, G. *et al.* Impact of hypoxia on chemoresistance of mesothelioma mediated by the proton-coupled folate transporter, and preclinical activity of new anti-LDH-A compounds. *Br. J. Cancer* **123**, 644–656 (2020).

257. Ma, J. *et al.* Patterning hypoxic multicellular spheroids in a 3D matrix - a promising method for anti-tumor drug screening. *Biotechnol. J.* **11**, 127–134 (2016).

258. Rosenberg, T., Aaberg-Jessen, C., Petterson, S. A. & Kristensen, B. W. Heterogenic expression of stem cell markers in patient-derived glioblastoma spheroid cultures exposed to long-term hypoxia. *CNS Oncol.* **7**, CNS15 (2018).

259. Avci, N. G., Fan, Y., Dragomir, A., Akay, Y. M. & Akay, M. Investigating the Influence of HUVECs in the Formation of Glioblastoma Spheroids in High-Throughput Three-Dimensional Microwells. *IEEE Trans. Nanobioscience* **14**, 790–796 (2015).

260. Chen, Z. *et al.* In vitro angiogenesis by human umbilical vein endothelial cells (HUVEC) induced by three-dimensional co-culture with glioblastoma cells. *J. Neurooncol.* **92**, 121–128 (2009).

261. Nguyen, D., Fan, Y., Akay, Y. & Akay, M. TNP-470 Reduces Glioblastoma Angiogenesis in Three Dimensional GelMA Microwell Platform. *IEEE Trans. Nanobioscience* **1241**, 1–1 (2016).

262. Nguyen, D. T., Fan, Y., Akay, Y. M. & Akay, M. Investigating Glioblastoma Angiogenesis Using A 3D in Vitro GelMA Microwell Platform. *IEEE Trans. Nanobioscience* **15**, 289–293 (2016).

263. Chonan, Y., Taki, S., Sampetrean, O., Saya, H. & Sudo, R. Endothelium-induced three-dimensional invasion of heterogeneous glioma initiating cells in a microfluidic coculture platform. *Integr. Biol. (United Kingdom)* **9**, 762–773 (2017).

264. Wang, C. *et al.* Mimicking brain tumor-vasculature microanatomical architecture via co-culture of brain tumor and endothelial cells in 3D hydrogels. *Biomaterials* **202**, 35–44 (2019).

265. McCoy, M. G. *et al.* Endothelial cells promote 3D invasion of GBM by IL-8-

dependent induction of cancer stem cell properties. *Sci. Rep.* **9**, 1–14 (2019).

266. Truong, D. *et al.* A three-dimensional (3D) organotypic microfluidic model for glioma stem cells – Vascular interactions. *Biomaterials* **198**, 63–77 (2019).

267. Ngo, M. T. & Harley, B. A. The Influence of Hyaluronic Acid and Glioblastoma Cell Coculture on the Formation of Endothelial Cell Networks in Gelatin Hydrogels. *Adv. Healthc. Mater.* **6**, (2017).

268. Civita, P., Leite, D. M. & Pilkington, G. J. Pre-clinical drug testing in 2d and 3d human in vitro models of glioblastoma incorporating non-neoplastic astrocytes: Tunneling nano tubules and mitochondrial transfer modulates cell behavior and therapeutic respons. *Int. J. Mol. Sci.* **20**, (2019).

269. Grodecki, J. *et al.* Glioma-astrocyte interactions on white matter tract-mimetic aligned electrospun nanofibers. *Biotechnol. Prog.* **31**, 1406–1415 (2015).

270. Gritsenko, P., Leenders, W. & Friedl, P. Recapitulating in vivo-like plasticity of glioma cell invasion along blood vessels and in astrocyte-rich stroma. *Histochem. Cell Biol.* **148**, 395–406 (2017).

271. Marisol Herrera-Perez, R. *et al.* Presence of stromal cells in a bioengineered tumor microenvironment alters glioblastoma migration and response to STAT3 inhibition. *PLoS One* **13**, (2018).

272. Oliveira Rodini, C., Benites Gonçalves da Silva, P., Faria Assoni, A., Melechco Carvalho, V. & Keith Okamoto, O. Mesenchymal stem cells enhance tumorigenic properties of human glioblastoma through independent cell-cell communication mechanisms. *Oncotarget* **9**, 24766–24777 (2018).

273. Breznik, B., Motaln, H., Vittori, M., Rotter, A. & Turnšek, T. L. Mesenchymal stem cells differentially affect the invasion of distinct glioblastoma cell lines. *Oncotarget* **8**, 25482–25499 (2017).

274. Coniglio, S., Miller, I., Symons, M. & Segall, J. E. Coculture assays to study macrophage and microglia stimulation of glioblastoma invasion. *J. Vis. Exp.* **116**, 53990 (2016).

275. Leite, D. M. *et al.* A human co-culture cell model incorporating microglia supports glioblastoma growth and migration, and confers resistance to cytotoxics. *FASEB J.* **34**, 1710–1727 (2020).

276. Cui, X. *et al.* Hacking macrophage-associated immunosuppression for regulating glioblastoma angiogenesis. *Biomaterials* **161**, 164–178 (2018).

277. Ravi, M., Ramesh, A. & Pattabhi, A. Human Brain Malignant Glioma (BMG-1) 3D

Aggregate Morphology and Screening for Cytotoxicity and Anti-Proliferative Effects. *J. Cell. Physiol.* **232**, 685–690 (2017).

278. Kim, J. W., Ho, W. J. & Wu, B. M. The role of the 3D environment in hypoxia-induced drug and apoptosis resistance. *Anticancer Res.* **31**, 3237–3245 (2011).
279. Stojković, S. *et al.* Resistance to DNA Damaging agents produced invasive phenotype of rat glioma cells-characterization of a new in vivo model. *Molecules* **21**, 1–16 (2016).
280. Pedron, S., Hanselman, J. S., Schroeder, M. A., Sarkaria, J. N. & Harley, B. A. C. Extracellular Hyaluronic Acid Influences the Efficacy of EGFR Tyrosine Kinase Inhibitors in a Biomaterial Model of Glioblastoma. *Adv. Healthc. Mater.* **6**, 1–20 (2017).
281. Xiao, W. *et al.* Brain-mimetic 3D culture platforms allow investigation of cooperative effects of extracellular matrix features on therapeutic resistance in glioblastoma. *Cancer Res.* **78**, 1358–1370 (2018).
282. Xiao, W. *et al.* Bioengineered scaffolds for 3D culture demonstrate extracellular matrix-mediated mechanisms of chemotherapy resistance in glioblastoma. *Matrix Biol.* (2019). doi:10.1016/J.MATBIO.2019.04.003
283. Shannon, S. *et al.* Inhibition of glioblastoma dispersal by the MEK inhibitor PD0325901. *BMC Cancer* **17**, (2017).
284. Yang, N. *et al.* A co-culture model with brain tumor-specific bioluminescence demonstrates astrocyte-induced drug resistance in glioblastoma. *J. Transl. Med.* **12**, (2014).
285. Xiao, M. *et al.* A Fully 3D Interconnected Graphene–Carbon Nanotube Web Allows the Study of Glioma Infiltration in Bioengineered 3D Cortex-Like Networks. *Adv. Mater.* **30**, 1806132 (2018).
286. Nešović, M. *et al.* Src Inhibitors Pyrazolo[3,4-d]pyrimidines, Si306 and Pro-Si306, Inhibit Focal Adhesion Kinase and Suppress Human Glioblastoma Invasion In Vitro and In Vivo. *Cancers (Basel).* **12**, 1570 (2020).
287. Morfoisse, F. *et al.* Hypoxia Induces VEGF-C Expression in Metastatic Tumor Cells via a HIF-1α-Independent Translation-Mediated Mechanism. *Cell Rep.* **6**, 155–167 (2014).
288. Vordermark, D., Shibata, T. & Brown, J. M. Green fluorescent protein is a suitable reporter of tumor hypoxia despite an oxygen requirement for chromophore formation. *Neoplasia* **3**, 527–534 (2001).

289. Ayuso, J. M. *et al.* Tumor-on-a-chip: a microfluidic model to study cell response to environmental gradients. *Lab Chip* **19**, 3461 (2019).

290. Hermanson, G. T. Bioconjugate Techniques: Third Edition. *Bioconjugate Tech. Third Ed.* 1–1146 (2013). doi:10.1016/C2009-0-64240-9

291. Ostermann, S. *et al.* Plasma and Cerebrospinal Fluid Population Pharmacokinetics of Temozolomide in Malignant Glioma Patients. *Clin. Cancer Res.* **10**, 3728–3736 (2004).

292. Rieger, A. M., Hall, B. E., Luong, L. T., Schang, L. M. & Barreda, D. R. Conventional apoptosis assays using propidium iodide generate a significant number of false positives that prevent accurate assessment of cell death. *J. Immunol. Methods* **358**, 81–92 (2010).

293. Pietkiewicz, S., Schmidt, J. H. & Lavrik, I. N. Quantification of apoptosis and necroptosis at the single cell level by a combination of Imaging Flow Cytometry with classical Annexin V/propidium iodide staining. *J. Immunol. Methods* **423**, 99–103 (2015).

294. Lacalle, D. *et al.* SpheroidJ: An Open-Source Set of Tools for Spheroid Segmentation. *Comput. Methods Programs Biomed.* **200**, (2021).

295. Atencia, J. & Beebe, D. J. Controlled microfluidic interfaces. *Nat. 2005 4377059* **437**, 648–655 (2004).

296. Convery, N. & Gadegaard, N. 30 years of microfluidics. *Micro Nano Eng.* **2**, 76–91 (2019).

297. Scott, S. M. & Ali, Z. Fabrication Methods for Microfluidic Devices: An Overview. *Micromachines* **12**, (2021).

298. Berthier, E., Young, E. W. K. & Beebe, D. Engineers are from PDMS-land, Biologists are from Polystyrenia. *Lab Chip* **12**, 1224–1237 (2012).

299. Gencturk, E., Mutlu, S. & Ulgen, K. O. Advances in microfluidic devices made from thermoplastics used in cell biology and analyses. *Biomicrofluidics* **11**, 051502 (2017).

300. Ayuso, J. M. *et al.* SU-8 based microdevices to study self-induced chemotaxis in 3D microenvironments. *Front. Mater.* **2**, 37 (2015).

301. Chu, J.-S., Gilchrist, M. D. & Zhang, N. Microinjection Molding for Microfluidics Applications. *Encycl. Microfluid. Nanofluidics* 2085–2101 (2015). doi:10.1007/978-1-4614-5491-5_694

302. Virumbrales-Muñoz, M. & Ayuso, J. M. From microfluidics to microphysiological systems: Past, present, and future. *Organs-on-a-Chip* 100015 (2022).

doi:10.1016/J.OOC.2022.100015

303. Zervantonakis, I. K. *et al.* Three-dimensional microfluidic model for tumor cell intravasation and endothelial barrier function. *Proc. Natl. Acad. Sci. U. S. A.* **109**, 13515–13520 (2012).

304. Li, R. *et al.* Macrophage-secreted TNFα and TGFβ1 Influence Migration Speed and Persistence of Cancer Cells in 3D Tissue Culture via Independent Pathways. *Cancer Res.* **77**, 279 (2017).

305. Chen, M. B. *et al.* On-chip human microvasculature assay for visualization and quantitation of tumor cell extravasation dynamics. *Nat. Protoc.* **12**, 865 (2017).

306. Hajal, C. *et al.* The CCL2-CCR2 astrocyte-cancer cell axis in tumor extravasation at the brain. *Sci. Adv.* **7**, 8139–8162 (2021).

307. Amemiya, T. *et al.* Mesenchymal glioblastoma-induced mature de-novo vessel formation of vascular endothelial cells in a microfluidic device. *Mol. Biol. Rep.* **48**, 395 (2021).

308. Young, E. W. K., Berthier, E. & Beebe, D. J. Assessment of enhanced autofluorescence and impact on cell microscopy for microfabricated thermoplastic devices. *Anal. Chem.* **85**, 44 (2013).

309. Ayensa-Jiménez, J. *et al.* On the Simulation of Organ-on-Chip Cell Processes: Application to an In Vitro Model of Glioblastoma Evolution. *Adv. Biomech. Tissue Regen.* 313–341 (2019). doi:10.1016/B978-0-12-816390-0.00016-9

310. Ayensa-Jiménez, J. *et al.* Mathematical formulation and parametric analysis of in vitro cell models in microfluidic devices: application to different stages of glioblastoma evolution. *Sci. Rep.* **10**, 1–21 (2020).

311. Ayensa-Jiménez, J. *et al.* Analysis of the Parametric Correlation in Mathematical Modeling of In Vitro Glioblastoma Evolution Using Copulas. *Math. 2021, Vol. 9, Page 27* **9**, 27 (2020).

312. Virumbrales-muñoz, M., Ayuso, J. M., Lacueva, A. & Randelovic, T. Enabling cell recovery from 3D cell culture microfluidic devices for tumour microenvironment biomarker profiling. *Sci. Rep.* 1–14 (2019). doi:10.1038/s41598-019-42529-8

313. Braun, F., Bertin-Ciftci, J., Gallouet, A. S., Millour, J. & Juin, P. Serum-Nutrient Starvation Induces Cell Death Mediated by Bax and Puma That Is Counteracted by p21 and Unmasked by Bcl-xL Inhibition. *PLoS One* **6**, e23577 (2011).

314. Winkler, J., Abisoye-Ogunniyan, A., Metcalf, K. J. & Werb, Z. Concepts of extracellular matrix remodelling in tumour progression and metastasis. *Nat. Commun.*

2020 111 **11**, 1–19 (2020).

315. Provenzano, P. P., Inman, D. R., Eliceiri, K. W., Trier, S. M. & Keely, P. J. Contact Guidance Mediated Three-Dimensional Cell Migration is Regulated by Rho/ROCK-Dependent Matrix Reorganization. *Biophys. J.* **95**, 5374 (2008).
316. Payne, L. S. & Huang, P. H. The pathobiology of collagens in glioma. *Mol. Cancer Res.* **11**, 1129–40 (2013).
317. Grinnell, F. Fibroblasts, myofibroblasts, and wound contraction. *J. Cell Biol.* **124**, 401–404 (1994).
318. Pakshir, P. & Hinz, B. The big five in fibrosis: Macrophages, myofibroblasts, matrix, mechanics, and miscommunication. *Matrix Biol.* **68**–**69**, 81–93 (2018).
319. Bell, E., Ivarsson, B. & Merrill, C. Production of a tissue-like structure by contraction of collagen lattices by human fibroblasts of different proliferative potential in vitro. *Proc. Natl. Acad. Sci. U. S. A.* **76**, 1274–1278 (1979).
320. Rhee, S. Fibroblasts in three dimensional matrices: cell migration and matrix remodeling. *Exp. Mol. Med. 2009 4112* **41**, 858–865 (2009).
321. Kim, D. & Herr, A. E. Protein immobilization techniques for microfluidic assays. *Biomicrofluidics* **7**, 041501 (2013).
322. Gokaltun, A., Yarmush, M. L., Asatekin, A. & Usta, O. B. Recent advances in nonbiofouling PDMS surface modification strategies applicable to microfluidic technology. *Technology* **5**, 1 (2017).
323. Pereiro, I., Fomitcheva Khartchenko, A., Petrini, L. & Kaigala, G. V. Nip the bubble in the bud: a guide to avoid gas nucleation in microfluidics. *Lab Chip* **19**, 2296–2314 (2019).
324. Eltzschig, H. K. & Eckle, T. Ischemia and reperfusion—from mechanism to translation. *Nat. Med. 2011 1711* **17**, 1391–1401 (2011).
325. Wu, M. Y. *et al.* Current Mechanistic Concepts in Ischemia and Reperfusion Injury. *Cell. Physiol. Biochem.* **46**, 1650–1667 (2018).
326. Chen, Y. *et al.* Ferroptosis: A Novel Therapeutic Target for Ischemia-Reperfusion Injury. *Front. Cell Dev. Biol.* **9**, 2203 (2021).
327. Palacio-Castañeda, V., Kooijman, L., Venzac, B., Verdurmen, W. P. R. & Gac, S. Le. Metabolic switching of tumor cells under hypoxic conditions in a tumor-on-a-chip model. *Micromachines* **11**, 1–13 (2020).
328. Gdynia, G. *et al.* Basal Caspase Activity Promotes Migration and Invasiveness in Glioblastoma Cells. *Mol. Cancer Res.* **5**, 1232–1240 (2007).

329. Sendoel, A. & Hengartner, M. O. Apoptotic cell death under hypoxia. *Physiology* **29**, 168–176 (2014).

330. Cieśluk, M. *et al.* Nanomechanics and Histopathology as Diagnostic Tools to Characterize Freshly Removed Human Brain Tumors. *Int. J. Nanomedicine* **15**, 7509 (2020).

331. Ciasca, G. *et al.* Nano-mechanical signature of brain tumours. *Nanoscale* **8**, 19629–19643 (2016).

332. Ge, X. *et al.* Hypoxia-mediated mitochondria apoptosis inhibition induces temozolomide treatment resistance through miR-26a/Bad/Bax axis. *Cell Death Dis. 2018 911* **9**, 1–16 (2018).

333. Yin, J. *et al.* Extracellular vesicles derived from hypoxic glioma stem-like cells confer temozolomide resistance on glioblastoma by delivering miR-30b-3p. *Theranostics* **11**, 1763 (2021).

334. Li, H. *et al.* Differences in protein expression between the U251 and U87 cell lines. *Turk. Neurosurg.* (2016).

335. Poon, M. T. C., Bruce, M., Simpson, J. E., Hannan, C. J. & Brennan, P. M. Temozolomide sensitivity of malignant glioma cell lines – a systematic review assessing consistencies between in vitro studies. *BMC Cancer* **21**, 1–9 (2021).

336. Lee, S. Y. Temozolomide resistance in glioblastoma multiforme. *Genes Dis.* **3**, 198–210 (2016).

337. Strobel, H. *et al.* Temozolomide and Other Alkylating Agents in Glioblastoma Therapy. *Biomedicines* **7**, 69 (2019).

338. Zhang, J., F.G. Stevens, M. & D. Bradshaw, T. Temozolomide: Mechanisms of Action, Repair and Resistance. *Curr. Mol. Pharmacol.* **5**, 102–114 (2012).

339. Aasland, D. *et al.* Temozolomide induces senescence and repression of DNA repair pathways in glioblastoma cells via activation of ATR–Chk1, p21, and NF-kB. *Cancer Res.* **79**, 99–113 (2019).

340. Nagane, M. Dose-dense Temozolomide: Is It Still Promising? *Neurol. Med. Chir. (Tokyo).* **55**, 38 (2015).

341. Galldiks, N. *et al.* 'one week on-one week off': Efficacy and side effects of dose-intensified temozolomide chemotherapy: Experiences of a single center. *J. Neurooncol.* **112**, 209–215 (2013).

342. Beier, D. *et al.* Efficacy of clinically relevant temozolomide dosing schemes in glioblastoma cancer stem cell lines. *J. Neurooncol.* **109**, 45–52 (2012).

343. Calcinotto, A. *et al.* Cellular Senescence: Aging, Cancer, and Injury. *Physiol. Rev.* **99**, 1047–1078 (2019).

344. Hernandez-Segura, A., Nehme, J. & Demaria, M. Hallmarks of Cellular Senescence. *Trends Cell Biol.* **28**, 436–453 (2018).

345. Gü, W., Pawlak, E., Damasceno, R., Arnold, H. & Terzis, A. Temozolomide induces apoptosis and senescence in glioma cells cultured as multicellular spheroids. *Br. J. Cancer* **88**, 463–469 (2003).

346. Stratenwerth, B. *et al.* Molecular Dosimetry of Temozolomide: Quantification of Critical Lesions, Correlation to Cell Death Responses, and Threshold Doses. *Mol. Cancer Ther.* **20**, 1789–1799 (2021).

347. Lee, S. & Schmitt, C. A. The dynamic nature of senescence in cancer. *Nat. Cell Biol. 2019 211* **21**, 94–101 (2019).

348. Gorgoulis, V. *et al.* Cellular Senescence: Defining a Path Forward. *Cell* **179**, 813–827 (2019).

349. Silva, A. O., Dalsin, E., Onzi, G. R., Filippi-Chiela, E. C. & Lenz, G. The regrowth kinetic of the surviving population is independent of acute and chronic responses to temozolomide in glioblastoma cell lines. *Exp. Cell Res.* **348**, 177–183 (2016).

350. Wang, H. *et al.* Expression of dynein, cytoplasmic 2, heavy chain 1 (DHC2) associated with glioblastoma cell resistance to temozolomide. *Sci. Rep.* **6**, 28948 (2016).

351. Neurohr, G. E., Terry, R. L., Van Werven, F. J., Holt, L. J. & Correspondence, A. A. Excessive Cell Growth Causes Cytoplasm Dilution And Contributes to Senescence. *Cell* **176**, (2019).

352. Miller, I. *et al.* Ki67 is a Graded Rather than a Binary Marker of Proliferation versus Quiescence. *Cell Rep.* **24**, 1105-1112.e5 (2018).

353. Perepechaeva, M. L. & Grishanova, A. Y. The Role of Aryl Hydrocarbon Receptor (AhR) in Brain Tumors. *Int. J. Mol. Sci.* **21**, (2020).

354. Gramatzki, D. *et al.* Aryl hydrocarbon receptor inhibition downregulates the TGF-β/Smad pathway in human glioblastoma cells. *Oncogene 2009 2828* **28**, 2593–2605 (2009).

355. Yamini, B. NF-κB, Mesenchymal Differentiation and Glioblastoma. *Cells* **7**, (2018).

356. Liu, J. *et al.* Differential effects of estrogen receptor beta isoforms on glioblastoma progression. *Cancer Res.* **78**, 3176 (2018).

357. Tirrò, E. *et al.* Prognostic and Therapeutic Roles of the Insulin Growth Factor System

in Glioblastoma. *Front. Oncol.* **10**, 3301 (2021).

358. Campos, B. *et al.* Aberrant Expression of Retinoic Acid Signaling Molecules Influences Patient Survival in Astrocytic Gliomas. *Am. J. Pathol.* **178**, 1953 (2011).
359. González-Mora, A. M. & Garcia-Lopez, P. Estrogen Receptors as Molecular Targets of Endocrine Therapy for Glioblastoma. *Int. J. Mol. Sci.* **22**, (2021).
360. Xu, Y. *et al.* SULT1E1 inhibits cell proliferation and invasion by activating PPARγ in breast cancer. *J. Cancer* **9**, 1078–1087 (2018).
361. Wijaya, J., Fukuda, Y. & Schuetz, J. D. Obstacles to Brain Tumor Therapy: Key ABC Transporters. *Int. J. Mol. Sci.* **18**, (2017).
362. Bao, X. *et al.* Protein Expression and Functional Relevance of Efflux and Uptake Drug Transporters at the Blood-Brain Barrier of Human Brain and Glioblastoma. *Clin. Pharmacol. Ther.* **107**, 1116–1127 (2020).
363. Emery, I. F. *et al.* Expression and function of ABCG2 and XIAP in glioblastomas. *J. Neurooncol.* **133**, 47 (2017).
364. Housman, G. *et al.* Drug resistance in cancer: An overview. *Cancers (Basel).* **6**, 1769–1792 (2014).
365. Phon, B. W. S., Kamarudin, M. N. A., Bhuvanendran, S. & Radhakrishnan, A. K. Transitioning pre-clinical glioblastoma models to clinical settings with biomarkers identified in 3D cell-based models: A systematic scoping review. *Biomed. Pharmacother.* **145**, 112396 (2022).
366. Demidenko, Z. N. & Blagosklonny, M. V. Growth stimulation leads to cellular senescence when the cell cycle is blocked. *https://doi.org/10.4161/cc.7.21.6919* **7**, 3355–3361 (2008).
367. Yamaki, T. *et al.* Temozolomide suppresses MYC via activation of TAp63 to inhibit progression of human glioblastoma. *Sci. Rep.* **3**, (2013).
368. Luo, H. *et al.* c-Myc–miR-29c–REV3L signalling pathway drives the acquisition of temozolomide resistance in glioblastoma. *Brain* **138**, 3654–3672 (2015).
369. Chan, Y. Y., Kalpana, S., Chang, W. C., Chang, W. C. & Chen, B. K. Expression of Aryl Hydrocarbon Receptor Nuclear Translocator Enhances Cisplatin Resistance by Upregulating MDR1 Expression in Cancer Cells. *Mol. Pharmacol.* **84**, 591–602 (2013).
370. Clark, P. A. *et al.* Activation of multiple ERBB family receptors mediates glioblastoma cancer stem-like cell resistance to EGFR-targeted inhibition. *Neoplasia (United States)* **14**, 420–428 (2012).

371. Zhou, T., Wang, Y., Qian, D., Liang, Q. & Wang, B. Over-expression of TOP2A as a prognostic biomarker in patients with glioma. *Int. J. Clin. Exp. Pathol.* **11**, 1228 (2018).

372. Arivazhagan, A. *et al.* Higher topoisomerase 2 alpha gene transcript levels predict better prognosis in GBM patients receiving temozolomide chemotherapy: identification of temozolomide as a TOP2A inhibitor. *J. Neurooncol.* **107**, 289–297 (2012).

373. Zalcman, N. *et al.* Androgen receptor: a potential therapeutic target for glioblastoma. *Oncotarget* **9**, 19980–19993 (2018).

374. Chen, T. C. *et al.* AR ubiquitination induced by the curcumin analog suppresses growth of temozolomide-resistant glioblastoma through disrupting GPX4-Mediated redox homeostasis. *Redox Biol.* **30**, (2020).

375. Fang, D. D. *et al.* Clinicopathological and Prognostic Significance of ABCC3 in Human Glioma. *J. Oncol.* **2021**, (2021).

376. Zhu, H., Yu, X., Zhang, S. & Shu, K. Targeting the Complement Pathway in Malignant Glioma Microenvironments. *Front. Cell Dev. Biol.* **9**, 758 (2021).

377. Li, X. & Wang, C.-Y. From bulk, single-cell to spatial RNA sequencing. *Int. J. Oral Sci. 2021 131* **13**, 1–6 (2021).

378. Marx, V. Method of the Year: spatially resolved transcriptomics. *Nat. Methods 2021 181* **18**, 9–14 (2021).

379. Kalita-de Croft, P. *et al.* Spatial profiling technologies and applications for brain cancers. *https://doi.org/10.1080/14737159.2021.1900735* **21**, 323–332 (2021).

380. Birzu, C. *et al.* Recurrent Glioblastoma: From Molecular Landscape to New Treatment Perspectives. *Cancers (Basel).* **13**, 1–29 (2021).

381. Hunter, M. V., Moncada, R., Weiss, J. M., Yanai, I. & White, R. M. Spatially resolved transcriptomics reveals the architecture of the tumor-microenvironment interface. *Nat. Commun. 2021 121* **12**, 1–16 (2021).

382. Liu, L. *et al.* CHI3L2 Is a Novel Prognostic Biomarker and Correlated With Immune Infiltrates in Gliomas. *Front. Oncol.* **11**, 1178 (2021).

383. La Rocca, G. *et al.* Glioblastoma CUSA Fluid Protein Profiling: A Comparative Investigation of the Core and Peripheral Tumor Zones. *Cancers 2021, Vol. 13, Page 30* **13**, 30 (2020).

384. Morandi, A., Taddei, M. L., Chiarugi, P. & Giannoni, E. Targeting the Metabolic Reprogramming That Controls Epithelial-to-Mesenchymal Transition in Aggressive

Tumors. *Front. Oncol.* **7**, 1 (2017).

385. Li, X. *et al.* Oxygen-Based Nanocarriers to Modulate Tumor Hypoxia for Ameliorated Anti-Tumor Therapy: Fabrications, Properties, and Future Directions. *Front. Mol. Biosci.* **8**, 604 (2021).

386. Wang, T. *et al.* Biomimetic nanoparticles directly remodel immunosuppressive microenvironment for boosting glioblastoma immunotherapy. *Bioact. Mater.* (2022). doi:10.1016/J.BIOACTMAT.2021.12.029